Wigner reconstruction of the quantum states emitted by a semiconductor laser: Experiments and simulations

Federico Battiston

Supervisors:
Prof. Frederic Grillot
frederic.grillot@phy.ulaval.ca

Prof. Lorenzo Columbo
lorenzo.columbo@polito.it

Dr. Juan Rafael Alvarez Velasquez
juanrafael.alvarez@telecom-paris.fr

Dr. Heming Huang
heming.huang@telecom-paris.fr

Politecnico di Torino
Telecom Paris

April 2025 – September 2025

Contents

Chapter 1

Introduction

The quantum description of light has enabled the measurement of new states of light as well as the development of novel technologies such as quantum sensing, quantum computing and quantum communications. One notable method used in the field of quantum communications is Quantum Key Distribution (QKD), which enables the secure exchange of a secret key between distant partners relying on the laws of quantum mechanics.

One important branch of quantum key distribution (QKD) is continuous-variable QKD (CV-QKD). In contrast to discrete-variable (DV) protocols such as BB84, which encode information in single photons using discrete degrees of freedom like polarization (leading to *discrete values*) [1], CV-QKD encodes information in the continuous observables of the electromagnetic field—typically the amplitude and phase quadratures [2, 3]. This approach enables the use of standard telecommunication technologies, such as coherent detection and Gaussian modulation, making it particularly appealing for practical implementations of quantum-secure communication.

This framework can be moreover operated at room temperature and enables the use of standard telecommunication equipment like coherent lasers, electro-optic modulators, and high-efficiency balanced homodyne detectors [4, 5], which allows for easier implementation and commercialization [6].

Unlike classical communications, the most dominant noise in CV quantum communications is the shot noise: going below the shot noise limit is a crucial task for the development of efficient communication protocols. Squeezed states, which reduce the noise in one quadrature at the expense of increasing it in the conjugate quadrature [7], could enable the development of CV quantum communication protocols that go below the shot noise limit. These states also play a crucial role in quantum sensing (such as in gravitational wave detection [8]) and in quantum computing [9, 10].

Squeezed states are usually generated by nonlinear optical processes based on a $\chi^{(2)}$ response as parametric down-conversion in non-linear crystals like $LiNbO_3$ [11] or $\chi^{(3)}$ processes exploiting four wave mixing [12, 13]. However, another interesting way that could produce squeezing without nonlinear media is by using a quantum-well or a quantum dot laser driven by a quiet pump source [14]. Indeed, as noted by Zhao et al. in [15], in this regime it is possible to achieve noise below the shot-noise limit, together with a second-order correlation function slightly below one, indicative of amplitude squeezing [16].

In this work, we establish an experimental setup for performing the full tomography of a quantum field produced by a low noise tuneable laser with the aims of further expanding this work in order to analyse quantum properties of light of semiconductor lasers.

We report on the measurement of vacuum and coherent states using this experimental setup (see: 5.2, 4.2). However it could be used to characterize any state of light emitted by a generic source, as in the quiet pump regime [15, 16].

The thesis is mainly divided into four main chapters. The theoretical background is introduced in Chapter 2, then the characterization of the setup is illustrated in Chapter 3 while the Inverse Radon Transform method, that is the common technique to characterize those states, is described in Chapter 4 together with the corresponding experimental results. Finally the Maximum Likelihood Estimation and the corresponding experimental results are discussed in Chapter 5. The last chapter, is dedicated to a description of the agenda with a focus on what we think represented the main challenges of this work and possible strategies to meet them.

Chapter 2

Quantum state tomography: Theoretical background

2.1 The wavefunction

Quantum mechanics is a revolutionary theory formally developed in the 20th century. One of its main novelties, as the name is suggesting, is the *quantization* of the energy [17,18]. Therefore, new physical quantities able to discretize the world, as the photon for the electromagnetic field, [19] are introduced.

On the other hand, quantum mechanics associates a wave-like description (that is formally continuous) to body-like physical quantities. Refer for example to the Stern-Gerlach experiment in 1922 [20]. This duality takes the name of *wave-particle dualism* [21].

It follows that, in quantum mechanics, the concept of *deterministic* particle is abandoned, and the systems will be described by *states* that are the eigenfunctions of the Hamiltonian operator (associated to the energy), also called *wavefunctions*.

The wavefunction ψ, is a complex function such that, for each time $t \in \mathbb{R}$, the function $\psi(\cdot, t) \in L^2(\mathbb{R})$ represents the quantum state of a particle, if $L^2(\mathbb{R}^n)$ is the space of square-integrable functions:

$$\psi \in L^2 \quad \text{if} \quad \int_{\mathbb{R}^n} |\psi(x,t)|^2 \, dx < \infty. \tag{2.1.1}$$

However, the value of ψ is not directly a measurable quantity; instead, its modulus square $|\psi|^2$ is, and it represents the probability of finding the particle at position x and time t [22].

This result leads to the second crucial consequence of the quantum mechanics: the probabilistic way of interpreting the information.

Indeed, while in classical mechanics the complete knowledge of a system at time $t = 0$ uniquely determines its future evolution, in quantum mechanics one can only predict the probability distributions of the outcomes of measurements of physical observables.

However, it is still possible to construct situations where, under particular conditions, the probability of a specific outcome becomes arbitrarily close to one, or even exactly one in idealized limits.

2.1.1 The operators

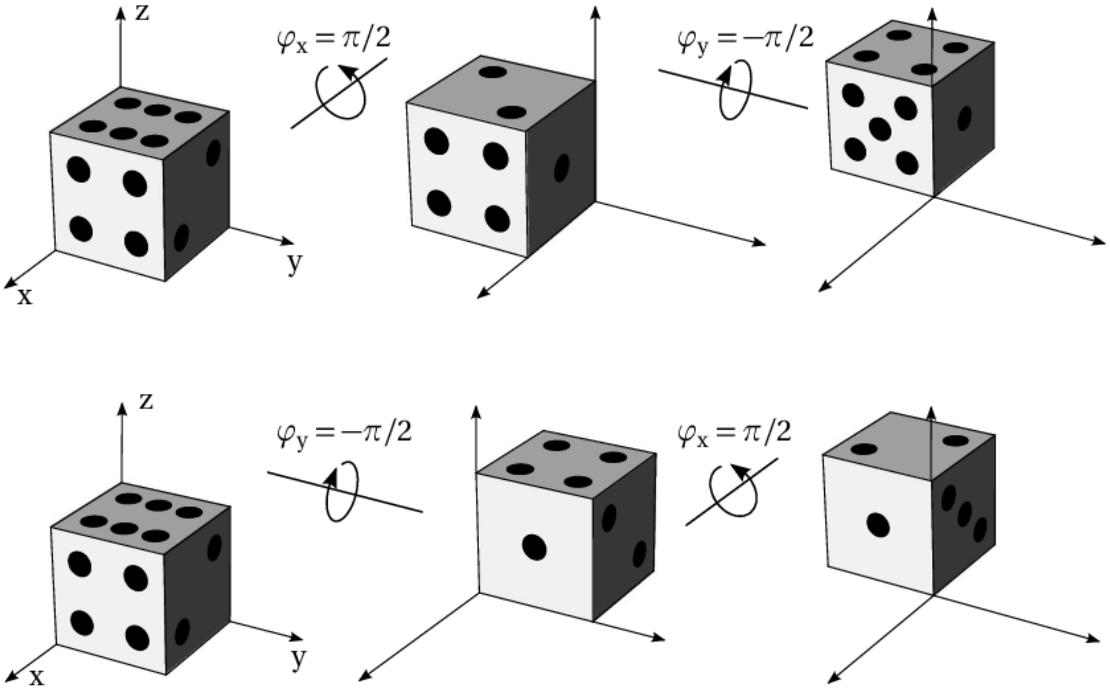

Figure 2.1: In the figure, reproduced from [23], is shown a figurative representation of how non-commuting quantities operate on a system. Supposing that the operator $\hat{A}$ is the rotation on the **x** plane and the operator $\hat{B}$ is a negative rotation on the **y** plane, then the action of $\hat{A}$ followed by the application of $\hat{B}$ does not have the final effect of the inverse process.

Once the system is defined by its state ψ, then its evolution (also partial) in quantum mechanics is described through *operators*.
An operator can be described as an *action* on a system, and it represents the only way to interfere with it (for instance, also the measurement process comes from the measurement operator $\hat{\mathcal{M}}$ acting on the system).

Any physical *observable* (i.e. quantity that can be measured) has to be associated with an operator **A** that has to be self adjoint, i.e. equal to its transpose conjugate.

However, differently from classical mechanics, in the quantum theory, some operators do not *commute* (for instance the position $\hat{x}$ and the momentum $\hat{p}$ operators), if the commutator $[\cdot]$ between two objects $\hat{A}, \hat{B}$ is defined as:

$$[\hat{A}, \hat{B}] = \hat{A}\hat{B} - \hat{B}\hat{A}. \tag{2.1.2}$$

The non-commutation relationship is formalized as $[\hat{A},\hat{B}] \neq 0$, and, in such cases, it is not possible to find a common eigenbasis that diagonalizes both $\hat{A}$ and $\hat{B}$. Consequently, one cannot simultaneously assign definite eigenvalues to both observables without an intrinsic uncertainty. Since the eigenvalues are related to the measurement, it implies that two non-commuting operators can not be measured in the same system with arbitrary precision.
This limitation is formalized by the Heisenberg uncertainty principle [24, 25] and will be important in the later on described quadratures of the field. Figure 2.1, reproduced from [23], visualizes this concept.

If on one hand this represents a limit in different problems (as the solution of hydrogen atom), on the other hand it has an important role in applications as Quantum Communication.
For instance, in the BB84 protocol, a malicious Eve can not retrieve the information of Alice and Bob without being discovered (in a statistical way) since her action perturbs the system.
More complex protocols exist, where continuous variables as the quadratures $\hat{X}$ and $\hat{P}$ of the field are used as encoding system. For such reason, those protocols are called CV (Continuous-Variable) QKD (Quantum Key Distribution).

2.1.2 The Schrödinger and the Heisenberg formalisms

Two different formalisms exist in quantum mechanics: the Schrödinger picture, introduced by Erwin Schrödinger in 1926, and the Heisenberg one proposed by Werner Heisenberg in 1925.
Both frameworks carry the same mathematical information, but *where* the time takes action is changing. Indeed in the Schrödinger picture, the operators are time independent while the states (wavefunctions) are time dependent; on the other hand, in the Heisenberg picture, the operators depend on time, while the states are time independent.
Therefore the only difference between the two frameworks consists in a sign in the system evolution equation.
For convenience, both pictures will be used in this work.

An operator, in the Heisenberg formalism could be represented by its matrix form that can be both finite ($\hat{\mathcal{A}} \in \mathbb{R}^n$) or infinite (as position $\hat{x}$ and momentum $\hat{p}$), while a state is represented by a column vector $|\psi\rangle$, also called *ket* vector. On the other hand its adjoint $|\psi\rangle^\dagger$ is called *bra* vector [18]. Therefore, the final state can be calculated as the action of the operator $\hat{\mathcal{A}}$ on the initial state $|\psi\rangle_{in}$, thus the product of the operator by the state vector: $|\psi\rangle_{fin} = \hat{\mathcal{A}}\,|\psi\rangle_{in}$.

Conversely, in the Schrödinger picture the evolution of a quantum system is ruled by the Schrödinger equation, that reads as:

$$i\hbar\frac{\partial}{\partial t}\psi(x,t) = \hat{H}\psi(x,t). \tag{2.1.3}$$

The operators are represented by *applications* (as derivatives) and wavefunctions in L^2 as before anticipated.
This equation could moreover be simplified in its easier time independent version (only when the operator $\hat{H}$ is constant in time):

$$\hat{H}\left|\psi_E\right\rangle = E\left|\psi_E\right\rangle. \tag{2.1.4}$$

Here $\hat{H}$ is the Hamiltonian operator, associated with the energy of the system.
In general, the Hamiltonian, is composed by a kinetic $(\frac{\hat{p}^2}{2m})$ and a potential $(\hat{U}(x,t))$ term. Therefore, if only the kinetic term of the Hamiltonian is non-vanishing, the one-dimensional (time dependent) Schrödinger equation could be further simplified as:

$$i\hbar\frac{\partial}{\partial t}\psi(x,t) = -\frac{\hbar^2}{2m}\frac{\partial^2}{\partial x^2}\psi(x,t). \tag{2.1.5}$$

Moreover, since the Schrödinger equation is a linear equation, with $|\cdot\rangle$ as solutions, then a generic state will be represented by a linear superposition of all the solution states:

$$|\psi\rangle = \sum_{i=0}^{n} a_i\phi_i \qquad\qquad \sum_{i}^{n}|a_i|^2 = 1, \tag{2.1.6}$$

where the a_i are normalization coefficients introduced since $\|\psi\|^2$ is associated to the probability of find the state ψ.
For example, for a two level system, if one identifies two different solutions (namely $|0\rangle$ and $|1\rangle$), then a generic state describing the system will be:

$$|\psi\rangle = a_0\,|0\rangle + a_1\,|1\rangle\,, \tag{2.1.7}$$

where $a_0, a_1 \in \mathbb{C}$ are such that $|a_0|^2 = \mathbb{P}(|\psi\rangle = |0\rangle)$ and $|a_1|^2 = \mathbb{P}(|\psi\rangle = |1\rangle)$.

Finally, the complex inner product $\langle u|v\rangle$ is introduced. This operation is used to calculate the probability amplitudes and expectation values of observables, providing a direct connection between the state of the system and measurable quantities.

2.1.3 The quantum harmonic oscillator

From a classical perspective, the light is defined as an oscillating electromagnetic (e.m.) field, and shows peculiar properties as interference and diffraction typical of a wave-like description.

The quantization of the e.m. field began with the interpretation of the photoelectric effect by Albert Einstein in 1905, and it is called second quantization [18, 26].
Indeed, inspired with the Planck's earlier work on blackbody radiation, Einstein proposed that light is composed by discrete *energy packets* called photons, each one carrying an energy $E = h\nu$, being h the Plank's constant and ν the frequency of the field. This is in clear contradiction with the classical formalism, where the energy of the field is determined by its intensity.

It is a known result that a single-mode light field behaves as a harmonic oscillator, as shown in Appendix 6.1.
For instance, one of the many similarities is that the two models share the same description of the energy:

$$\begin{array}{cc} \text{hamornic oscillator energy} & \text{em energy} \\ \frac{1}{2m}p^2 + \frac{1}{2m}\omega^2 x^2, & \frac{1}{2}\varepsilon_0 \mathcal{E}^2 + \frac{1}{2\mu_0}\mathcal{B}^2, \end{array} \tag{2.1.8}$$

where p and x are the momentum and position of the particle in the harmonic oscillator, while $\mathcal{E}, \mathcal{B}$ are the electric and magnetic fields.

This analogy can be extended to quantum mechanics, where the quantum harmonic oscillator must be used. In this model the field is described in terms of the creation ($\hat{a}^\dagger$) and annihilation ($\hat{a}$) operators [7], able to create ($\hat{a}^\dagger$), or destroy ($\hat{a}$) a particle.
Those operators are needed since, in the quantum harmonic oscillator, discrete energy levels are achieved.
Therefore, if one particle has to move from one level (for example $|0\rangle$) to another (for example $|1\rangle$), one has to remove it from one level ($\hat{a}\,|0\rangle$), and add it to the new one ($\hat{a}^\dagger\,|1\rangle$).
Then the creation and annihilation operators allow particles to move between the discretized levels of the quantum harmonic oscillator as along a stair, reason why they are called *ladder* operators:

$$\begin{tikzcd}
|0\rangle \arrow[r, bend left, dashed, "a^\dagger"] & |1\rangle \arrow[l, bend left, "a"] \arrow[r, bend left, dashed, "a^\dagger"] & |2\rangle \arrow[l, bend left, "a"] \arrow[r, bend left, dashed, "a^\dagger"] & \cdots \arrow[l, bend left, "a"]
\end{tikzcd}$$

However, in quantum mechanics, the creation and annihilation operators $\hat{a}$ and $\hat{a}^\dagger$ are not associated to observable quantities and in general they do not commute:

$$[\hat{a}, \hat{a}^\dagger] = 1. \tag{2.1.9}$$

Their relative eigenvalue equations, if n is the number of particles in the state, are:

$$\hat{a}^\dagger\,|n\rangle = \sqrt{n+1}\,|n+1\rangle \tag{2.1.10}$$

$$\hat{a}\,|n\rangle = \sqrt{n}\,|n-1\rangle \tag{2.1.11}$$

$$|n\rangle = \frac{1}{\sqrt{n!}}(\hat{a}^\dagger)^n\,|0\rangle\,, \tag{2.1.12}$$

$$\tag{2.1.13}$$

with the boundary conditions:

$$\hat{a}\,|0\rangle = 0, \tag{2.1.14}$$

$$\hat{a}^\dagger(a\,|0\rangle) = 0. \tag{2.1.15}$$

Here the number operator $\hat{n}$ and the Fock state $|n\rangle$ (described in the following subsection) were defined, and are related to the number of particles present in the state.
Indeed, since $\hat{n} = \hat{a}^\dagger \hat{a}$:

$$\langle n| \hat{a}^\dagger \hat{a} |n\rangle = \sqrt{n} \langle n| \hat{a}^\dagger |n-1\rangle = \sqrt{n}\sqrt{n} \langle n, n\rangle = n \tag{2.1.16}$$

effectively retrieving the number of photons present in the state $|n\rangle$.
The boundary conditions in Eq 2.1.15 imply that no photon can be removed from the state in which no photons are present ($\hat{a}|0\rangle = 0$), and that this state carries no photons. This state is referred to as the vacuum.

Finally, one can then define the quantum electric field $\mathcal{E}(x,t)$ as:

$$\mathcal{E}(x,t) = u^*(x,t)\hat{a} + u(x,t)a^\dagger \tag{2.1.17}$$

where u is the spatio-temporal mode and $a, a^\dagger$ are the creation and annihilation operators [7].

The phase shifting operator, on the other hand, is defined as $\hat{U}(\theta) = e^{-i\theta\hat{n}}$ and introduces a complex phase to the field, if θ is the phase rotation angle applied to the optical mode.
Indeed:

$$\frac{d}{d\theta}\hat{a}(\theta) = i\hat{n}\hat{U}(\theta)^\dagger \hat{a}\hat{U}(\theta) - \hat{U}(\theta)^\dagger \hat{a}(i\hat{n})\hat{U}(\theta) = i\hat{U}(\theta)^\dagger [\hat{n}, \hat{a}]\hat{U}(\theta) = -i\hat{a}(\theta). \tag{2.1.18}$$

Therefore, $\hat{a}(\theta) = \hat{a}(0)e^{-i\theta}$, where $\hat{a}(0)$ sets the reference phase. So the generic form of 2.1.17 could be written as:

$$\mathcal{E}(x,t) = u^*(x,t)e^{-i\theta}\hat{a} + u(x,t)e^{i\theta}\hat{a}^\dagger \tag{2.1.19}$$

On the other hand, it is well known that a classical e.m. field can be completely described by the In-phase (I) and in-Quadrature (Q) components, representing the Real and Imaginary components of the field. Since classical mechanics is a particular case of quantum mechanics, those components have to have a quantum version. Therefore, the *quadrature operators* are introduced, usually referred as $\hat{X}, \hat{P}$ or $\hat{q}, \hat{p}$ [27].
In particular, the two quadratures, play the same role as the position $\hat{x}$ and momentum $\hat{p}$ operators in the quantum harmonic oscillator, and they have the same mathematical description under proper normalizations and they are linked by a Fourier transform (see Appendix 6.7) [7]. Consequently, the quadrature vector moves as a rigid rotation in the phase space (the space spanned by X and P), just as position and momentum do in the harmonic oscillator (in the x, p space). Moreover, since the two quadratures encode all the physical information of the field, it that can be expressed as:

$$\mathcal{E} = \sqrt{2}\mathcal{E}_0 \left[\hat{X}\cos(\omega t) + \hat{P}\sin(\omega t)\right]. \tag{2.1.20}$$

Therefore, the two quadratures reads [7, 28]:

$$\hat{X} = \frac{\hat{a} + \hat{a}^\dagger}{\sqrt{2}}, \tag{2.1.21}$$

$$\hat{P} = \frac{\hat{a} - \hat{a}^\dagger}{\sqrt{2}i}, \tag{2.1.22}$$

with indetermination relation $[\hat{X},\hat{P}] = i$ $(\Delta X \Delta P \geq \frac{1}{2})$, if $\hbar = 1$.

However, by construction, the two quadratures (Real and Imaginary components of the field) are linked by a phase difference. Therefore, the previously defined operator $U(\theta)$ can relate them and the generalized quadrature operator $\hat{X}_\theta$ or $\hat{x}_\theta$ can be defined. Moreover [7]:

$$\hat{X}_\theta = U(\hat{\theta})^\dagger \hat{X} U(\hat{\theta}) = \hat{X}\cos\theta + \hat{P}\sin\theta, \tag{2.1.23}$$

$$\hat{P}_\theta = U(\hat{\theta})^\dagger \hat{P} U(\hat{\theta}) = \hat{P}\cos\theta - \hat{X}\sin\theta. \tag{2.1.24}$$

Finally, using the relations:

$$\hat{a} = \sqrt{\frac{1}{2}}\left(\hat{X} + i\hat{P}\right), \tag{2.1.25}$$

$$\hat{a}^\dagger = \sqrt{\frac{1}{2}}\left(\hat{X} - i\hat{P}\right). \tag{2.1.26}$$

one can derive the energy of the quantum harmonic oscillator, written as [7]:

$$\hat{H} = \omega\left(\hat{n} + \frac{1}{2}\right) = \omega\left(\frac{\hat{X}^2}{2} + \frac{\hat{P}^2}{2}\right) \tag{2.1.27}$$

where, $\hbar$ was set to one.

2.2 The quantum states of light

Following the reasoning in subsection 2.1.3, the light is composed by discrete particles called photons; moreover the energy levels are quantized, and the ladder operators are used to move among these.
Therefore, the quantum state of light is described by a generic distribution of such particles. These states are called Fock states and are defined as the eigenstates of the number operator $\hat{n}$:

$$\hat{n}\,|n\rangle = n\,|n\rangle\,, \tag{2.2.1}$$

where $n \geq 0$ is an integer that represents the number of particles.
Moreover, since these states are orthogonal, they form an orthonormal basis, which spans the entire space, called the Fock space [7, 29].

Due to the correspondence between each mode of the quantized electromagnetic field and a quantum harmonic oscillator, the energy eigenstates of the field are identical in form to those of a harmonic oscillator. Hence, solving the harmonic oscillator problem yields the photon-number (Fock) states, which in the quadrature representation read:

$$\psi_n(X) = \langle X|n\rangle = \frac{1}{\sqrt[4]{\pi}\sqrt{2^n n!}} H_n(X) e^{-\frac{X^2}{2}}, \tag{2.2.2}$$

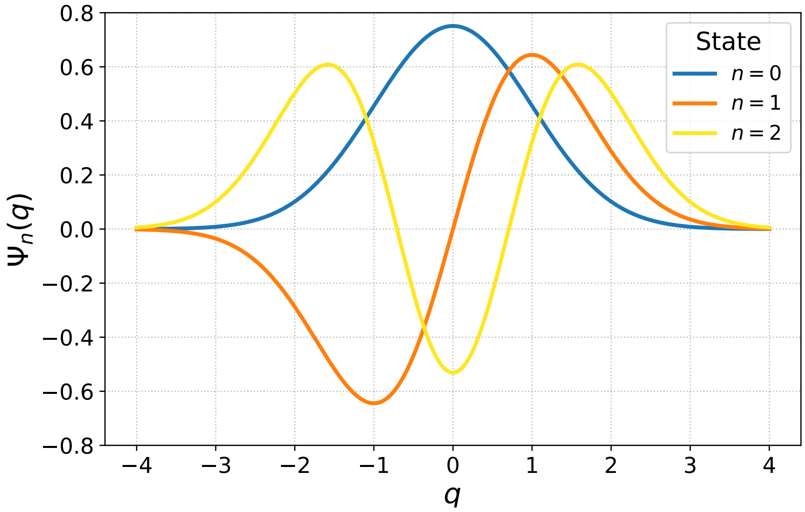

Figure 2.2: In the image are shown the Fock wavefunction of order 0,1,2 calculated with the general formula shown in equation 2.2.2. The one that correspond to n=0 is the one that correspond to the vacuum state.

if $H_n(X)$ are the Hermite polynomials defined as:

$$H_n(X) = (-1)^n e^{X^2} \frac{d^n}{dX^n}(e^{-X^2}), \tag{2.2.3}$$

the derivation is reported in Appendix 6.2 .
The simplest example of such states is the previously anticipated vacuum state, which corresponds to the absence of photons. It exhibits the minimum variance allowed by the Heisenberg uncertainty principle. This variance, known as the ground-state noise or shot noise, sets a fundamental lower limit on the fluctuations of the field quadratures and can not be reduced by standard measurement techniques.
Returning to the correspondence between the quadratures and the position and momentum operators of the quantum harmonic oscillator, the shot noise plays the role of a mass in the normalization of the field. Since the shot noise (i.e., quantum noise) depends on the optical power of the employed light, a proper normalization procedure must be applied so that quantum states are represented independently of the field strength. Consequently, states in phase space are expressed in shot noise Units (SNU) [7, 11].

In the following sections, different states of light are analysed, and their properties are discussed.

2.2.1 The vacuum states

As previously anticipated. the vacuum state, usually represented with $|0\rangle$, is the state where no photons are present. Therefore it represents the ground state from which one is able to generate all the other states (by using the ladder operators).

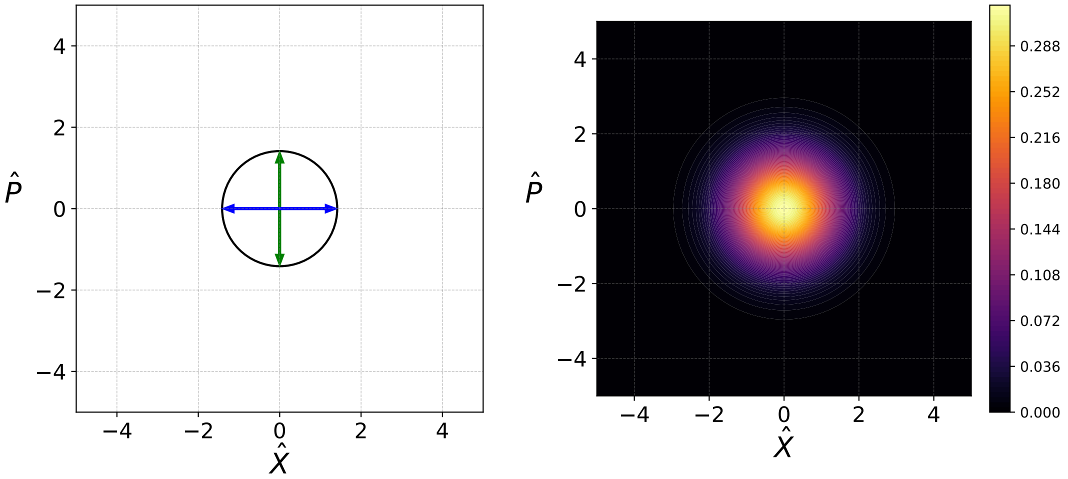

Figure 2.3: On the left the representation of the photon state with 0 photons (vacuum state) in the phase space, while on the right its probability distribution. As can be seen, the vacuum state shows the same variances for all the quadratures and the probability distribution is a Gaussian function centred in the origin.

Its mathematical representation can be derived starting with the general Fock-state equation derived in Appendix 6.2.

However, it is instructive to use one of the boundary conditions for the annihilation operator $\hat{a}$, defined in 2.1.15, since they directly come from the physics of the vacuum state. in particular, if the annihilation operator is applied to vacuum:

$$\hat{a}\,|0\rangle = \frac{1}{\sqrt{2}}(\hat{X} + i\hat{P})\,|0\rangle = 0, \tag{2.2.4}$$

if $|0\rangle$ is the vacuum state, which wavefunction is called ψ_0.

Moreover, since $\hat{P} = -i\frac{\partial}{\partial X}$, then:

$$\psi_0 = Ae^{-\frac{X^2}{2}}, \tag{2.2.5}$$

exactly what expected with n = 0 in equation 2.2.2 (see Appendix 6.3).

This wavefunction is a Gaussian centred at the origin of phase space and exhibits a constant variance (i.e., independent of X). Consequently, the vacuum state is represented by a Gaussian distribution in phase space centred at the origin.

As will be discussed later, this phase-space distribution is known as the *Wigner function*, and the procedure used to reconstruct it experimentally is called quantum state tomography.

In order to determine the constant A, that has to be understood as a normalization constant, the Born principle (normalization of the wavefunction) could be uses: $\int_{-\infty}^{+\infty} \psi\psi^* = 1$, thus achieving $A = \frac{1}{\sqrt[4]{\pi}}$.

Therefore, the final vacuum wavefunction then reads:

$$\psi_0 = \frac{1}{\sqrt[4]{\pi}} e^{-\frac{X^2}{2}}. \tag{2.2.6}$$

The variance of the vacuum state is chosen to be $\frac{1}{2}$ (i.e. standard deviation $\sigma = \frac{1}{\sqrt{2}}$) in normalized units. This variance (uncertainty) corresponds to the previously mentioned shot noise or quantum noise, i.e., the minimum uncertainty expected when measuring states of light.

2.2.2 Coherent states

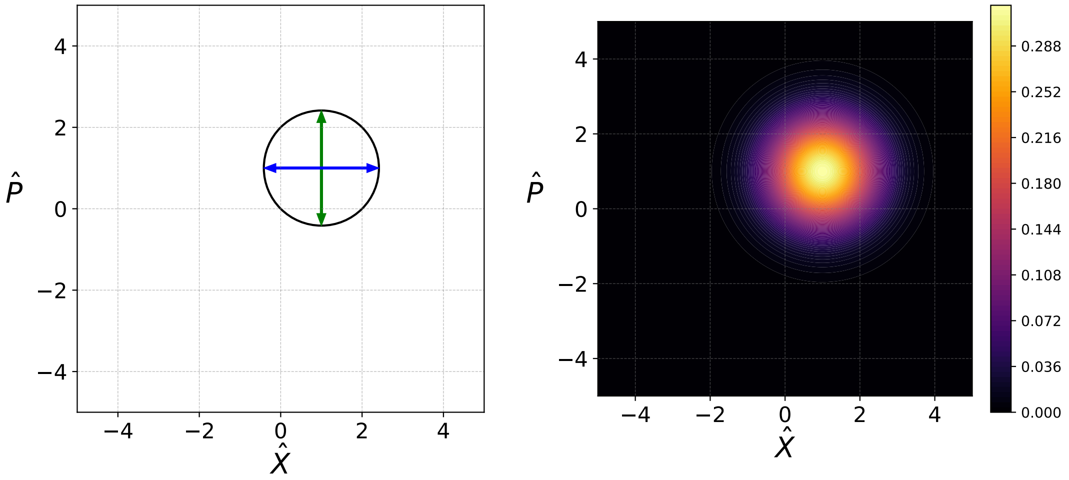

Figure 2.4: On the left the representation of the coherent wavefunction with coherent parameter $\alpha = 1 + i$, associated with $|1 + i|^2$ mean photons is shown. Its Wigner (right) distribution shows the same variance as vacuum with a shift in the phase space, as expected.

Coherent states are defined as the eigenvectors of the annihilation operator [7]:

$$|\alpha\rangle \quad \text{coherent if} \quad \hat{a}\,|\alpha\rangle = \alpha\,|\alpha\rangle \tag{2.2.7}$$

Where α is the coherent parameter and its square modulus determines how many photons (on average) the state has ($\langle n\rangle = |\alpha|^2$).
These states are emitted by an ideal laser. Indeed, by looking at the first order correlation function $g^{(1)}(\tau)$, used to define the coherence properties of a field from time t to time $t+\tau$, if $|\psi\rangle = |\alpha\rangle$, $\hat{a}\,|\alpha\rangle = \alpha\,|\alpha\rangle$ and $a\hat{(t)} = a\hat{(0)}e^{-i\omega t}$:

$$g^{(1)}(\tau) = \langle \hat{a}(0)^\dagger e^{i\omega t}\hat{a}(0)e^{-i\omega(t+\tau)}\rangle = e^{i\omega\tau}\langle \hat{a}(0)^\dagger \hat{a}(0)\rangle = \text{const.} \tag{2.2.8}$$

Therefore, the eigenstate of the annihilation operator has an infinite coherence time: the main property of an ideal laser.

While for all the other Fock states:

$$\hat{a}\left|n\right\rangle = \sqrt{n}\left|n-1\right\rangle \Rightarrow \langle n|\hat{a}^{\dagger}(t)\hat{a}(t+\tau)|n\rangle = 0 \tag{2.2.9}$$

related to a finite coherence time.

Finally, using the quadrature operator definitions, it is possible to estimate the variance of the coherent state as:

$$\begin{align}
\mathrm{Var}(\hat{X}) &= \mathbb{E}(\hat{X}^2) - \mathbb{E}(\hat{X})^2 \tag{2.2.10}\\
&= \frac{1}{2}\left[\left\langle\alpha\right|(\hat{a}+\hat{a}^{\dagger})^2\left|\alpha\right\rangle - \Big(\left\langle\alpha\right|(\hat{a}+\hat{a}^{\dagger})\left|\alpha\right\rangle\Big)^2\right] \tag{2.2.11}\\
&= \frac{1}{2}\left[\alpha^2 + 2|\alpha|^2 + \alpha^{*2} + 1 - (\alpha+\alpha^*)^2\right] \tag{2.2.12}\\
&= \frac{1}{2}\left[\alpha^2 + \alpha^{*2} + 2|\alpha|^2 + 1 - \Big(\alpha^2 + \alpha^{*2} + 2|\alpha|^2\Big)\right] \tag{2.2.13}\\
&= \frac{1}{2} = \mathrm{Var}(\hat{P}), \tag{2.2.14}
\end{align}$$

Analogously to the vacuum state.
However a non-zero mean photon number characterizes the coherent state, determining a *shift* in the Wigner representation with respect to the origin of the phase space [7]. For this reason, coherent states are usually referred to as *displaced vacuum* states.
Therefore, the displacement operator is defined as:

$$\hat{D}(\alpha) = e^{\alpha a^{\dagger} - \alpha^* a} \qquad\qquad \hat{D}(\alpha)^{\dagger}\hat{a}\hat{D}(\alpha) = \hat{a} + \alpha. \tag{2.2.15}$$

Conversely,

$$\hat{D}(-\alpha)\left|\alpha\right\rangle = \left|0\right\rangle,$$

if, again, $|0\rangle$ is the vacuum state.
However, coherent states should be considered as new states of light with their own properties, distinct from the vacuum state [7]. In particular, coherent states are characterized by a random photon number, leading to a Poissonian distribution in the Fock space, as shown in Appendix 6.4. Therefore, a coherent state reads:

$$\left|\alpha\right\rangle = \sum_{n=0}^{\infty} e^{-\frac{|\alpha|^2}{2}} \frac{\alpha^n}{\sqrt{n!}}\left|n\right\rangle. \tag{2.2.16}$$

Furthermore, especially when the mean photon number is not zero, the centre of the Wigner function depends on the normalization of the quadrature operators. In the conventional framework, where a multiplicative factor of $\frac{1}{\sqrt{2}}$ is included in the quadrature definition, the centre of the distribution appears at $\sqrt{2}\alpha$. Conversely, if this factor is replaced by $\frac{1}{2}$, the centre remains exactly at α.

Indeed:

$$\begin{aligned} X &= \langle\alpha| \frac{\hat{a}+\hat{a}^\dagger}{\sqrt{2}} |\alpha\rangle \\ &= \frac{\langle\alpha| \hat{a} |\alpha\rangle + \langle\alpha| \hat{a}^\dagger |\alpha\rangle}{\sqrt{2}} \\ &= \frac{2\alpha_{\mathbb{R}}}{\sqrt{2}} = \sqrt{2}\,\alpha_{\mathbb{R}}. \end{aligned} \tag{2.2.17}$$

While if:

$$\hat{X} = \frac{\hat{a}+\hat{a}^\dagger}{2}, \tag{2.2.18}$$

$$\hat{P} = \frac{\hat{a}-\hat{a}^\dagger}{2i}, \tag{2.2.19}$$

one achieves:

$$\begin{aligned} X &= \langle\alpha| \frac{\hat{a}+\hat{a}^\dagger}{2} |\alpha\rangle \\ &= \frac{\langle\alpha| \hat{a} |\alpha\rangle + \langle\alpha| \hat{a}^\dagger |\alpha\rangle}{2} \\ &= \frac{2\alpha_{\mathbb{R}}}{2} = \alpha_{\mathbb{R}}. \end{aligned} \tag{2.2.20}$$

Similar relations can be derived for the $\hat{P}$ quadrature.
From now on (unless stated otherwise) whenever a displaced Wigner function is mentioned, its maximum will be assumed to occur at α, since this is the conventional choice that allows for a direct estimation of the coherent parameter.

2.2.3 Squeezed states

Both coherent and vacuum states, as previously derived, show the same variance properties. In particular they are able to minimize the Heisenberg uncertainty principle (allow for the equality to hold). For such reason are also referred to as *minimum uncertainty states*.
There is another state able to minimize the Heisenberg relation: the squeezed state (see Appendix 6.6).

However, the squeezed light, differently from coherent and vacuum states shows an unbalance between the variances of the two quadratures: the quadratures with the smaller variance will be called *squeezed* quadrature, while the other one will be the *anti-squeezed* one.
Of course, since the Heisenberg uncertainty principle still holds, the squeezed quadrature is expected to have a variance lower than that of the vacuum, while the anti-squeezed quadrature has a larger variance.

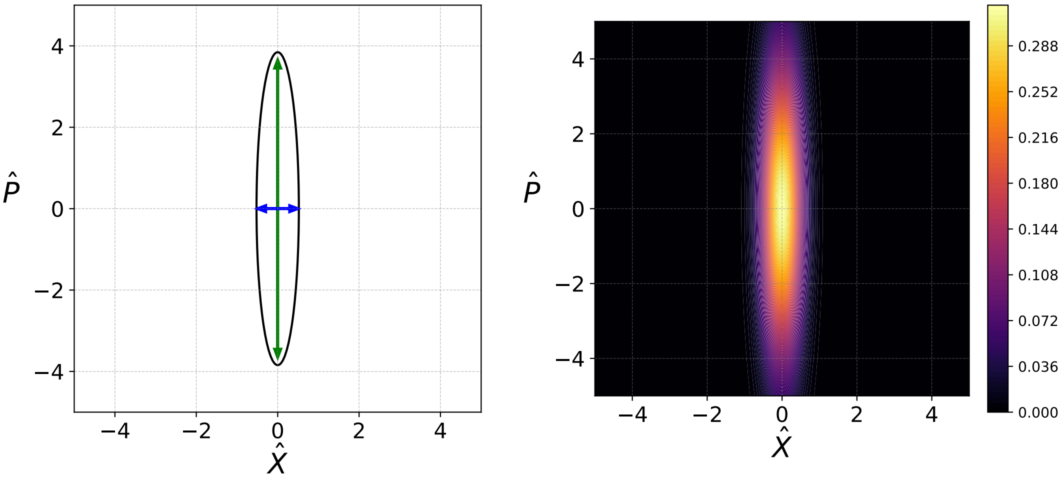

Figure 2.5: On the left, the representation of a squeezed vacuum state with squeezing parameter $r = 1$ is shown, while on the right its Wigner function is displayed. A strong imbalance between the variances of the squeezed and anti-squeezed quadratures is observed, as expected for such a high squeezing parameter, while the function remains centred at the origin since the mean photon number is zero.

Following the definition of the Pauli argument [7]:

$$\delta \equiv |\frac{q}{2\Delta^2 q}\varphi + \frac{\partial\varphi}{\partial q}|^2, \tag{2.2.21}$$

one can derive the squeezed wavefunction as:

$$\varphi(X) = (2\pi\Delta^2 X)^{-\frac{1}{4}} e^{-\frac{X^2}{4\Delta^2 X}}, \tag{2.2.22}$$

that has a Gaussian shape (as vacuum and coherent states), but that is not *forced* to have a symmetric variance between the two quadratures.
However, no hypothesis was assumed on the mean number of photon number of that state. Indeed, the *squeezing* is a property regarding the variances of the quadratures. Therefore, if the Wigner representation in the phase space is centred in the origin ($\alpha = 0$), it is called *squeezed vacuum*. Conversely, if the state is *displaced* ($\alpha \neq 0$) it is called *squeezed displaced* or *displaced squeezing*.
Therefore, it is convenient to introduce an operator able to *squeeze* a state. This operator is named *squeezing operator*, and it is defined as [7, 30]:

$$S\hat{(r)} = \exp\left[\frac{r}{2}\left(\hat{a}^2 - \hat{a}^{\dagger 2}\right)\right], \tag{2.2.23}$$

where r is the *squeezing parameter*. In particular, r determines the noise properties of the squeezed state (see Appendix 6.5); indeed, the higher is r and the higher will be the unbalance between the squeezed and anti-squeezed quadrature.

Consequently, the squeezed vacuum state will be defined as $(|\psi_{0r}\rangle = S(r)\,|0\rangle$, while a displaced squeezed state can be defined as $|\psi_{\alpha,r}\rangle = D(\alpha)S(r)\,|0\rangle$.

In order to derive the squeezing operator, one can start by the squeezed vacuum wavefunction, defined as:

$$\psi_r(X) = e^{r/2}\psi_0(e^r X). \tag{2.2.24}$$

By taking its derivative:

$$\begin{aligned}
\frac{\partial}{\partial r}\psi_r(X) &= \frac{\partial(e^{\frac{r}{2}})}{\partial r}\psi_0(e^r X) + \frac{\partial(\psi_0(e^r X))}{\partial r}e^{\frac{r}{2}} \\
&= \frac{1}{2}\psi_r(X) + X'\frac{\partial}{\partial X'}\psi_r(X) \\
&= \frac{1}{2}[2X'\frac{\partial}{\partial X'} + 1]\psi_r(X) \\
&= \frac{1}{2}[X'\frac{\partial}{\partial X'} + \frac{\partial}{\partial X'}X']\psi_r(X) \\
&= \frac{i}{2}[X'(-i\frac{\partial}{\partial X'}) + (-i\frac{\partial}{\partial X'}X']\psi_r(X) \\
&= \frac{1}{2}[i\hat{X}\hat{P} + i\hat{P}\hat{X}]\psi_r(X),
\end{aligned} \tag{2.2.25}$$

where again $\hbar$ was set to 1 [7].
The quantity in the brackets is simply a linear combination of the creation and the annihilation operators. Indeed, using equations 2.1.22:

$$\begin{aligned}
i\hat{X}\hat{P} + i\hat{P}\hat{X} &= \frac{(\hat{a}+\hat{a}^\dagger)(\hat{a}-\hat{a}^\dagger)}{\sqrt{2}}\frac{(\hat{a}-\hat{a}^\dagger)(\hat{a}+\hat{a}^\dagger)}{\sqrt{2}} \\
&= (\hat{a})^2 - (\hat{a}^\dagger)^2.
\end{aligned} \tag{2.2.26}$$

Therefore 2.2.25 reads:

$$\frac{\partial}{\partial r}\psi_r(X) = \hat{G}\psi_r(X), \tag{2.2.27}$$

where the operator $\hat{G}$ was defined as $\hat{G} = \frac{1}{2}[(\hat{a})^2 - (\hat{a}^\dagger)]$.
Since $\hat{G}$ is a linear operator defined in a complex vector space (the Hilbert space), similarly to the derivation of the quantum mechanical propagator, the equation

$$\frac{\partial}{\partial r}\psi = \hat{G}\psi$$

could be proven has the solution:

$$\psi_r(X) = U(\hat{G})\psi(0). \tag{2.2.28}$$

Here $U(\hat{G})$ was defined as

$$U(\hat{G}) = e^{r\hat{G}}, \tag{2.2.29}$$

and it is unitary [31, 32].

Moreover the squeezing parameter is a generic complex number [7]:

$$\xi = re^{i\theta} \in \mathbb{C} \tag{2.2.30}$$

where now r is accounting for the effective squeezing in the quadratures while θ is relative to which quadrature is squeezed. Figure 2.6 effectively shows this principle.

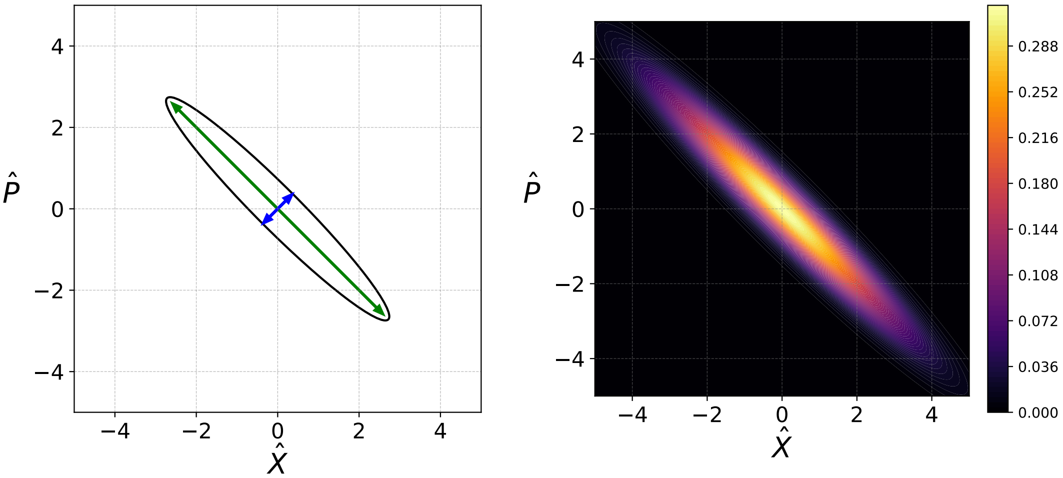

Figure 2.6: On the left is the representation of the squeezed vacuum wavefunction with squeezing parameter $r = 1$ and rotation $\theta = \frac{\pi}{4}$. As it is possible to observe both in the representation and in the probability distribution (right), the squeezing parameter is determining how much the variance of the two quadratures are different as in Figure 2.5, while the rotation parameter θ rotating the Wigner representation of the state.

As a last remark, since the squeezed states are minimum uncertainty states, once the squeezed (or anti-squeezed) variance is known, then the anti-squeezed (or squeezed) is too:

$$\Delta\hat{q}\Delta\hat{p} = \frac{1}{2}$$

since $\hbar = 1$.

Furthermore, since the squeezed quadrature has a variance that has to be lower than vacuum, it is possible to go below the shot noise, so the quantum limit.
As before anticipated, this feature can be exploited in applications such as quantum metrology or quantum sensing [8], but finds application also in quantum communication and quantum computing [9, 10, 15].

2.3 Quantum tomography

2.3.1 Quantum state tomography framework

Following the rules of quantum mechanics, a quantum state can not be directly observed. Instead, the measurement outcomes are associated with a set of projective operators $\{\hat{\Pi}_i\}$ and the outcome probabilities are given by Born's rule $p_i = \langle\psi|\hat{\Pi}_i|\psi\rangle$ This assumption comes from the fact that a generic state is defined as a linear superposition between the vectors of the representation basis:

$$|\psi\rangle = \sum_{i=0}^{n} a_i \, |\phi_i\rangle \, . \tag{2.3.1}$$

Knowing only the outcome probabilities $p_i = |a_i|^2$ in a single basis is not sufficient to fully determine the quantum state, since the relative phases $\arg(a_i)$ between coefficients a_i are lost. However, by performing measurements in several complementary bases, one can reconstruct the complete information encoded in the density matrix: [3]:

$$\hat{\rho} = |\psi_k\rangle \langle\psi_k| = \sum_{i,j} a_i a_j^* \, |\phi_i\rangle \langle\phi_j| \, . \tag{2.3.2}$$

The density matrix fully characterizes the quantum state, containing both the probabilities of measurement outcomes and the coherences between basis states. Therefore, the ability to reconstruct the density matrix allows for the description of all the properties of the system.

Indeed, if one wants to find the probability of observing the vector $|\phi_i\rangle$, and knows the density matrix of the state $\hat{\rho}$, it is necessary to look at the element in the density matrix at position (i,i); indeed:

$$\begin{aligned} \langle\phi_k| \, \hat{\rho} \, |\phi_k\rangle &= \sum_{i,j} \langle\phi_k| \Big(a_i a_j^* \, |\phi_i\rangle \langle\phi_j| \Big) |\phi_k\rangle \\ &= a_k a_k^* \, \langle\phi_k|\phi_k\rangle \langle\phi_k|\phi_k\rangle \\ &= |a_k|^2 = p_k. \end{aligned} \tag{2.3.3}$$

As a consequence, it follows that the density matrix is a square matrix where the diagonal elements correspond to the probability of finding the state $|\phi_i\rangle$. The off-diagonal elements, on the other hand, correspond to the quantum interferences of two states $\langle\phi_i|\phi_j\rangle$, therefore, at the cross-correlation between the two vectors. Moreover, it is possible to derive that a density matrix $\hat{\rho}$ has the following properties [3]:

i Semi-positive defined: $\langle\psi_i|\hat{\rho}|\psi_j\rangle \geq 0$;

ii Self adjoint: $\hat{\rho} = \hat{\rho}^\dagger$;

iii Have unitary trace: $\mathrm{Tr}(\hat{\rho}) = 1$;

The previously mentioned requirements are necessary to ensure non-negative probabilitie (i), Real diagonal elements (ii) and that those elements will sum up to one, ensuring the correct probability normalization (iii). Thus, in order to characterize a quantum state, the density or any other quantity that carries the same information must be evaluated.

This problem falls back into the field of tomography, which is tasked with recovering a complete set of information starting from partial data. In our case, we want to perform a quantum tomography, which recovers the full information of a quantum state or a quantum process [33, 34]. For the faithful recovery of the full information of a state, multiple acquisitions have to be performed [3, 35].

The recovery of quantum information can be schematized with the following diagram:

$$\text{unknown } \rho \longrightarrow \boxed{\text{algorithm}} \longrightarrow \tilde{\rho}$$

It is important to notice that, since the no-cloning theorem holds in quantum mechanics [36], there is no possibility to extract more that one measurement from one acquisition. As a consequence, experiments have to be made multiple times and each acquired point can contribute to one and only one measurement.

Ideally, following the statistical requirements, experiments have to be replicated multiple times for acquiring an accurate reconstruction of the density matrix. Since each measurement is subject to errors due to practical constraints (e.g. pollution from the environment), the number of measurements needed for characterizing the state increases depending on the error rate. Given then that one can accept an error of ϵ for any measurement, the total number of measurements that must be carried out have to be

$$n \sim \frac{d^2}{\epsilon^2}, \tag{2.3.4}$$

where d is the dimension of the density matrix $\hat{\rho} \in \mathbb{C}^{d \times d}$ that one wants to reconstruct [35], as shown in Appendix 6.8. Since the error will not go to zero due to experimental constraints, one aims to find a density matrix $\tilde{\rho}$ that approximates the effective density matrix $\hat{\rho}$ in the best possible way.

Once the minimum number of points is defined, suitable projection operators have to be determined. This set of projectors is known as POVMs [3] (Positive Operator Valued Measures, capable of measuring projections in one basis).

Let us consider a generic pure state vector $|v\rangle$ that lives in the complex Hilbert space $\mathbb{C}^d$. Since a complex vector of dimension d has $2d$ real parameters (one imaginary and one real coefficient) and the state vector must be normalized ($|\langle v|v\rangle|^2 = 1$), the vector is geometrically represented as a point on the real sphere S^{2d-1}. Physically, this means that every possible pure quantum state in the Hilbert space is represented by a unique point on a high-dimensional sphere.

When treating with a continuous set of states (such as the eigenvalues of the position or momentum operators), it is impossible to project against an infinite set of states. As a consequence, there will always be errors that are dependent on the size of the built space. This concept will be later explored in the Maximum Likelihood Estimation (MLE), since the dimension of the density matrix has to be set by input. In later chapters, it will be shown that, depending on the state to be characterized, different space dimensions will be required.

2.3.2 Wigner inverse transform

It is well established that the density matrix $\hat{\rho}$ contains all the information able to describe a quantum state.
Therefore, if one is able to reconstruct it, it will be also able to completely characterize a generic quantum state.
However the density matrix is not the only mathematical object having this feature. Other representations share the same property, for example the previously anticipated Wigner function, here described.
Since the Wigner function is represented in the phase space, identified by the $\hat{X}$ and $\hat{P}$ quadratures, fully characterizing the field, it is particularly suitable for describing quantum states of light.

One of the most commonly used tomographic algorithms for reconstructing the Wigner function is the Inverse Radon Transform (IRT).
The principle of this method is based on the Radon Transform (or Radon Integral). Specifically, by continuously changing the phase θ in the phase space, the complete set of probability distributions $P(X_\theta)$ is measured, providing the necessary data for tomographic reconstruction.
However, since the commutation relation $[\hat{X}, \hat{P}] = i$, an intrinsic uncertainty is present in the phase space, leading to the previously defined variances in the state representations. Consequently, a Wigner *distribution* ($W(X,P)$) is the natural representation of the quantum state in phase space and provides the joint *quasi-probability* of measuring the quadrature $X_\theta = X\cos\theta + P\sin\theta$. [7].
The reason why the word *quasi*-probability was used relies on the fact that the Wigner function can assume negative values (as in cat states or single photons) or be ill-behaved. It can be proven that the only states that are not showing negativities in the Wigner function must be Gaussian [37,38], while negative values are always referred to quantum features [39].
In Figure 2.9 are shown the expected Wigner functions of non-classical states (single photon and a cat states) compared to the vacuum one.
In particular one expects that, integrating the Wigner function along one quadrature will

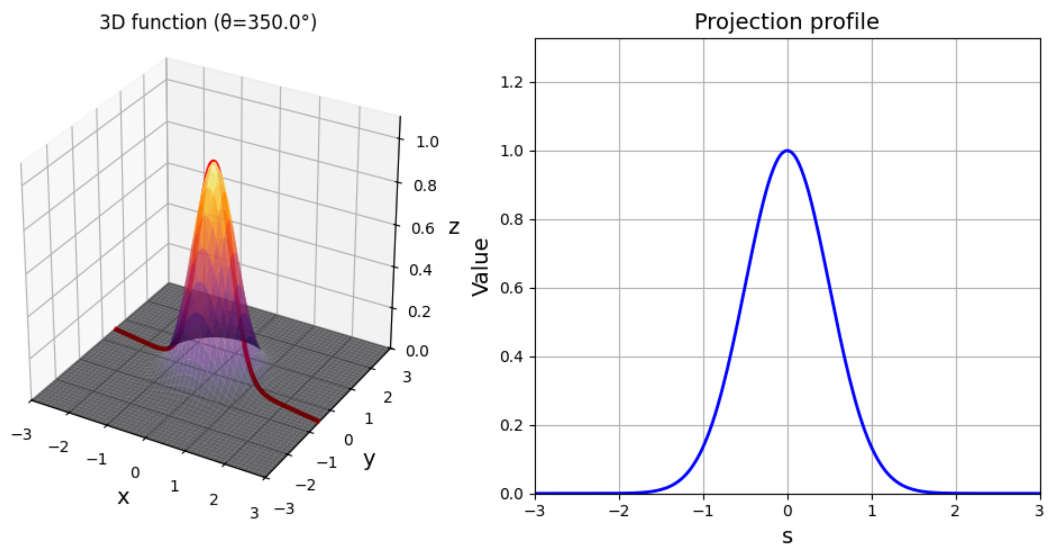

Figure 2.7: Above is shown the effect of the Radon Transform on a Gaussian Wigner function centred at the origin. As can be seen, the projection is simply the probability distribution of the measured quadrature, $P(X_\theta)$, for a specific phase angle θ. The parameter s represents the distance along the measurement axis X_θ with respect to the centre of the Wigner function.

result in the probability distribution in the orthogonal one (its marginal):

$$P(X) = \langle X|\,\hat{\rho}\,|X\rangle = \int_{-\infty}^{\infty} W(X,P)dP, \tag{2.3.5}$$

$$P(P) = \langle P|\,\hat{\rho}\,|P\rangle = \int_{-\infty}^{\infty} W(X,P)dX. \tag{2.3.6}$$

This property allows the Wigner reconstruction. Indeed, once all projections for any phase θ have been measured, the Wigner function can be recovered by combining all the marginals.

However, as before anticipated, the two quadratures are related by a phase difference. Therefore the θ dependent probability distribution can be defined as [7]:

$$\begin{aligned} P_\theta(X) &= \langle X|\,\hat{\rho_\theta}\,|X\rangle \\ &= \langle X|\,\widehat{\hat{U}_\theta \hat{\rho} \hat{U}_\theta^\dagger}\,|X\rangle \\ &= \int_{\mathbb{R}} W(X\cos(\theta) + P\sin(\theta), P\cos(\theta) - X\sin(\theta))\;dP = P(X_\theta), \end{aligned} \tag{2.3.7}$$

that is the previously mentioned Radon Integral.

Therefore, the Radon Transform is able to retrieve the marginal distributions given a Wigner function and, conversely, the IRT is able to recover the Wigner function starting from the projections:

$$\mathcal{R}[f(t,\theta)] = \int_{L_{t,\theta}} f(x)\, dS(x) = \int_{\mathbb{R}^2} f(x)\, \delta(\langle x, n_\theta \rangle - t)\, dx \qquad n_\theta = (\cos\theta, \sin\theta). \tag{2.3.8}$$

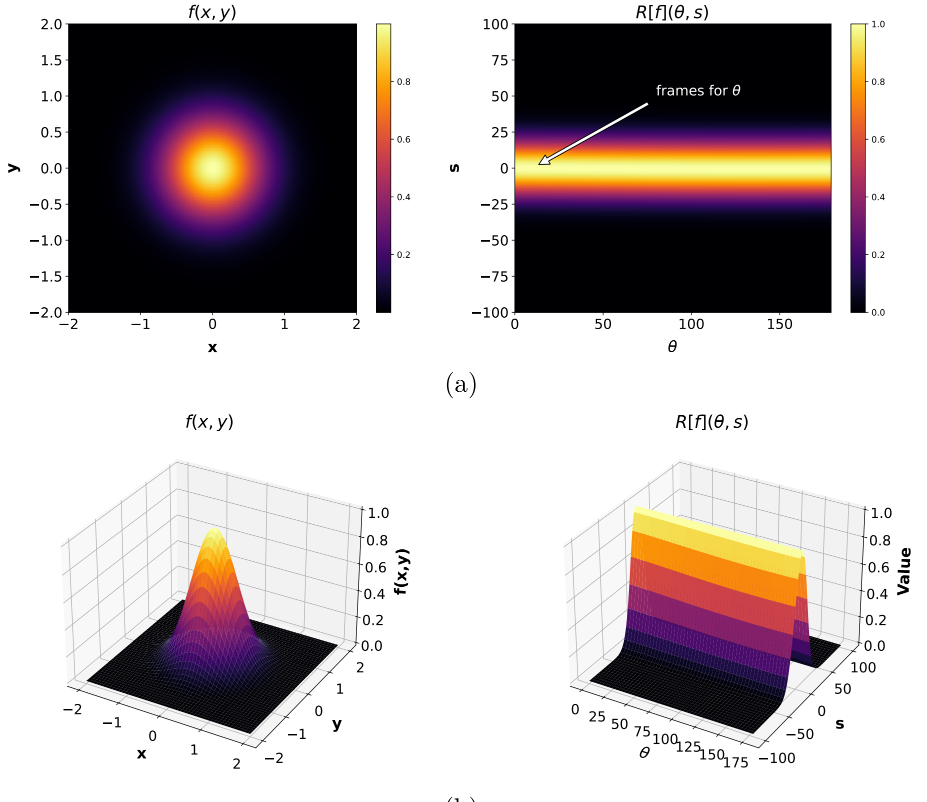

(a)

(b)

Figure 2.8: The relationship between the Radon Transform and the Inverse Radon Transform is illustrated above in two dimensions (a) and three dimensions (b). As can be seen, the Radon Transform is the mathematical operation that yields the multiple projections of the original function across different phases θ. Conversely, the Inverse Radon Transform performs the inverse process, reconstructing the original function from the ensemble of these projections.

This transformation is shown in Figures 2.7 and 2.8, its mathematical derivation can be found in Appendix 6.9 and reads as:

$$W(X,P) = \frac{1}{2\pi} \int_{-\infty}^{\infty} \langle X - \frac{v}{2} |\, \hat{\rho}\, | X + \frac{v}{2} \rangle\; e^{ivP}\, dv. \tag{2.3.9}$$

This transformation belongs to the class of Weyl transforms, which establish a correspondence between a quantum mechanical operator ($\hat{\rho}$) and its representation as a distribution in phase space ($W(X,P)$).

Therefore the procedure for evaluate $W(X,P)$ can be resumed as it follows:

i) obtain the probabilities from the experimental setup;

directly related to the distributions of the quadrature operators.

ii) Make the Fourier transform $\mathcal{F}$ of those outcomes;

allowing us to have the characteristic function χ then written in polar coordinates.

iii) Apply the Inverse Radon Transform $\mathcal{R}^{-1}$;

see Appendix 6.10. Different process will be required in the Maximum Likelihood Estimation experiment, where the density operator $\hat{\rho}$ is reconstructed, then used for evaluate the Wigner function.

Now that the Wigner function $\mathcal{W}(X,P)$ has been introduced, its main properties can be exposed. First, as stated above, it is a quasi-probability distribution in the phase space, able to encode all the meaningful information of the quantum state.
Secondly, it is a purely real function ($\mathcal{W}(X,P) = \mathcal{W}(X,P)^*$):

$$\begin{aligned}
W(X,P)^* &= \left[\frac{1}{2\pi}\int_{-\infty}^{\infty} \langle X - \frac{v}{2}|\,\hat{\rho}\,|X + \frac{v}{2}\rangle\; e^{-iPv}\,dv\right]^* && (2.3.10)\\
&= \frac{1}{2\pi}\int_{-\infty}^{\infty} \left(\langle X - \frac{v}{2}|\,\hat{\rho}\,|X + \frac{v}{2}\rangle\right)^* \left(e^{-iPv}\right)^* dv && (2.3.11)\\
&= \frac{1}{2\pi}\int_{-\infty}^{\infty} \langle X + \frac{v}{2}|\,\hat{\rho}^\dagger\,|X - \frac{v}{2}\rangle\; e^{iPv}\,dv && (2.3.12)\\
&= \frac{1}{2\pi}\int_{-\infty}^{\infty} \langle X + \frac{v}{2}|\,\hat{\rho}\,|X - \frac{v}{2}\rangle\; e^{iPv}\,dv \quad (\hat{\rho}^\dagger = \hat{\rho}) && (2.3.13)\\
&= \frac{1}{2\pi}\int_{-\infty}^{\infty} \langle X - \frac{v'}{2}|\,\hat{\rho}\,|X + \frac{v'}{2}\rangle\; e^{-iPv'}\,dv' \quad (v' = -v) && (2.3.14)\\
&= W(X,P), && (2.3.15)
\end{aligned}$$

Where $\hbar$ was set to unity, and the self adjointness of the density operator was used. However, the invariance under complex conjugation is a characteristic of Weyl transforms linked to an Hermitian quantum operator, as used in Eq. 2.3.13.
Moreover, we have [7]:

$$\mathrm{Tr}\Big[\hat{F}_1\hat{F}_2\Big] = \int_{-\infty}^{+\infty} \langle X|\hat{F}_1\hat{F}_2|X\rangle\, dX.$$

Due to the probabilistic meaning of the Wigner function, since in quantum mechanics, the expectation of an operator $\hat{A}$ acting on a system identified by $\hat{\rho}$ is given by $\mathrm{Tr}[\hat{A}\hat{\rho}]$, the Wigner function can be used for the calculation of those expectations ($\mathrm{Tr}[\hat{\rho}\hat{A}]$), or for the calculation of the joint probability ($|\langle\psi_1|\psi_2\rangle|^2$) [7].
The utilities of this property span between the quantum tomography to the quantum communication applications where, for instance, a qudit can be written with the two densities operators $\hat{\rho}_1$, $\hat{\rho}_2$ [40].

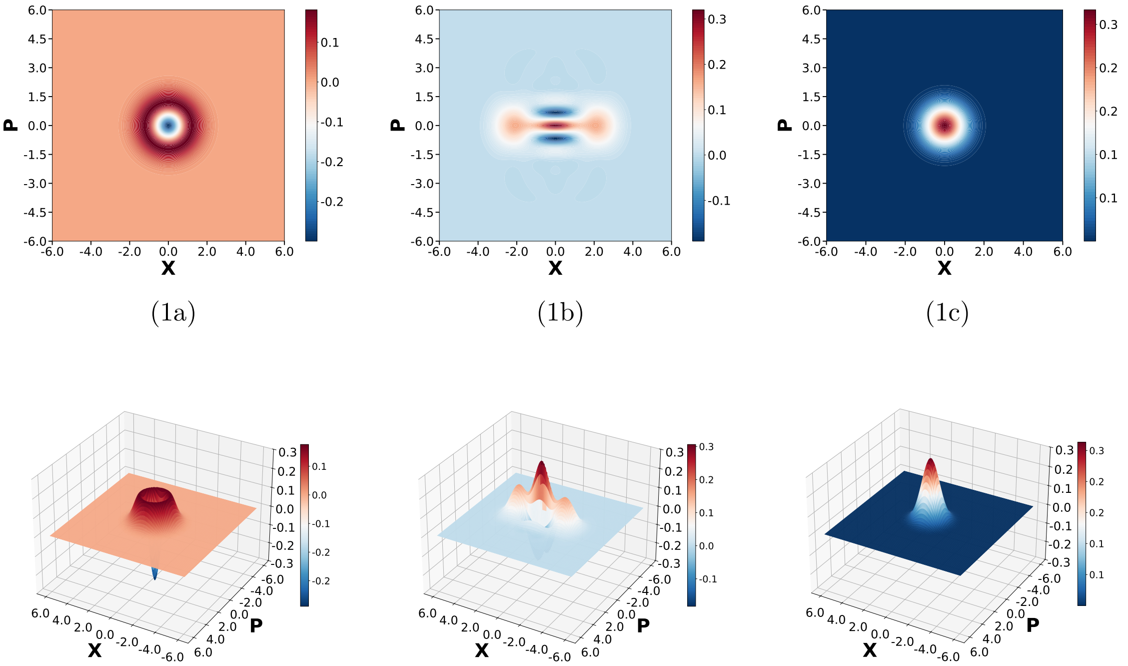

(1a) (1b) (1c)

(2a) (2b) (2c)

Figure 2.9: In the figure are shown the two-dimensional (1) and three-dimensional (2) simulated Wigner functions for a single photon (a), cat (b) and vacuum (c) states. The cat state was simulated by using a coherent parameter $\alpha = 1.5$ (if the cat state is defined as $|\psi\rangle = |\alpha\rangle \pm |-\alpha\rangle$) and even parity. Together with the single photon state, and in contrast with the vacuum state, both the cat and single photon Wigner functions shows remarkable negativities, as expected since quantum states.

Furthermore, since the density operator $\hat{\rho}$ have unity trace ($\mathrm{Tr}[\hat{\rho}] = 1$), then also the Wigner function have to be normalized ($\int_{-\infty}^{\infty} W(\hat{X}, \hat{P}) = 1$), similarly to a probability distribution.

Chapter 3

Quantum State Tomography: Setup and Experimental Characterization

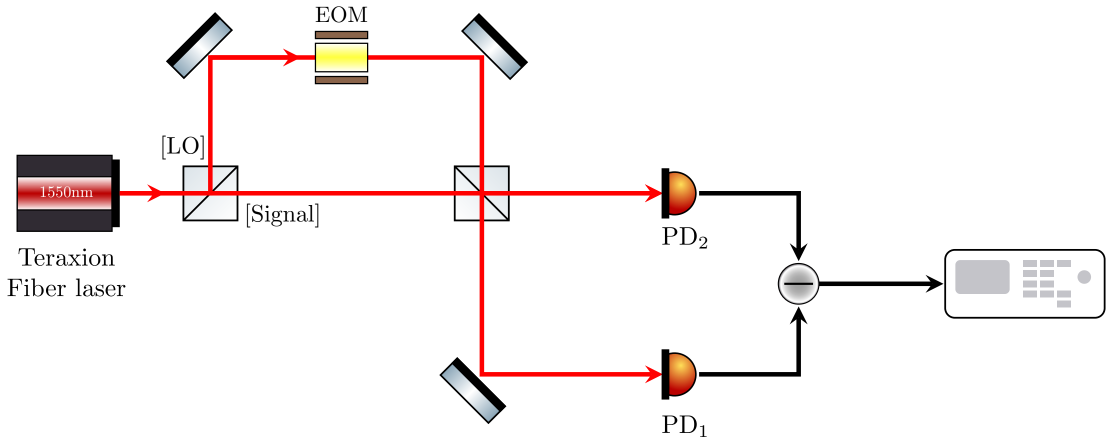

Figure 3.1: Experimental setup used for homodyne tomography. It consists of a standard balanced homodyne detection scheme.

The aim of this work is to reconstruct the Wigner function of a quantum state by measuring the quadrature probability distributions. A standard and well-established technique to perform such measurements is balanced homodyne detection [7,11]. Indeed, such setup enables the measurement of the previously defined marginal distributions in 2.3.7 :

$$P_\theta(X) = \langle X|\,\hat{\rho}_\theta\,|X\rangle = \langle X_\theta|\,\hat{\rho}\,|X_\theta\rangle\,, \tag{3.0.1}$$

where X_θ is the field quadrature at phase θ. The setup used in this work is presented in Fig 3.1.

The key optical component enabling such a measurement is a balanced beam splitter, which projects the signal field onto the basis of the Local Oscillator (LO), expected to be

a strong coherent field.
Indeed, the quantum mechanical beam splitter transformation in terms of the annihilation operators is given by:

$$\begin{pmatrix} \hat{c} \\ \hat{d} \end{pmatrix} = \frac{1}{\sqrt{2}} \begin{pmatrix} 1 & 1 \\ 1 & -1 \end{pmatrix} \begin{pmatrix} \hat{a} \\ \hat{b} \end{pmatrix}, \tag{3.0.2}$$

where $\hat{a}$ and $\hat{b}$ denote the input signal and LO mode, while $\hat{c}$ and $\hat{d}$ denote the outputs.

Therefore, if the two beam splitter outputs are read in a differential way, the resulting photocurrent can be evaluated as:

$$i_{-} = I_c - I_d \propto \hat{n}_c - \hat{n}_d = \hat{c}^{\dagger}\hat{c} - \hat{d}^{\dagger}\hat{d} = \hat{a}^{\dagger}\hat{b} + \hat{b}^{\dagger}\hat{a}. \tag{3.0.3}$$

Assuming that the LO field is a strong coherent state, $\hat{b} = |\beta|e^{i\theta} + \delta\beta$, and $|\beta| \gg 1$, the normalized differential current becomes

$$\hat{X}_{\text{meas}} = \frac{i_{-}}{|\beta|} = \frac{\beta^{*}\hat{a} + \hat{a}^{\dagger}\beta}{|\beta|} + \frac{\delta\beta^{\dagger}\hat{a} + \hat{a}^{\dagger}\delta\beta}{|\beta|} = X_{\theta} + R, \tag{3.0.4}$$

or $\sqrt{2}X_{\theta}$ if the $\frac{1}{\sqrt{2}}$ factor is considered in the quadrature definition. Here R collects the LO-induced noise, negligible in the limit of high LO power and phase stability ($\langle\delta\beta\rangle_{\rho} = 0$). In such conditions the measurement yields the quadrature operator X_{θ}.

The high power and the phase stability required are obtained by using an ultra-stable laser (Teraxion TNL162630) operating at 1550 nm as LO. The phase difference between LO and signal is obtained through an MPZ-N10 electro-optic modulator (EOM) driven by an Agilent 33522A AWG. A nearly 50/50 beam splitter (with estimated splitting ratio $\sim 51/49$) combines the two signal. The resulting beams are detected by an ultralow-noise photodiode (Exalos EBR370005-02), and the differential signal is acquired using a Tektronix MSO64 oscilloscope.

The system is implemented in polarization-maintaining (PM) fibres to ensure stable interference. However, none of the available 1550 nm laser sources in the laboratory exhibited sufficiently low phase noise in order to obtain a conclusive result when the signal did not come from the ultra-stable LO. As a consequence, only calibration states (vacuum and coherent states) have been characterized for now. For such reason, in the shown setup in Fig 3.1 the signal originates from the same laser source.
In particular a highly unbalanced beam splitter, followed by a polarizer (to equalize the polarization) was used to generate the signal. This approach was chosen due to the absence of a functional PM attenuator, but does not allow precise estimation of the absolute signal power.

Before presenting the acquisition techniques for the quadrature distributions, the characterization of the detector is reported since its noise and bandwidth are essential for a proper reconstruction.

3.1 Detector characterization

The calibration of the photodiodes, reported in this section, is important for a proper reconstruction. This procedure allowed us to understand whether the Exalos balanced photodiode was working properly.
In particular, as before stated, the shot noise and bandwidth characterizations were carried out. The shot noise, in particular, is expected to show a linear dependency with the power and will be crucial for the proper normalization of the phase space. On the other hand, the Power Spectral Density (PSD) gave us information about the electrical noise and about the frequency response of the photodiode.

3.2 Shot noise characterization

As before introduced, the shot noise characterization allowed us to understand whether the photodiode was measuring as expected. The measurement of the shot noise will be essential in later steps, since it acts as a normalization coefficient for the phase space, effectively normalizing the measured differential current. For instance, the squeezing (and anti-squeezing), are described having as a reference the vacuum standard deviation, therefore the shot noise. In particular, shot noise arises from the discrete nature of light and is therefore an intrinsically quantum noise source.

Indeed the photo-generated current can be evaluated as:

$$\langle i_{ph} \rangle = eR\langle N(t) \rangle, \tag{3.2.1}$$

where e is the electron charge, R is the responsivity and $N(t)$ is the number of photons dependent on the time.
On the other hand the power of the field can be expressed as:

$$P = \frac{\langle N(t) \rangle h\nu}{t} \tag{3.2.2}$$

if t represents the time.

If a coherent field is considered, then the photons must arrive with a Poissonian distribution.
Since for a Poissonian distributed random variable the following properties holds:

$$\mathbb{E}(X) = \langle X \rangle \tag{3.2.3}$$
$$\mathrm{Var}(X) = \langle X \rangle \qquad\qquad X \sim \mathcal{P}, \tag{3.2.4}$$

if $\langle X \rangle$ identify the expected value, recalling that $\mathrm{Var}(cX) = c^2\mathrm{Var(X)}$, if c is a real number, one obtains:

$$\begin{aligned} \mathrm{Var}(i_{ph}) &= (eR)^2\mathrm{Var}(\langle N(t) \rangle) \\ &= (eR)^2 \frac{P\Delta t}{h\nu} \propto P. \end{aligned} \tag{3.2.5}$$

Therefore, for a coherent field, if the device is properly working, one should expect a linear increase of the measured noise power as the intensity of the laser increases, if the shot noise is dominant on other noise sources.
The achieved results for the Exalos photodiode varying the input power are reported in Figure 3.2.

In order to properly measure the shot noise, it is essential to distinguish it from electrical one. Indeed, by using photodiodes and other electronic equipment, there is always some background noise due to dark currents or other non-idealities. If multiple noise sources are present in the system, the total measured noise will be dominated by the largest one. For instance, this is the reason why ultra-low noise photodiodes were used.
Increasing the input power, the shot noise dominance can be further improved. For such reason, the used optical power in the experiment exceeded the maximum limit specified in the photodiode datasheet (–4 dBm per input). Therefore, the electronic noise is further negligible.
However, exceeding the maximum power can lead to saturation effects, as the detector can not maintain linearity while providing the differential current. This introduces non-idealities and potential errors. Nevertheless, this operation did not compromise the reliability of the results. Indeed, following an idea suggested by Dr. Guillaume Richard from our laboratory, the datasheet limit appears to be mainly related to the differential voltage output of the Exalos, crucial in unbalanced detections; the opposite situation of this experiment. Indeed, such effects were not recorded.

3.3 Frequency response

The second characterization that was carried out was the PSD evaluation of the photodiode. This analysis provides the noise profile of the detector besides its bandwidth.

Since a phase modulation will be induced, the knowledge of the bandwidth of the detectors is crucial for the correct implementation of the experiment: since the phase modulation is converted into an amplitude modulation through interference, the modulation frequency must remain below the 3 dB bandwidth of the photodiode.
Otherwise, aliasing and distortion effects may occur in the recorded traces, thereby perturbing the measurement.
A bandwidth of 350 MHz was estimated for the used photodiodes, as shown in Figure 3.3, accordingly to what stated in the datasheet.
Such low bandwidth will be problematic later on since, as before already anticipated, the phase diffusion of the quantum well laser occurs at an high frequency.

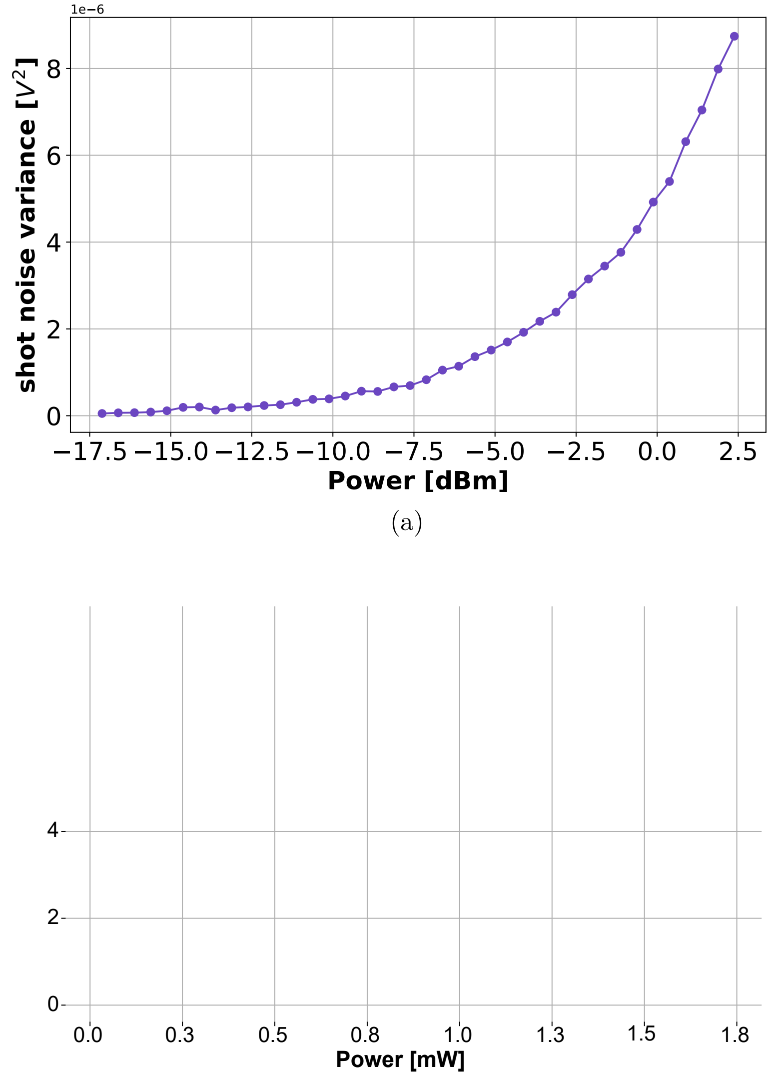

(a)

(b)

Figure 3.2: In the figure above, the shot-noise variance is plotted for different optical powers. Since the electronic noise was found to be constant, the shot noise was normalized to it, which is represented as the reference level at zero. Each point corresponds to an acquisition of 500,000 samples, recorded at a sampling rate of 25 GSa/s over a total acquisition time of 2 μs. Image (b) shows the variance as a function of optical power in mW, clearly exhibiting the expected linear behaviour. Conversely, in Figure (a), where powers are reported in dBm, the trace appears exponential. From panel (a), it can be observed that up to approximately -7.5 dBm the measured variance remains close to the electronic noise reference (0 level), indicating that the electronic contribution is still comparable to the shot noise, although the shot noise is already dominant. The displayed powers should be considered for a single input of the Exalos photodiode.

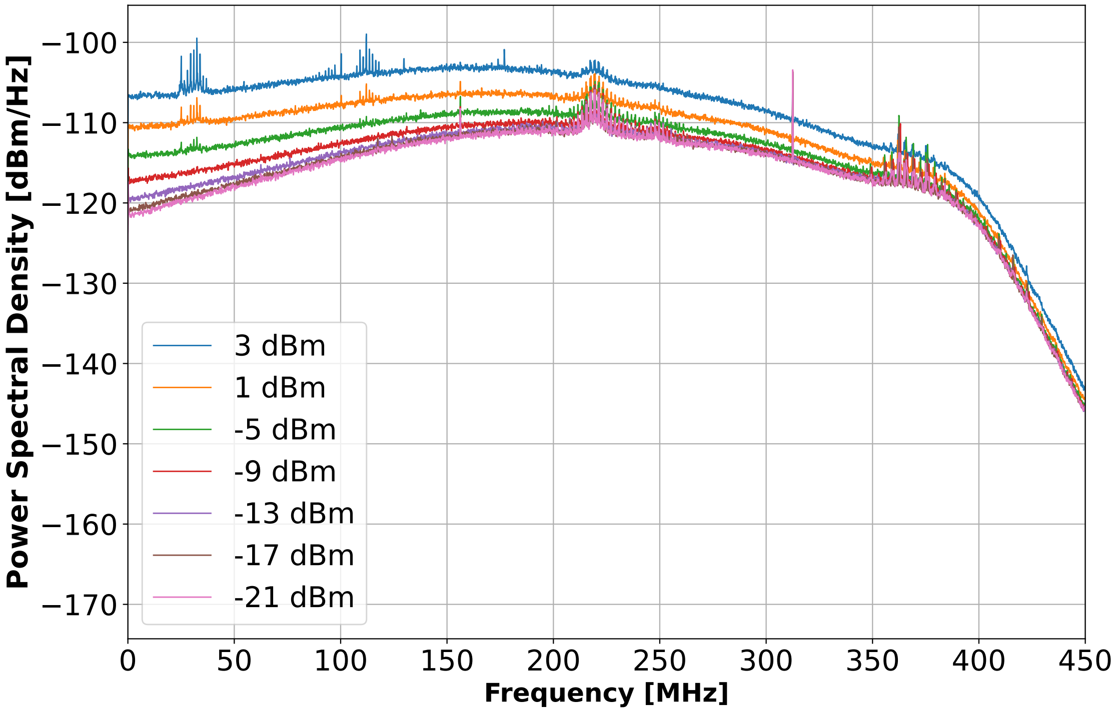

Figure 3.3: In the panel, the frequency response of the Exalos photodiode at multiple optical powers is reported. As expected, the Power Spectral Density (PSD) increases with the input optical power. Each trace was acquired with a Sampling Rate of 25 GSa/s and an acquisition time of 2 μs, corresponding to 500,000 samples per trace. The measured bandwidth is approximately 350 MHz, in good agreement with the value reported in the datasheet.

Chapter 4

Quantum state tomography: Inverse Radon Recovery

As previously mentioned, this work is divided into two main experiments: the Inverse Radon reconstruction, analysed in this chapter, and the Maximum Likelihood Estimation exposed in the next one.

As shown in Chapter 2.3, the IRT is able to reconstruct the Wigner function of a quantum state, provided that the probability distributions of the quadratures are known for all phases θ; defined as the phase difference between the Local Oscillator and the signal.
Those probabilities can be obtained, up to a normalization constant, using the previously described Balanced Homodyne Detection (BHD) setup, provided that a stable laser with high output power interferes with the signal to be characterized.

In particular, for strong classical fields, given E_1, E_2 as the two input fields, the two outputs can be calculated as:

$$\mathcal{E}'(t) = E_1(t) + E_2(t) = A_1 e^{i(\omega_1 t + \phi_1)} + A_2 e^{i(\omega_2 t + \phi_2)},$$
$$\mathcal{E}''(t) = E_1(t) - E_2(t) = A_1 e^{i(\omega_1 t + \phi_1)} - A_2 e^{i(\omega_2 t + \phi_2)},$$

resulting in two photo-generated currents that read:

$$i_{1,2}(t) \propto |\mathcal{E}_{1,2}|^2 = |A_1|^2 + |A_2|^2 \pm 2|A_1||A_2| \cos(\Delta\omega t + \Delta\phi). \tag{4.0.1}$$

Here, $\Delta\omega$ represents the frequency difference between the two fields, while $\Delta\phi$ represents their phase one. In particular, the phase difference θ in the quadrature definition, is determined by both these quantities.

The phase stability characterization of the Teraxion laser was kindly given by Dr. Huang Heming, and it is reported in Figure 4.1.
Moreover, both the In phase (I) and in Quadrature (Q) components coming from the coherent interference of the Local Oscillator beating with itself were recorded, by using

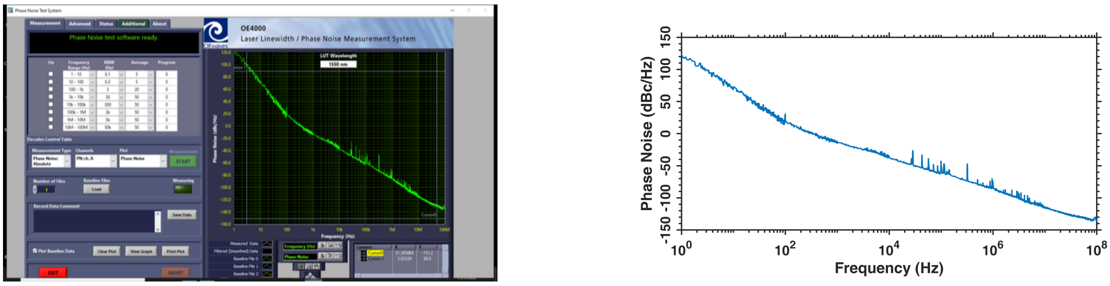

(a)

(b)

Figure 4.1: In the figure above, the Teraxion TNL162630 phase noise characteristics are shown. The plots were kindly given by Heming Huang that obtained them through the Teraxion calibration using an OE4000 laser noise analyser. Both Teraxion operative regimes, native mode (a), and low noise mode (b) were analysed, showing respectively a linewidth of 2.5KHz and 300Hz. Such ultra-low linewidth of this laser is crucial to correctly track the phase and manipulate it in a known way.

a Kylia IQ decoupler.
By making use of:

$$\mathcal{E}(t) = \mathrm{I(t)}\cos\theta + \mathrm{Q(t)}\cos\theta, \tag{4.0.2}$$

and using the trigonometric identity:

$$\cos(\alpha+\beta) = \cos\alpha\cos\beta \ - \ \sin\alpha\sin\beta, \tag{4.0.3}$$

it is possible to obtain:

$$i_- \propto i_{dc} + I(t)\cos(2\pi\Delta f t) + Q(t)\sin(2\pi\Delta f t). \tag{4.0.4}$$

Therefore:

$$I(t) \propto \cos(\Delta\phi(t)), \tag{4.0.5}$$

$$Q(t) \propto \sin(\Delta\phi(t)). \tag{4.0.6}$$

Moreover, if I_0 is the constant amplitude of the In phase signal and Q_0 the in Quadrature one, it is possible to see that:

$$\begin{cases} \frac{I(t)^2}{I_0^2} = \cos\Delta\Phi^2 \\ \frac{Q(t)^2}{Q_0^2} = \sin\Delta\Phi^2 \end{cases} \implies \frac{I(t)^2}{I_0^2} + \frac{Q(t)^2}{Q_0^2} = \cos\Delta\Phi^2 + \sin\Delta\Phi^2 = 1 \tag{4.0.7}$$

So if $\mathrm{I}_0 = \mathrm{Q}_0$ the phase θ of the field can be derived as:

$$\theta = \arctan\frac{\mathrm{I(t)}}{\mathrm{Q(t)}} \tag{4.0.8}$$

and by plotting I(t) versus Q(t) (so moving to the phase space) a circle is expected, where each radial component is associated to a certain phase θ:

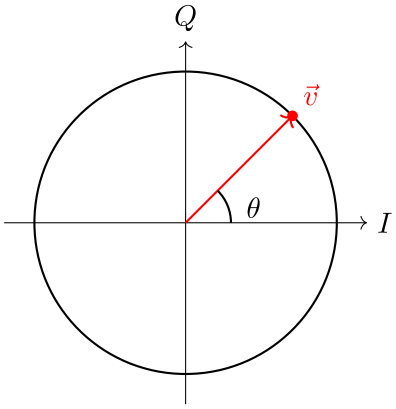

$$\vec{v}_I = \vec{v}\cos\theta$$
$$\vec{v}_Q = \vec{v}\sin\theta$$

This procedure, with the extraction of the phase, is usually referred as software PLL (Phase Locked Loop), since it is able to sense the phase of the field at each time.
The results for the self interference of the Teraxion TNL162630 with a triangular phase modulation between 0 to π, is shown in Figure 4.2.
A very clear plots are visible in the Figure, because of the ultra-low linewidth of the Local Oscillator ($\sim$ 300 Hz), resulting in a coherence time of $\sim$ ms. A little unbalance between the I(t) and Q(t) is reflected in the phase space plot as an ellipse instead of a circle.

Now that the setup was proven working fine, and that the stability of the Local Oscillator was shown, the last preliminary measurement can be carried out before the measurement of coherent and vacuum states: the shot noise estimation.
Such evaluation can be split in several passages, summarized in Figure 4.3:

i. Measure electronic noise;

Then both the Local Oscillator and the signal branches were switched off, from now on referred to as off_trace. This procedure is needed in order to evaluate the residual noise (coming from dark-current in the photodiodes, drifting of the lasers etc) that can pollute the measurement. Thus, from this measurement, it will be possible to extract the ground electronic variance σ_{el}^2.

ii. Measure vacuum state;

So turn on only the Local Oscillator branch in order to measure the vacuum state (no light in the signal), from now on referred as lo_trace. This measurement allow us to measure the shot noise σ_{shot}^2 by comparing its variance with the previously evaluated σ_{el}^2.
This noise is dependent on the power of the Local Oscillator, thus from now on the Local Oscillator power has to be supposed constant.
In particular, for all this experiment the power of the LO at the input of the interfering beam splitter was around 1 dBm.

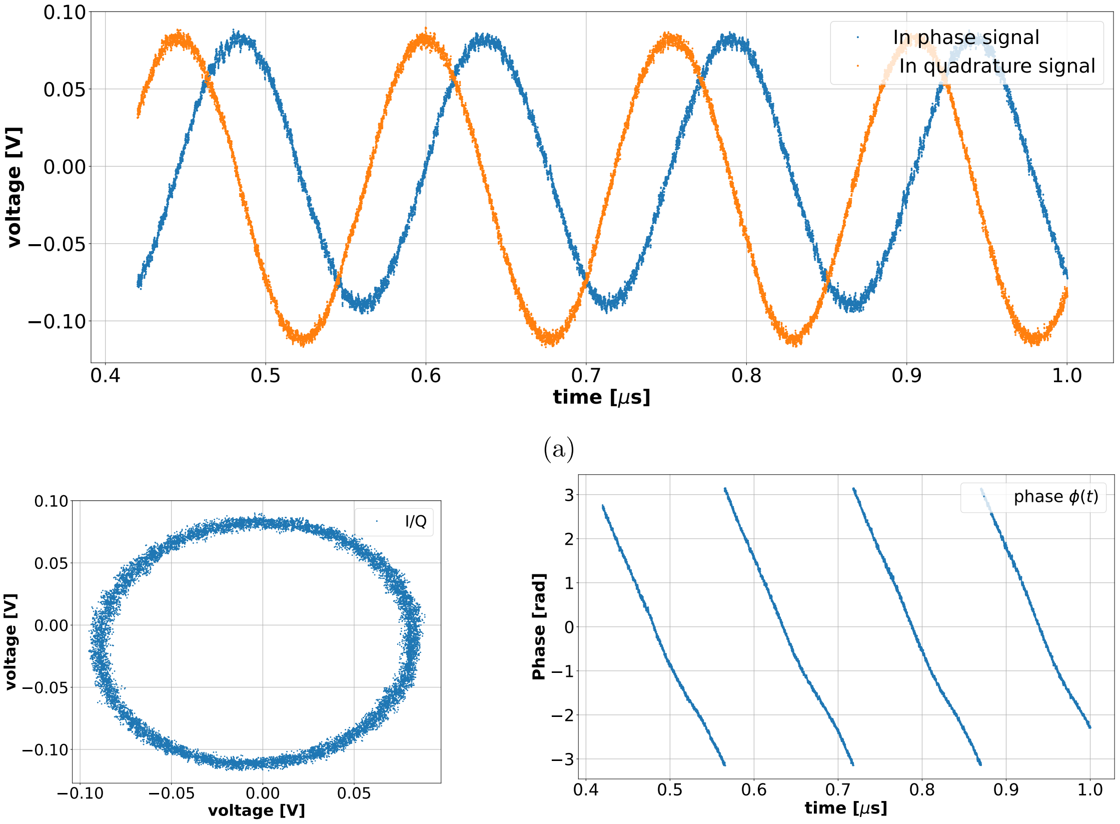

(a)

(b)

(c)

Figure 4.2: In the figure above are shown the achieved traces of the Teraxion TNL162630 laser interfering with itself both for the In-phase (I) and the in-Quadrature (Q) components, after a triangular modulation between 0 and π at $\sim$ 300 KHz was applied (a). As can be seen, the traces are cosinusoidal (as expected from the interference) and no phase pollution was measured. This is also clearly visible by the results of a Phase Tracking algorithm (c), where the phase was unwrapped, and in the In-phase versus the in-Quadrature component plot (b).

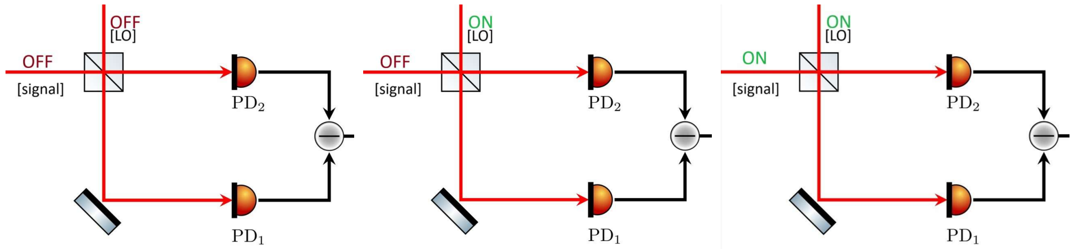

(a) (b) (c)

Figure 4.3: In the figure is shown the process for the data acquisition before the tomographic algorithm starts. Firstly, the electronic noise is evaluated by setting to off both the Local Oscillator and the signal (a). Then the shot noise is evaluated by comparing this measurement with the vacuum state (b) while the effective signal can be obtained by switching on also the signal branch (c).

iii. Measure coherent noise;

By turning on also the signal branch with a coherent field, from now on referred as on_trace (that has to be normalized) the coherent state quadrature probabilities can be evaluated.
The process is schematized in Figure 4.3.

Once the normalized data are achieved, the on_trace is split in many segments where the phase difference was supposed constant (in order to retrieve a projection for a given θ). Then, for each segment, a histogram is computed. It is also important to notice that the normalization procedure eliminates the proportionality constants arising from the photodiode responsivity and the model description. Indeed, this constant is common to both the coherent and vacuum acquisitions.
As will be shown later, two parameters play a crucial role in this step: the number of bins used for each histogram, which determines the resolution of the trace at a given phase, and the number of phase segments, which defines how finely the overall trace is divided. It is also essential to ensure that each histogram contains a sufficient number of data points per bin to provide a reliable statistical estimate, and that adjacent phase segments do not average out, as this could blur the phase-dependent features of the distribution.
As will become clear later, both the trace and the histogram analysis already provide information about the measured state, since they are related to the probability distributions.
However, the Wigner transform offers a complete characterization, yielding all the necessary information about the quantum state.

The data organized in such a way are called *sinograms*: a two-dimensional array in which each row corresponds to a histogram for a fixed phase. Then the `iradon` function from the Python library `skimage.transform` was used for the reconstruction.

Due to its mathematical nature, the IRT is not requiring for the physicality of the measured data, since it is a purely mathematical algorithm (see Appendix 6.10). Then both the shot noise division and the histogram normalization could not be enough to properly normalize the dataset. For this reason, a second normalization was executed directly on the evaluated Wigner function in order to normalize its integral to one.
In the following section, several simulations were performed to test the functionality of the code. These simulations also provided insight into its limitations and the ways in which non-idealities can perturb the measurements.

4.1 Numerical simulations

Before analysing the data coming from real measurements, ideal simulations were performed. This procedure allowed us to test whether the implemented tomography algorithm was properly working, letting us moreover explore its criticalities and limitations. Therefore, ideal data were generated through a Python script for different phases and then fed into the software. The resulting outputs were analysed for different quantum states of light. The statistical properties of each state were simulated using the `numpy` library, reproducing the expected quadrature distributions associated with each state.

Since the main goal of this work was to sense if squeezed light was emitted by a quantum well laser driven with a quiet pump, only the vacuum, coherent and squeezed Wigner functions were simulated.

However, the IRT is a general algorithm that can be applied for the reconstruction of any state of light, provided that the probability distributions for each quadrature $\hat{X}_\theta$ are known. In order to not be redundant, the limitations of the algorithm were analysed once (in the vacuum state).

Moreover, the ideal simulations will assume an already normalized dataset. Indeed, the trace can be already generated with a proper normalization.

As later explained, different variables were varied, such as the coherent parameter α for coherent states, and the squeezing parameter r for squeezed states.

Following the previously used order, firstly the vacuum, followed by the coherent and squeezed states were analysed.

4.1.1 Vacuum state

The vacuum state represents one of the fundamental states of light, since it defines the shot noise level, as previously discussed.
As noted in Section 2.2, it corresponds to a mean photon number of $|\alpha|^2 = 0$, as no photons are present. The associated Wigner function in phase space is expected to exhibit a Gaussian-like profile with mean value $\mu = 0$ and variance $\sigma^2 = 0.5$, accordingly to Eq. 2.2.6.

Defined a certain number of points, and a certain number of phases as input parameters, the trace was then generated. Therefore, all the points were divided into subgroups and a constant phase was associated to each of them (spanning between 0 and π).
Since vacuum state is phase independent, then the same distribution were assigned for each quadrature projection.
In principle, the higher the used number of phases and the more accurate the resulting plot will be, since more projections (therefore information) are present in the dataset. However, if one supposes a fixed number of points, two issues may arise:

- The higher the number of phases, the fewer the points available for each phase. This leads to a bad behaved distribution of the field for fixed phase, introducing errors in the reconstruction.
- The higher the number of phases, the greater the required computational resources.

Moreover, since a finite number of points can be simulated (and measured), there will be always an error during the reconstruction.
A similar problem occurs with the number of bins, i.e. in how many parts each segment of fixed phase is divided. In Figures 4.7 and 4.8 these limitations are analysed.

In Figure 4.4 the simulated trace, together with the histograms calculation, are presented. The shown trace and histograms were reconstructed by dividing a simulated trace of 10^7 points in 5000 pieces, and normalized histograms were built using 70 bins for each constant phase segment.

The Wigner function, both from two-dimensional and three-dimensional perspectives, is shown in Figure 4.5. The plots clearly resemble Gaussian functions centred at the origin of the phase space, with a standard deviation of $\sigma^2 = \frac{1}{2}$.

The last parameter relevant to the IRT analysis is the *filter*, which acts on the filtered back-projections. Its presence naturally arises from the underlying working principle of the algorithm (see Appendix 6.10).

Therefore, the filter must be directly applied to the probability distributions p_θ, and its effect can be expressed as:

$$\tilde{q}_\theta(\omega) = H(\omega)\, \tilde{p}_\theta(\omega), \tag{4.1.1}$$

where $\tilde{q}_\theta(\omega)$ denotes the filtered Fourier transform of the probability distribution $p_\theta(s)$.

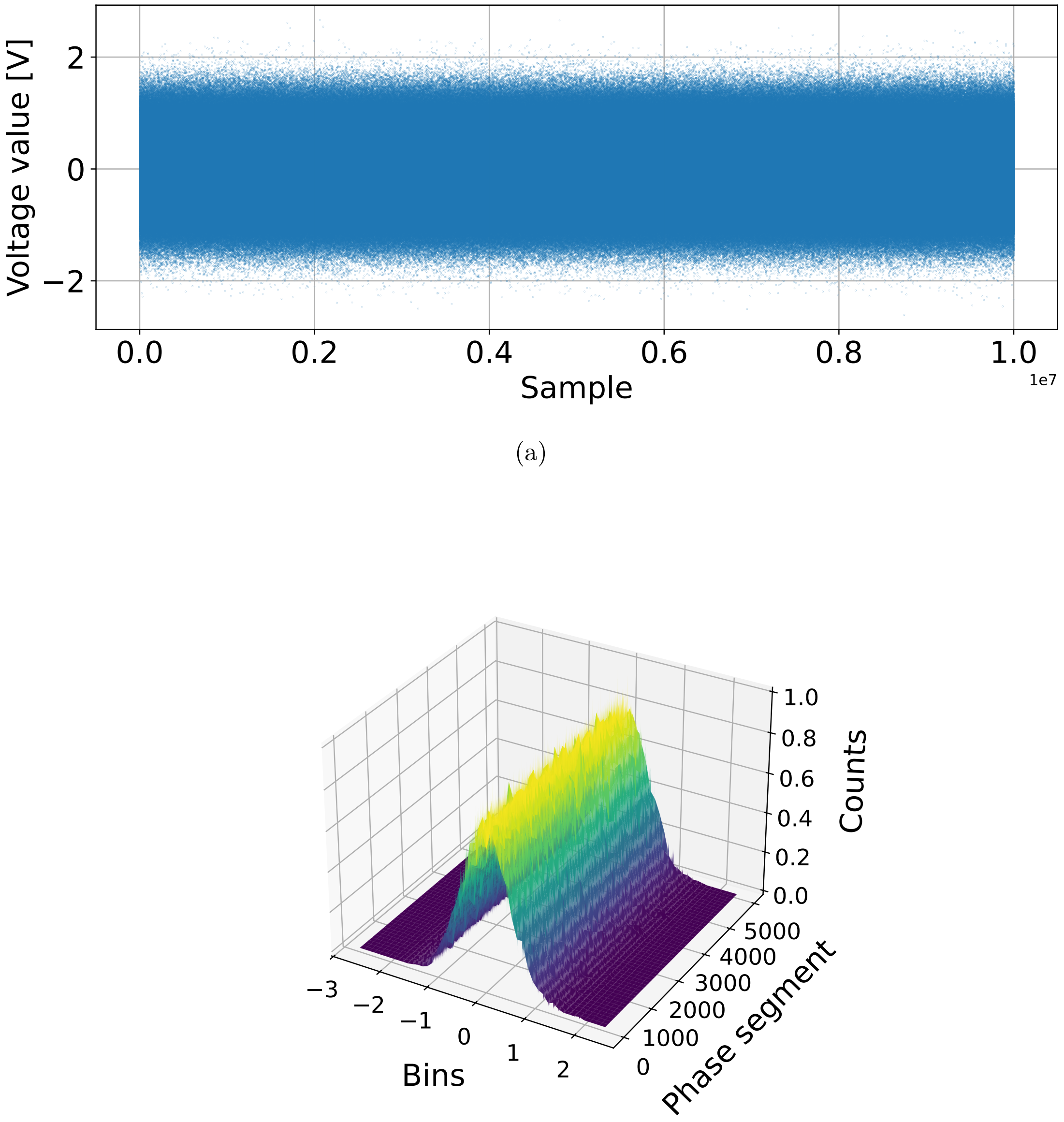

(a)

(b)

Figure 4.4: In the figure is shown the simulated trace (a) and the evaluated histograms (b) for the vacuum state. A total of 10^7 points were generated, then separated in 5000 different segments where the phase was considered constant. As clearly visible, the trace is showing the same variance for every phase and its mean value is zero, as predicted from the theory. The histograms show similar characteristics, being centred at zero with a Gaussian distribution as expected. For any of the 5000 segments 50 bins were used to evaluate the statistic of the field.

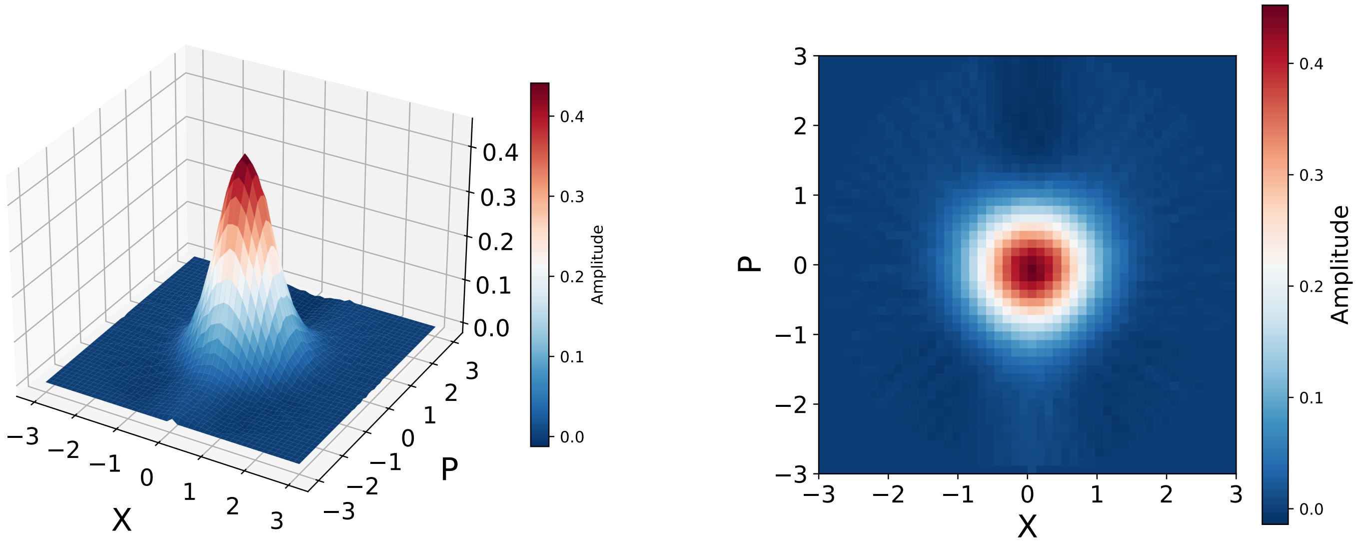

(a)

(b)

Figure 4.5: In the image above, the reconstructed Wigner function is shown both from a three-dimensional (a) and two-dimensional (b) perspective. As can be observed, the result is a Gaussian-like function centred in the origin of the phase space. The tails of the Gaussian vanish far from the central peak, which is located at $\frac{1}{\pi}$, in agreement with theoretical expectations. Again the simulation was performed using a total of 10^7 points, divided into 5000 phases, with 70 bins per phase, and employing a Hann filter.

The standard filter necessary to compute the IRT is the Ram-Lak filter, defined as $H(\omega) = |\omega|$, and directly arises from the change to polar coordinates. If this factor is omitted, the reconstructed image exhibits systematic distortions, as $|\omega|$ provides the correct spectral weighting of the high-frequency components during polar integration.

In fact, when performing integration in polar coordinates, higher frequencies correspond to larger circular paths in the Fourier domain, containing a greater number of sampling points. Consequently, their contribution must be properly weighted. The multiplicative factor $|\omega|$ compensates for this geometric effect by ensuring that each frequency contributes proportionally to its circumference in Fourier space. If this factor is neglected, high-frequency components become under represented, leading to a blurred or distorted reconstruction.

However, the Ram-Lak filter is not the only filter applicable in the IRT. While it corrects for the intrinsic weighting of the transformation, it also tends to amplify high-frequency noise. To compensate for this, smoother filters are often employed, such as the

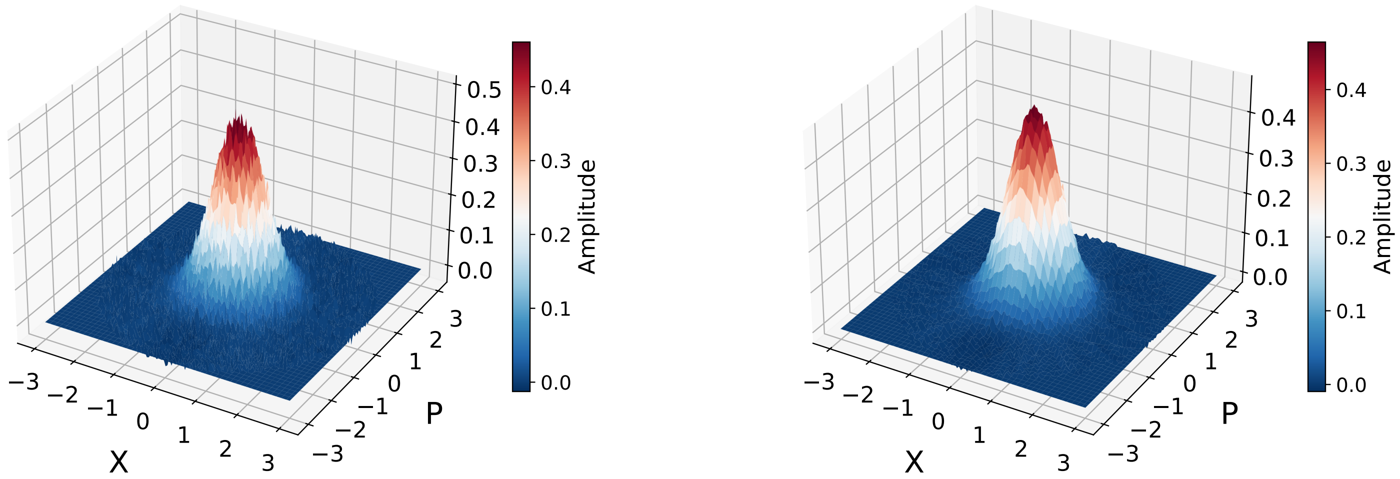

(a)

(b)

Figure 4.6: The figure above shows the simulated Wigner reconstruction for the vacuum state using the Ram-Lak (a) and the Hann (b) filters with 10^7 points divided into 5000 phases and 150 bins per phase. As expected, the Ram-Lak filter introduces high noise components, while the Hann allows for a smoother reconstruction. The risings, and the cutoff frequency, are clearly visible when the Ram-Lak filter was applied. In contrast, the Hann filter effectively suppresses these effects, allowing for a smoother reconstruction.

Hann filter, defined as:

$$H_{\text{Hann}}(\omega) = |\omega|\,\alpha(\omega), \qquad \alpha(\omega) = \begin{cases} \frac{1}{2}\left[1 + \cos\left(\frac{\pi\omega}{\omega_c}\right)\right], & |\omega| \le \omega_c, \\ 0, & |\omega| > \omega_c, \end{cases} \tag{4.1.2}$$

where $\alpha(\omega)$ is the Hann window and ω_c denotes the cutoff frequency of the filter. Another commonly used option is the *Hamming* filter, defined as:

$$H_{\text{Hamm}}(\omega) = |\omega|\,\beta(\omega), \qquad \beta(\omega) = \begin{cases} 0.54 + 0.46\cos\left(\frac{\pi\omega}{\omega_c}\right), & |\omega| \le \omega_c, \\ 0, & |\omega| > \omega_c, \end{cases} \tag{4.1.3}$$

where $\beta(\omega)$ is the Hamming window and ω_c again represents the cutoff frequency.

The back-projection (BP) can then be viewed as a convolution between the filter and the radial component $\frac{1}{r^2}$ and a typical non-ideality that often arises when applying a filter—especially the Ram-Lak filter—can be described as:

$$G(\Omega) \propto H(\omega)\left[\frac{\sin(\Omega r)}{r} + \cdots\right], \tag{4.1.4}$$

where the term $[\cdots]$ indicates higher-order corrections (see Appendix 6.11). This expression shows that the behaviour of the filter near the cutoff frequency ω_c strongly affects the reconstruction, producing oscillations in the final Wigner function, usually referred to as *ringing*.

Figure 4.6 shows the reconstruction of a vacuum Wigner function using 10^7 points and 5000 phases, comparing the results obtained with the Ram-Lak and Hann filters. As can be observed, the Ram-Lak filter preserves finer details but also introduces higher noise, whereas the Hann filter, being more aggressive, effectively suppresses the ringing artefacts. Therefore, the choice of filter is crucial and must be adapted to the dataset in order to achieve the best possible reconstruction.

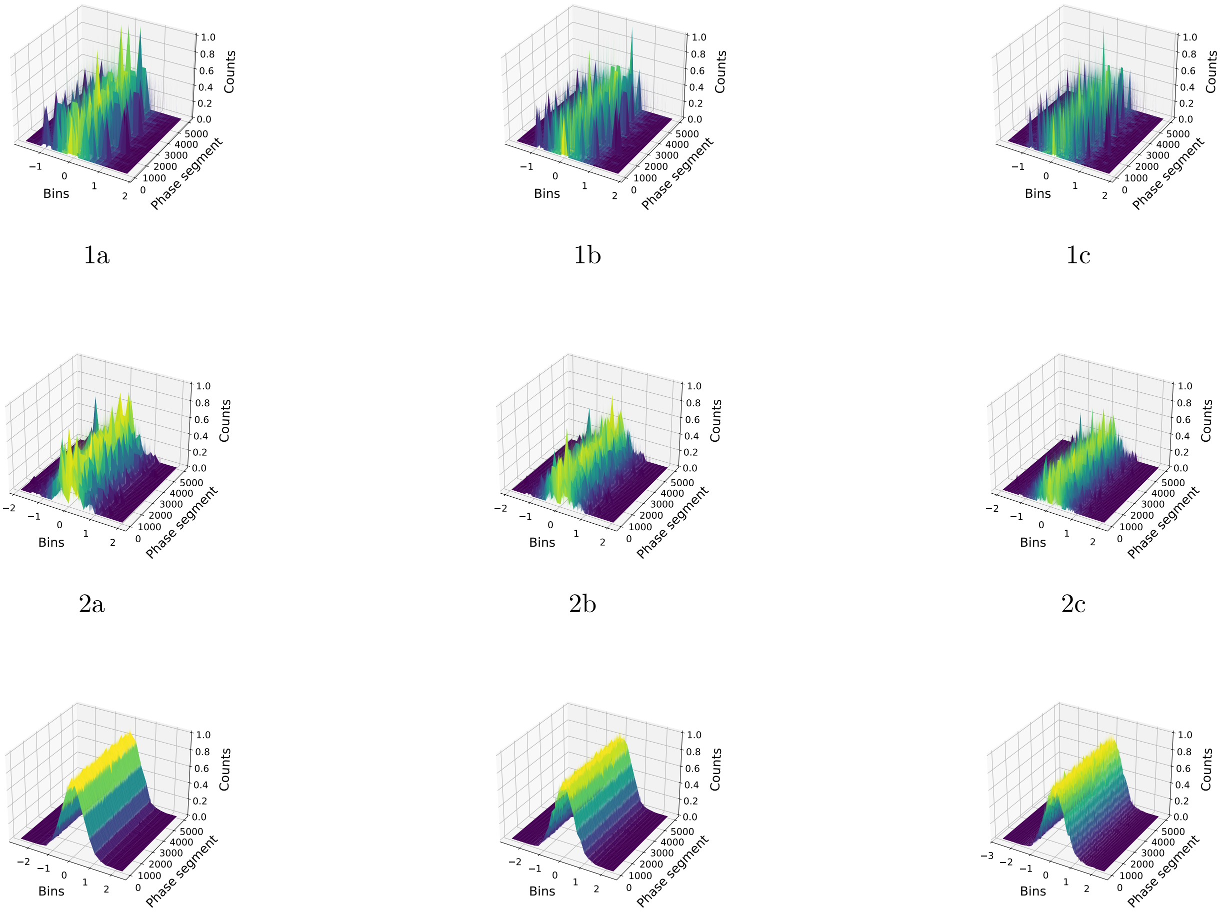

1a 1b 1c

2a 2b 2c

3a 3b 3c

Figure 4.7: In the figure, the results of the histogram reconstruction of the vacuum state are shown, varying both the number of points and the number of histogram bins. Specifically, figures 1, 2, and 3 were obtained using 10^4, 10^5, and 10^7 points, respectively, while figures a, b, and c within each series correspond to 20, 35, and 50 bins, respectively. For all plots, a total of 5,000 phases were used to define the segments.As can be seen, using too few points ($\lesssim 10^5$) leads to a bad histogram reconstruction, since there are not enough points per constant phase segment to reliably derive the required statistics. The same issue arises when the number of bins is too high (e.g., Figures 1c and 2c), whereas the best results are obtained using 10^7 points. This optimal balance must be determined for each Wigner reconstruction and acquisition, as it depends on both the number of data points and the data's phase distribution.

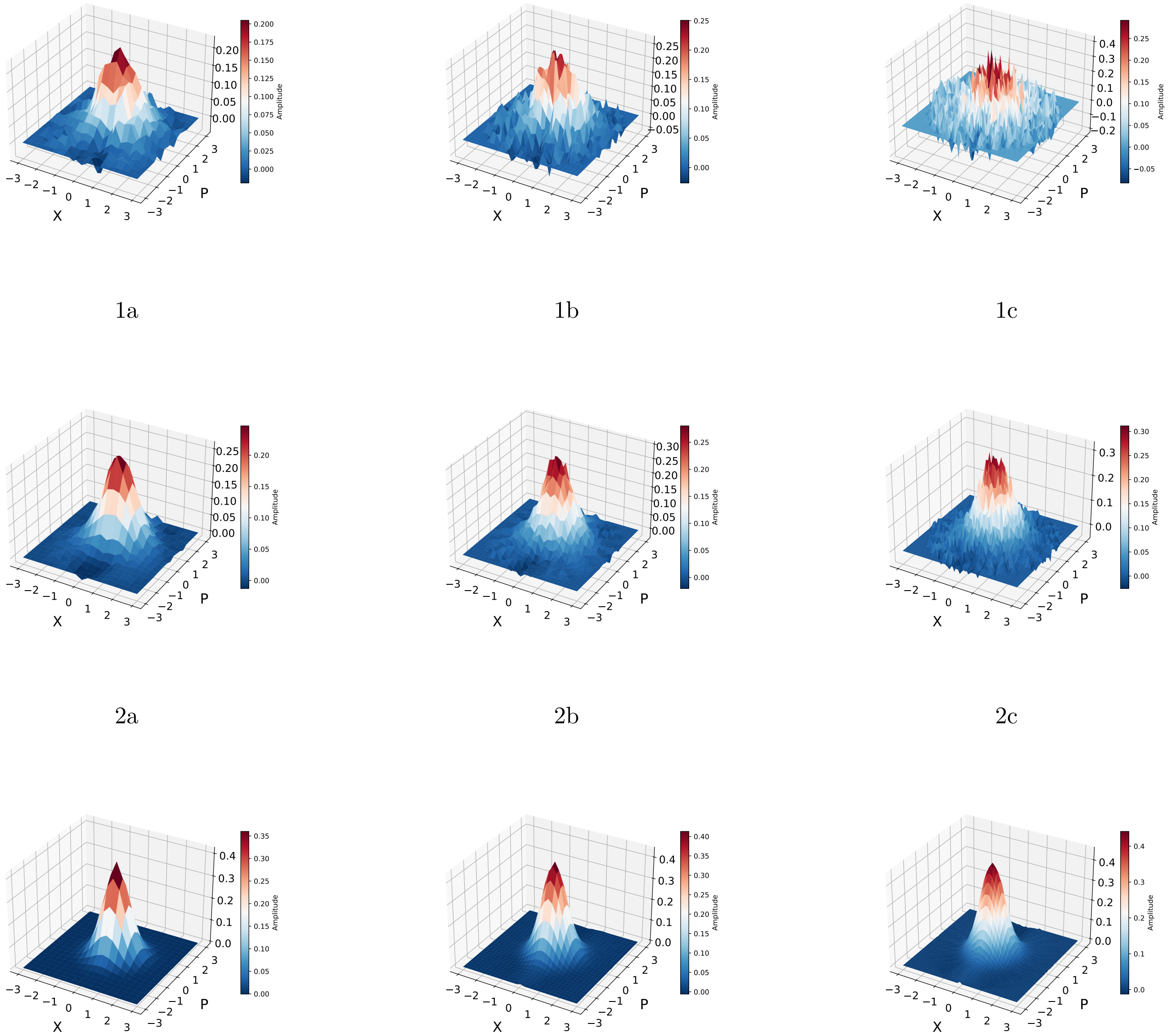

1a 1b 1c

2a 2b 2c

3a 3b 3c

Figure 4.8: The figure shows the results of the Wigner function reconstruction for the vacuum state using the Inverse Radon Transform. The reconstruction status varies by changing both the number of points and the number of histogram bins, similarly to Figure 4.7. Moreover, it is clear that when the number of points is too low or the number of bins is too high, the Wigner reconstruction is significantly compromised. The ringing artefacts observed in the reconstructions are due to numerical effects introduced by the Ram-Lak filter employed. This filter is the default choice in the `iradon` implementation; however, smoother filters, such as Hamming or Hann, can be applied to mitigate these oscillations, as demonstrated in Figure 4.6.

4.1.2 Coherent state

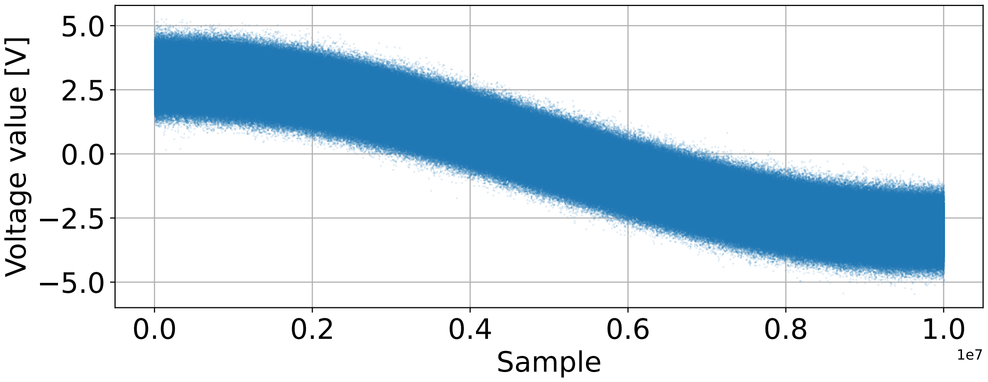

(a)

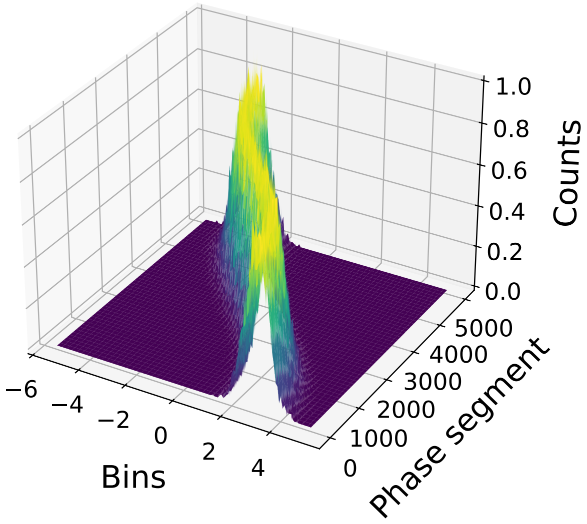

(b)

Figure 4.9: In the figure above, the generated trace (a) and the corresponding histograms (b) for the coherent state are shown. A total of 10^7 points divided in 5000 phases with 150 bins per phase were used, with coherent parameter $\alpha = 3$. As expected from theory, the standard deviation of the trace is constant and equal to the one of vacuum. The trace resembles a sinusoidal shape, with shifts depending on the complex coherent parameter α. In (b), the histograms follow the expected behaviour: they have the same width as the vacuum distributions but are displaced depending on the phase θ.

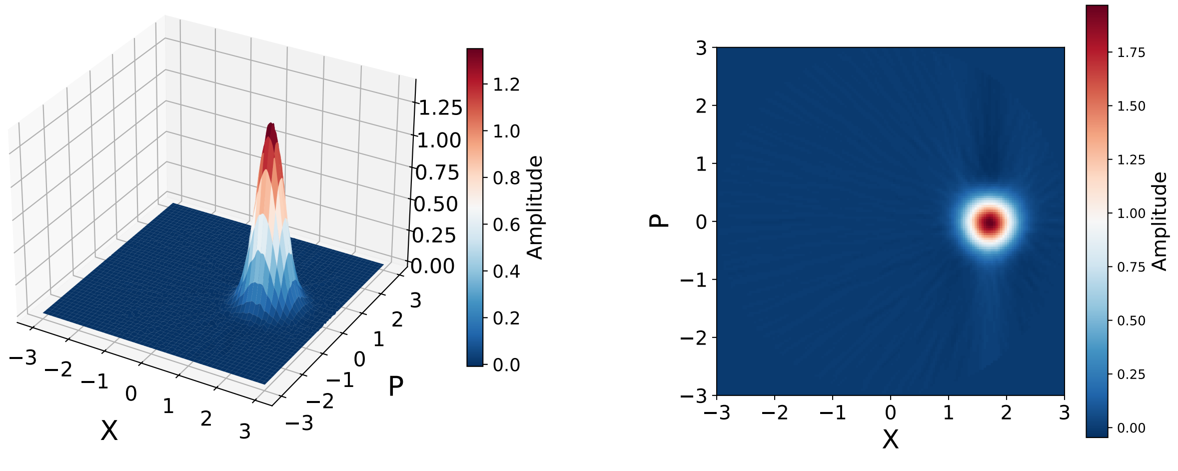

(a) (b)

Figure 4.10: In the figure above, both the two-dimensional and three-dimensional Wigner reconstructions of the state shown in Figure 4.9, obtained using a Hann filter, are presented. As theoretically expected, the Wigner function exhibits a displaced Gaussian profile, centred at $\alpha \sim 2 + 0i$. The height of the Gaussian is however not the expected value of $\frac{1}{\pi}$. This is a common issue with the IRT, since no physical constraints are imposed in the transformation. Normalization effects are then expected during experimental reconstructions.

The coherent states are defined as the eigenstates of the annihilation operator:

$$\hat{a} \left|\alpha\right\rangle = \alpha \left|\alpha\right\rangle . \tag{4.1.5}$$

and are emitted by an ideal laser. The corresponding Wigner function is expected to exhibit a non zero mean Gaussian function in the phase space (as derived in Section 2.2.2). The obtained results for the coherent Wigner reconstruction by simulated data are reported in Figure 4.10 and, as expected, shows a similar behaviour as above stated.

As before anticipated, the centre of the Wigner function has to be intended in α, in order to have a more direct relation with the displacement operator: $\left|\alpha\right\rangle = \hat{D}(\alpha) \left|0\right\rangle$. However, the recovered Wigner function has normalization issues (maxima close to 2 instead of the $\frac{1}{\pi}$ expected factor) and the coherent parameter is not in the expected position of $2 + 0i$ but, rather, in $\alpha \sim 1.9 + 0i$.

As it is possibe to see from figure 4.11, the choice of the filter can be important also for the coherent states.

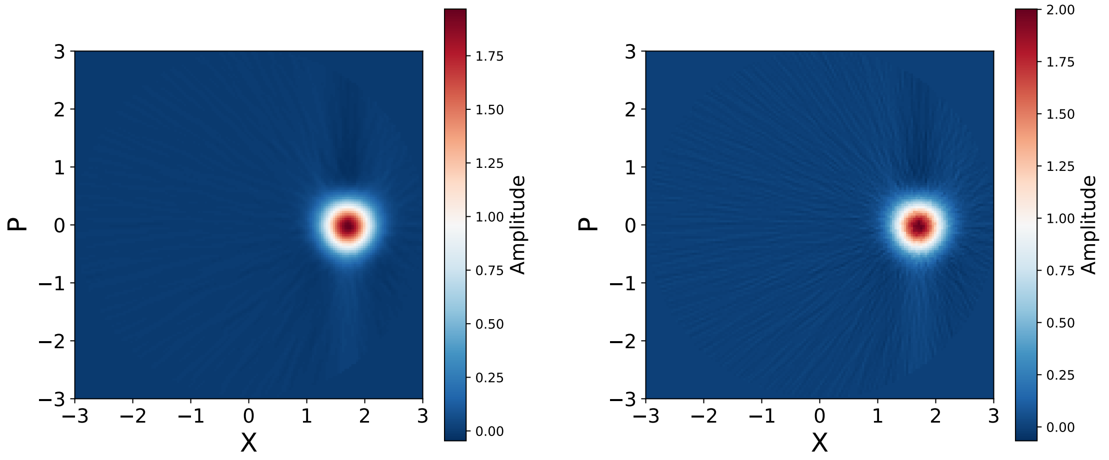

(a) (b)

Figure 4.11: For completeness, the same Wigner function shown in Figure 4.10 (a), together with an evaluation using a Ram-Lak filter (b), is reported above. As expected, the Ram-Lak estimation is noisier and exhibits more prominent ringing than the Hann filter result.

4.1.3 squeezed states

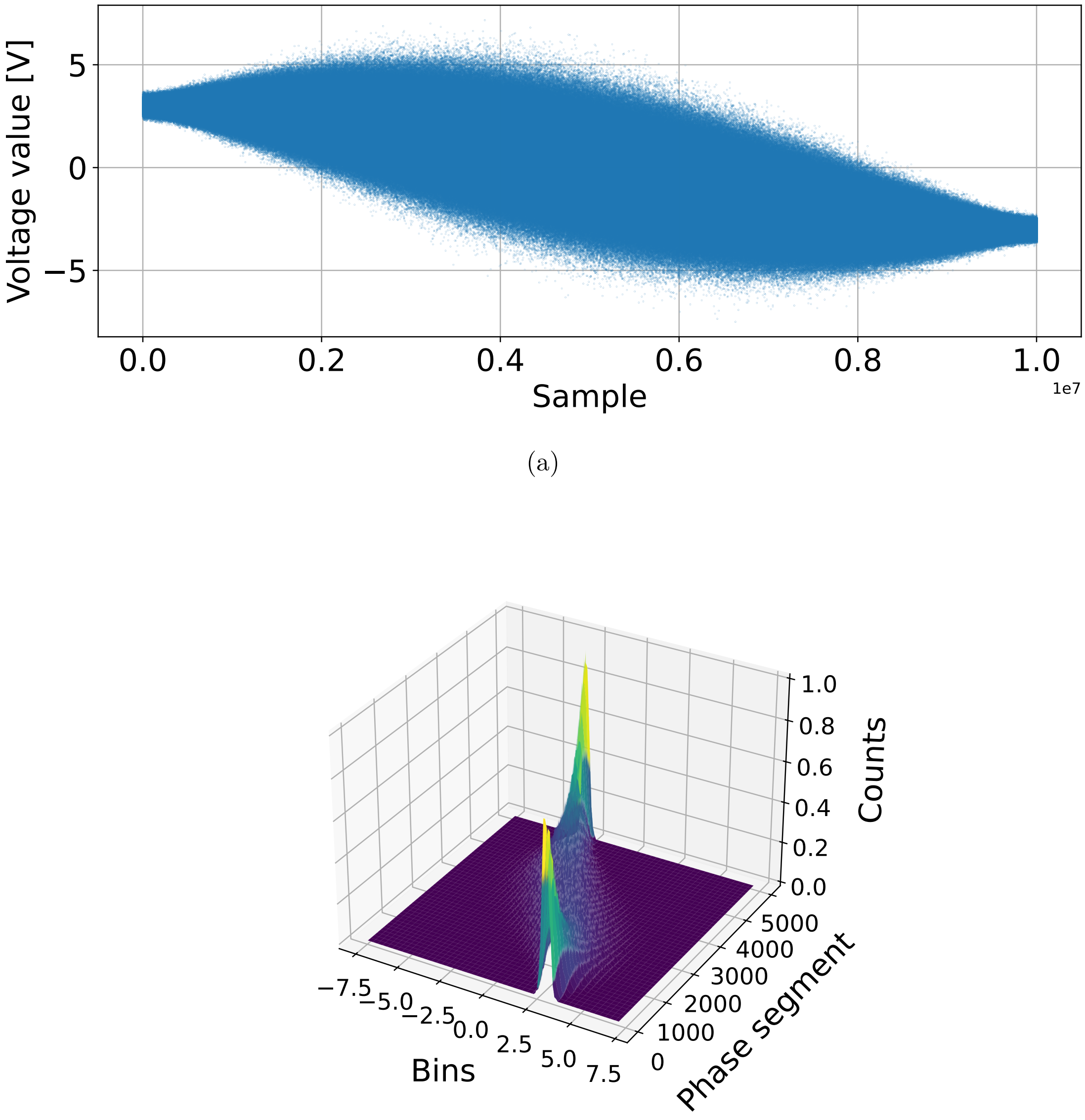

(a)

(b)

Figure 4.12: In the figure above, the generated trace (a) and the corresponding histograms (b) for the squeezed state are shown. A total of 10^7 points divided into 5000 phases with 150 bins per phase were used, with coherent parameter $\alpha = 3$, squeezing parameter $r = 1$ and rotation angle $\phi = 0.5$. The trace is, as expected, showing different variance values depending on the phase θ and it is also shifted by the rotation phase ϕ. This behaviour, as expected, is also translated into the histograms of figure (b) that clearly shows a squeezed characteristic.

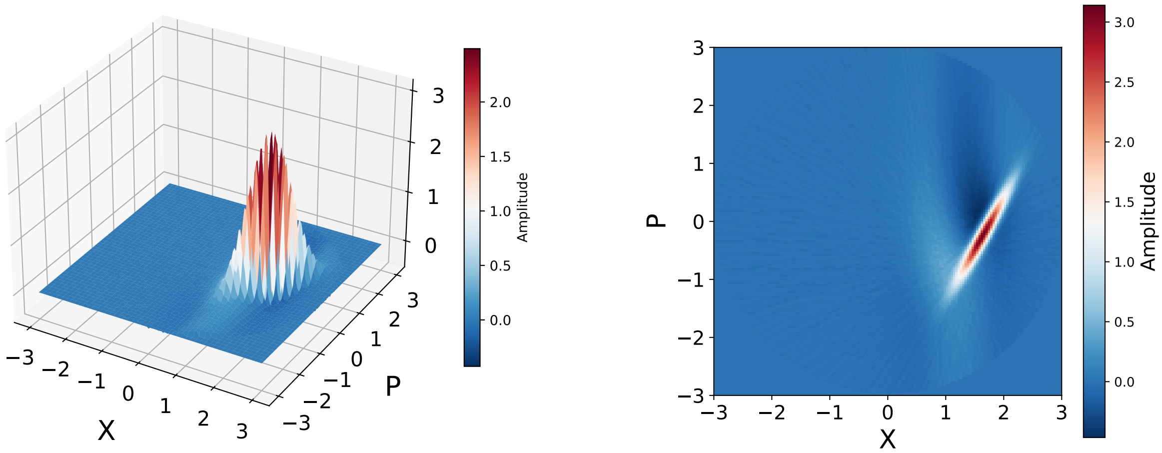

(a)

(b)

Figure 4.13: The figure above shows the three-dimensional (a) and two-dimensional (b) reconstructions of the Wigner function for the squeezed state evaluated from the data presented in Figure 4.12, with a Hann filter. The Wigner function is displaced according to the coherent parameter α, that however diverges from the expected value of $\alpha = 2+0i$, and it exhibits both the squeezed and anti-squeezed quadratures, with the expected phase shift of $\phi = 0.5$. However, the maximum of the reconstructed function is not at the expected value of 0.314. Moreover, the baseline level of the phase space is higher than expected. Nevertheless, the obtained distribution unambiguously corresponds to that of a squeezed state.

The squeezed states are states characterized by the same properties as coherent ones but they are not forced to have the same variance for all the quadratures, as explained in Section 2.2.3. Moreover, since they are minimum uncertainty states (see Appendix 6.6), once the squeezing (or antisqueezing) is known, then also the antisqueezing (or squeezing) is uniquely determined. Then the Wigner function of a squeezed state is expected to be a Gaussian function *squeezed* along one quadrature and *anti-squeezed* along the other.
The simulated trace with histograms are presented in Figure 4.12, while the Wigner reconstruction with an Hann filter is presented in Figure 4.13.
As for the coherent state both an error in the displacement (expected to be at $\alpha = 2+0i$ but found at $\alpha \sim 1.8+0i$) and regarding the height of the Wigner (found above 2 but expected at $\frac{1}{\pi}$) are present.
A clear squeezing is however recovered (with a simulated squeezing parameter r = 1) with an evident phase shift of $\phi = 0.5$. The difference between a squeezed stated with $\phi = 0$ and $\phi = 0.5$ are shown in Figure 4.14, and follows the expected behaviour.

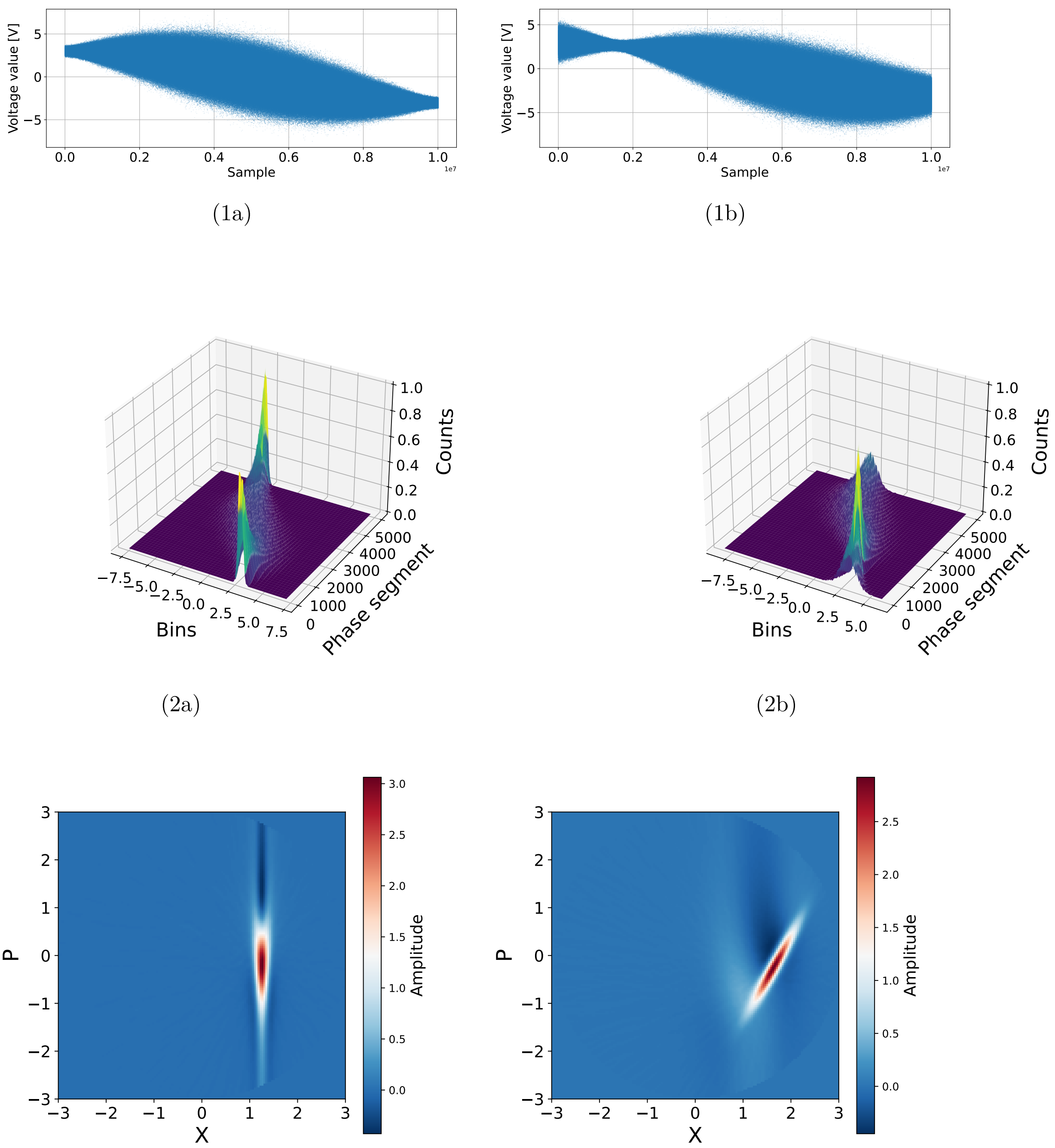

(1a) (1b)

(2a) (2b)

(3a) (3b)

Figure 4.14: In the figure above are shown the images of traces (1), histograms (2) and two-dimensional Wigner reconstruction (3) for displaced squeezed states with angle $\phi = 0$ rad (a) and $\phi = 0.5$ rad (b). The extra angle, as before stated, is simply inducing a rotation clearly shown in the histograms and in the Wigner function.

4.2 Experiment results

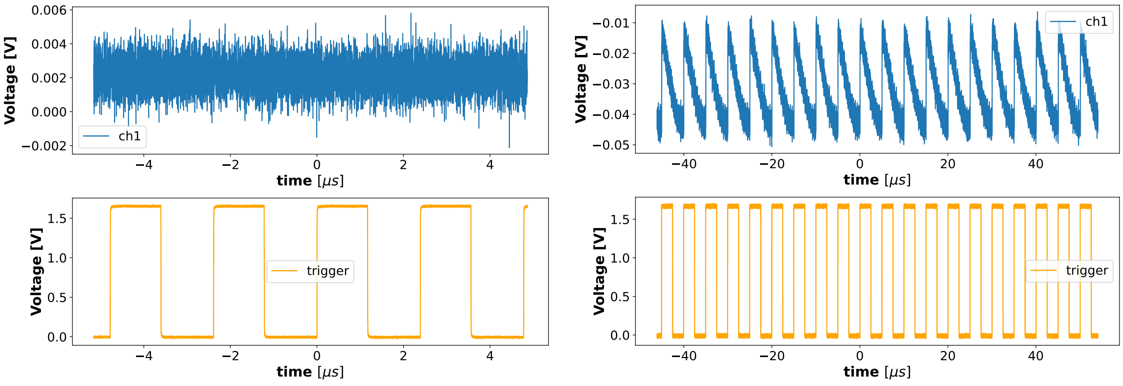

(a) (b)

Figure 4.15: In the figure above, the traces corresponding to the vacuum (a) and to the coherent self-interference of the LO (b) are presented. Both the trigger (below) and the recorded signal (above) are shown for completeness.

Now that the expected Wigner functions for the states of interest have been shown, and the code has been verified to work properly, the experimental results can be presented.

In retrospect, we know that the expected squeezed state (quantum well driven by a quiet pump) was not observed due to experimental issues. However, some calibration states, namely vacuum and coherent, were measured.

In order to scan in all the different phase projections, the setup presented in Figure 3.1 was used, with a triangular modulation between 0 and π using 100% symmetry.

The Agilent AWG was then programmed in a way to repeat the input modulation periodically, and data segmentation was performed to isolate the useful data within a single period.

To help in this process, the trigger channel was connected to another port of the oscilloscope to register abrupt jumps each time the signal repeated. The achieved traces are visible in Figure 4.15. Some cuts of the signal have to be done in order to mitigate for non-idealities (delays, jumps etc.).

The vacuum trace was then used for the normalization, following the procedure explained in 4. The standard achieved standard deviation for the on_trace (Total Variance), off_trace (Electrical Variance) and lo_trace (Shot Variance) are summarized in the table below:

Total Variance	**Electrical Variance**	**Shot Variance**
6×10^{-6}	2×10^{-6}	4×10^{-6}

4.2.1 Vacuum state

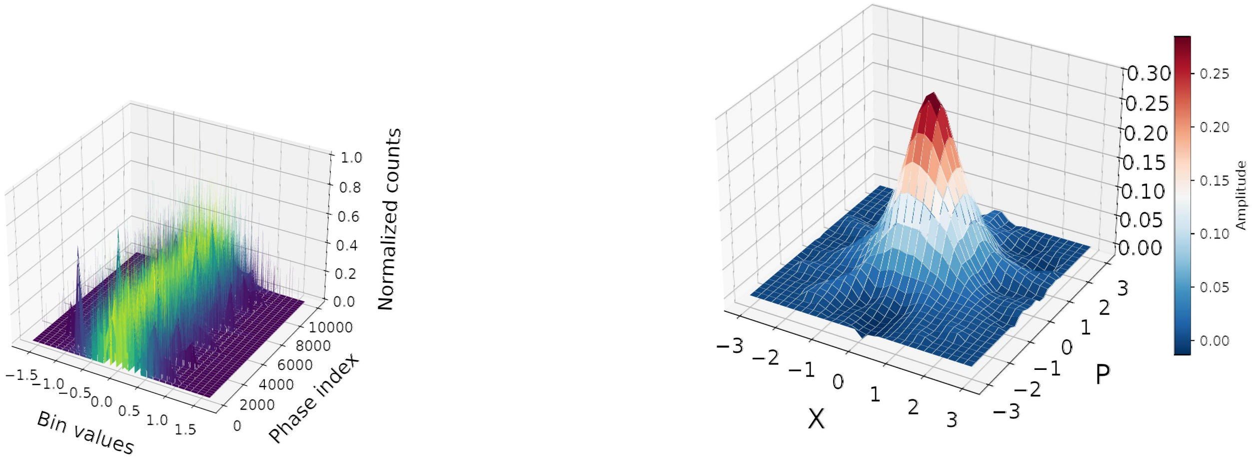

(a) (b)

Figure 4.16: In the figure above the reconstructed Wigner function for the vacuum state is shown, derived from the data presented in Figure 4.15. The trace was divided with a total of 10^5 phase segments, divided into 30 bins, was used, with a Hann filter applied to smooth high-frequency non-idealities. The histograms (a) show peaks away from the centre value, likely due to residual electronic noise, while the reconstructed Wigner function (b) exhibits a peak at 0.296 (slightly lower than the expected 0.314) and a variance of two SNU (higher than expected). Nevertheless, the reconstruction clearly indicates a vacuum state, with a peaked Gaussian at 0 and fixed standard deviation.

The vacuum reconstruction of the Wigner distribution starting from the trace is shown in Figure 4.15 is presented in Figure 4.16. As expected, the trace is phase independent and shows the same variance for any phase. On the other hand, the Wigner reconstruction clearly manifest a Gaussian peak at 0 and a fixed standard deviation of 2 SNU, slightly above the expected 1 SNU. The dataset was then enlarged by summing up multiple trigger periods in order to accumulate more information, allowing us to achieve a trace of 499993 points, due to the high sampling rate of the oscilloscope (25GSa/s). Still, some errors can be found both in the histograms and in the Wigner function as noted, making the reconstruction not as clear as the one shown in the ideal simulations.

4.2.2 Coherent state

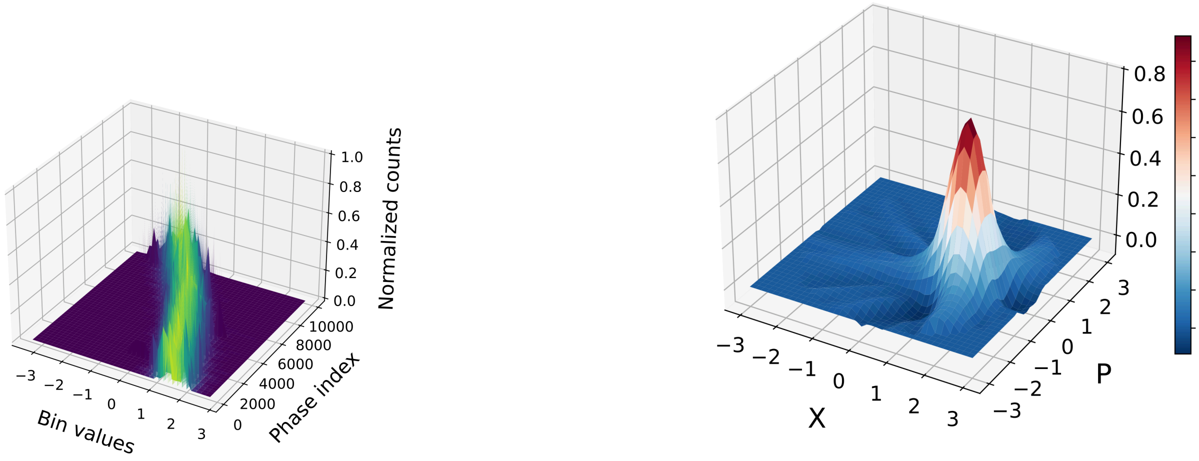

(a) (b)

Figure 4.17: In the figure above, the reconstructed Wigner function for the coherent state is shown, derived from the data presented in Figure 4.15. The trace was divided with a total of 10^5 phase segments, divided into 40 bins, was used, with a Hann filter to achieve a better reconstruction. The histograms (a) show peaks that follow the expected sinusoidal behaviour, proportional to the mean photon number $|\alpha|^2$. In (b), the Wigner function exhibits a peak at 0.791 (slightly higher than the expected 0.314) and a variance of 1.3 SNU (higher than expected). Other issues are then related to the ripples at the basis of the Gaussian and some unexpected negativities. Nevertheless, the reconstruction clearly indicates a coherent state, with a peaked Gaussian at $\alpha_{\mathbb{R}} = 1$, $\alpha_{\mathbb{I}} = 0$.

The coherent reconstruction obtained by the self-interference of LO is shown in Figure 4.15.
Some unexpected negativities are present, together with ripples and a peak of the Wigner function higher than 0.314, probably due to residual electronic noise. In order to further lower the coherent parameter, the fibre was also slightly unplugged in order to have a higher attenuation.

4.2.3 Quiet pump state

This high phase noise of the signal (see Figure 4.18) invalidates the Inverse Radon Transform approach for the quantum well laser driven by quiet pump source introduced in Chapter 1. Indeed, the algorithm relies on the assumption that the phase can be tracked in a known way.

Since the quadrature distributions are determined by the argument of the interference cosine (and thus by the phase $\phi(t)$), this induces the distributions to pick at random values within the interval $[0,\, 2\pi]$. Moreover, due to the high frequency at which this effect occurs, our low bandwidth detectors (bandwidth ~ 350 MHz) were not able to track the phase diffusion. A trial with faster photodiodes (u2tBPDV2150R) was done, although without success due to the high electronic noise.

The obtained Wigner reconstruction is shown in Figure 4.19.

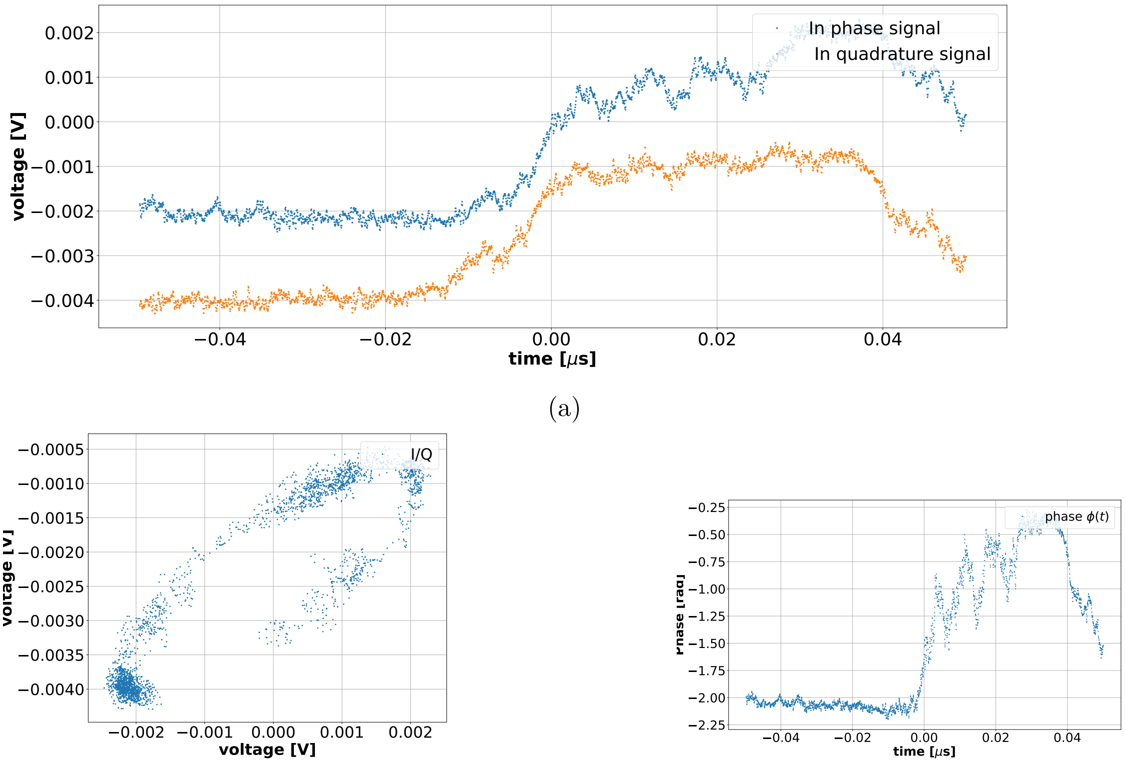

(a)

(b)

(c)

Figure 4.18: In the figure above, the noise characteristics of the quantum well laser are presented. The results were obtained from a self-beating experiment performed on the quantum well laser driven by a quiet pump and measured with u2tBPDV2150R photodetectors to capture all phase drifts. In (a), the in phase (I) and Quadrature (Q) signals are shown, presenting a very high phase noise despite the nominally negligible frequency difference. For completeness, panel (b) shows the I vs. Q plot together with the corresponding phase distribution. As expected, the phase is almost completely random. This random phase behaviour prevents a successful inverse Radon transform (IRT) reconstruction, since the phase distribution does not follow any known order. Some discontinuities are visible in the plots because only a subset of points was displayed for computational efficiency.

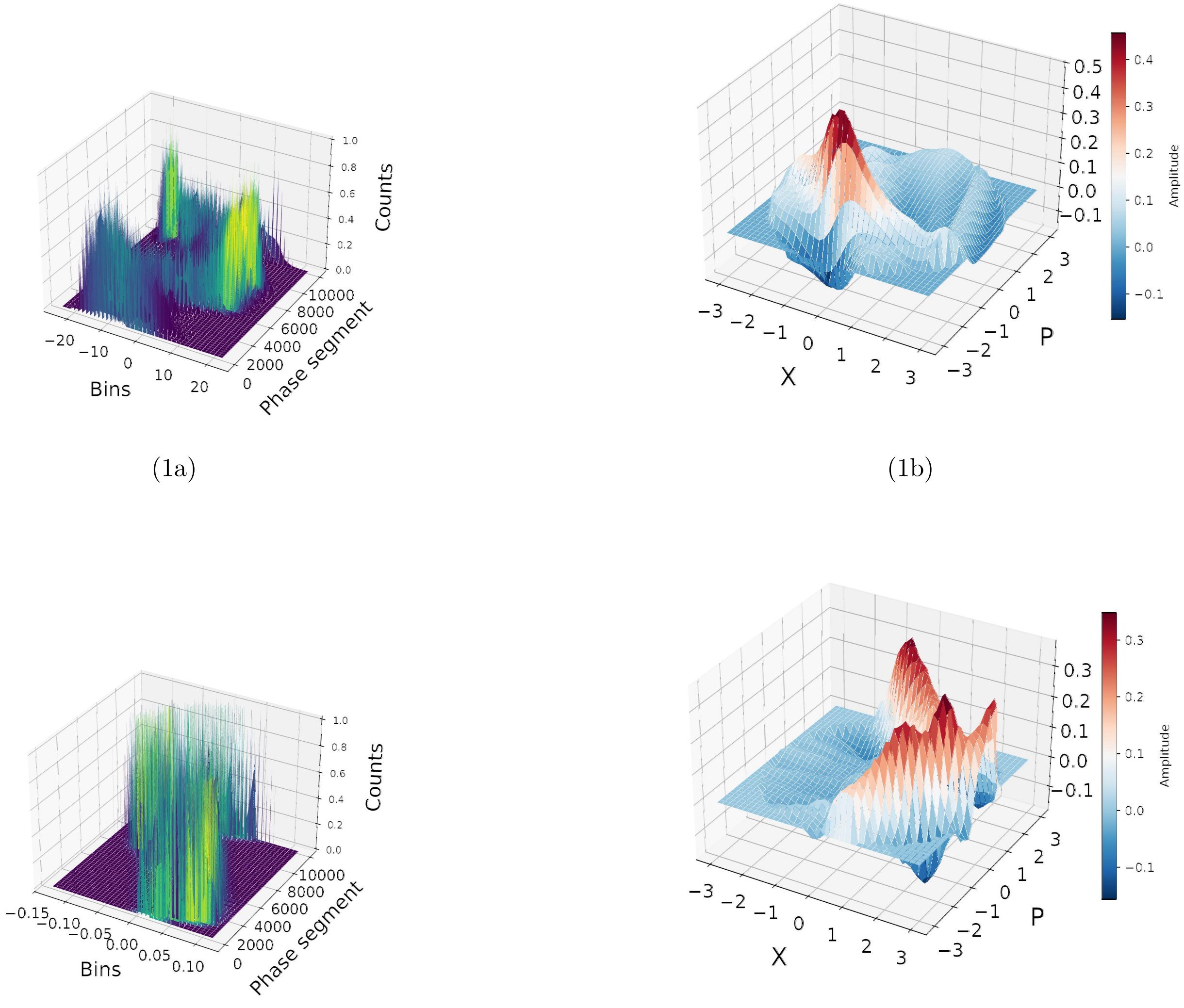

(1a)

(1b)

(2a)

(2b)

Figure 4.19: In the figure above, the results of the inverse Radon analysis for the data presented in Figure 4.18 are shown. The analysis refers to the quantum well laser driven by a quiet pump, beating against itself (1), and to the complete interference with the Teraxion laser used as the local oscillator (2). In both cases, the phase drifts of the quantum well laser prevent the reconstruction of the Wigner function. The situation is even worse for the complete interference, since the frequency difference between the two lasers must be taken into account.

Chapter 5

The Maximum Likelihood Estimation

Since the Inverse Radon Transform approach proved ineffective for the quiet pump driven quantum well laser, alternative reconstruction methods were explored. Among these, the Maximum Likelihood Estimation (MLE) appeared promising, due to the small number of needed quadrature projections (i.e. spanned phases). This will allow us to obtain better statistics to recover the measured state, since more points for each phase can be acquired assuming a fixed modulation speed.

This idea was based on the fact that the Maximum Likelihood Estimation is intrinsically more resilient to noise than the Inverse Radon Transform [41]. Indeed, since a lower number of phases is required, a higher acquisition time per quadrature can be assigned. This improves the statistical accuracy. However, the number of required phases, is expected to be dependent on the dimension of the rebuilt density operator $\hat{\rho}$ [42].

Imagine defining a function, referred to as the *likelihood function*, constructed from the outcomes of measurements performed on a system. The likelihood function, therefore, encodes all the relevant information about the system and represents an estimator of the probability to obtain those measurements, allowing one to retrieve the state or the parameters that most likely generate the observed data.

The estimation process is then carried out by maximizing such function.

The concept of likelihood, and in general of likelihood estimators, was first introduced by Fisher under the assumption of independent and identically distributed (i.i.d.) random variables (for a given quadrature probability outcome) [43]. It relies on the Wald theorem [44] and on the laws of large numbers [45], as will be discussed later.

In particular, it will be shown that the MLE can be interpreted as an iterative convergence algorithm for the estimator (the likelihood), whose convergence rate depends on the amount of information that the dataset provides; i.e. on the number and on the cleanliness of available data points [43].

However, other studies have proven that even in the presence of dependencies among the data, the MLE can still converge [46]. Nevertheless the hypothesis of independency of the data is required here, in order to simplify the model, since there is no reason to assume correlation between the measurements. However, it is important to emphasize that the identically distributed assumption applies to a single phase, so to a single quadrature probability distribution, a condition that is indeed satisfied by the physics of quadrature measurements.

To formalize this, consider a set of measurements,

$$y = (y_1, \cdots, y_n), \tag{5.0.1}$$

where each y_i represents an observation.
The Likelihood function is related to the probability of obtaining the observed data given a specific statistical model, thereby allowing the estimation of the parameters or the state of the system that most likely produced the data.
Since every point is generated by a generic distribution, it can be related to the set of parameters that define a distribution, called α. For instance, if the distribution y_i is Gaussian, then $\alpha = (\mu, \sigma^2)$, where μ identifies the mean value and σ the standard deviation of such distribution.
Therefore, the Likelihood function $L_n(\alpha)$ measures *how much* the measured data y_i is compatible with the distribution α_i. In other words, by maximizing the Likelihood function L, it is possible to estimate the distribution α for any given point.

Following the rules of the probability theory, the probability of observing all the achieved n outcomes is the product of the single events:

$$P(y_i, y_2, \cdots, y_n|\alpha) = \prod_{i=1}^{n} f(yi, \alpha) \tag{5.0.2}$$

that is indeed the searched Likelihood function $L(\alpha)$, from now on also called $L(\theta)$ for make evident that the points are grouped by constant phase (thus same distribution).
Since in this contest the Likelihood function is managing to reconstruct the quantum state (so the density matrix $\hat{\rho}$), another notation that will be used is $L(\hat{\rho})$.
Due to numerical reasons, instead of using the product as in 5.0.2, its logarithm is introduced:

$$\ln\left(\prod_{i=1}^{n} f(yi, \alpha)\right) = \ln\left(L(\theta)\right) = \sum_{i=1}^{n} \ln(f(yi, \alpha)) = \mathcal{L}(\theta) \tag{5.0.3}$$

and it is usually referred to as *log-likelihood* or *Log-Likelihood* function.
This likelihood can be proven to have the same properties as the previous one defined. Indeed, suppose Θ is a set of values and f is a function such that $f : \Theta \to \mathbb{R}$ (property fulfilled by the Likelihood function). Then given a value $\alpha^* \in \Theta$ that maximizes the f function ($f(\alpha^*) \geq (\alpha) \quad \forall \alpha \in \Theta$), then also $\ln f(\alpha^*) \geq \ln f(\alpha) \quad \forall \alpha \in \Theta$; conversely if α^* maximizes $\ln \{(\alpha^*)$, then $f(\alpha^*) \geq f(\alpha)$. This statement is crucial since it implies that the logarithm of the Likelihood function is maximized by the same value of the Likelihood itself, thus the target value (or values) is (are) the same.
This property is not typical of the logarithm, but it can be extended to a monotonically

increasing function g (i.e. $\forall a, b \in \Theta$ s.t. $a > b \quad g(a) > g(b)$), with equality holding if the function is strictly increasing.

In order to find the maximum of a generic function f (as the log-likelihood), the gradient rule can be applied:

$$\nabla_\alpha f(\vec{\alpha}) = 0 \qquad \Longrightarrow \qquad \frac{\partial f(\vec{\alpha})}{\partial \alpha_i} = 0 \tag{5.0.4}$$

However, if the function is not differentiable (usual situation in real experiments), a convergence algorithm must be employed. Possible strategies could be smoothing of the function, using sub-differential conditions or randomly exploring the space in order to find the solution. All these methods are, however, highly expensive from the computational power perspective, a reason why the Maximum Likelihood Estimation requires high computational capabilities.

Moreover, for some states the density functions f could be complex and difficult to model also in simulated data, thus leading to highly non-linear equations. This problem can be avoided by looking at simple distributions as Gaussians or exponential ones, as the states studied in this work. However, no assumption on the state type was made in order to keep the model to be general for any state as proven in Figure 5.5.

5.1 The algorithm and state simulations

As previously stated, the homodyne detection scheme, shown in Figure 3.1 (reported in Figure 5.16 for convenience), is able to retrieve the probability distributions of the quadrature operator $\hat{X}_\theta$.

The outcomes of the homodyne measurement correspond to the eigenvalues of such operator.

Given that each event has a probability pr_j and a frequency f_j to occur, then the Likelihood function can be written as:

$$\mathcal{L}(\hat{\rho}) = \prod_j \mathrm{pr}_j^{f_j}. \tag{5.1.1}$$

However, the probability of a given outcome is given by the measurement theorem:

$$\mathrm{pr}_j = \langle y_j | \, \hat{\rho} \, | y_j \rangle = \mathrm{Tr}[\hat{\Pi}_j \hat{\rho}], \tag{5.1.2}$$

where $\hat{\rho}$ is a density matrix operator, $\{|y_j\rangle\}$ are the von Neumann basis vectors and $\hat{\Pi}_j = |y_j\rangle \langle y_j|$ is the projection operator.

One can therefore introduce an operator ruling the convergence evolution of $\hat{\rho}$ as [41]:

$$\hat{R}(\hat{\rho}) = \sum_j \frac{f_j}{\mathrm{pr}_j} \hat{\Pi}_j. \tag{5.1.3}$$

It is possible to see that this operator is able to find the density matrix $\hat{\rho}$ generating the input data, therefore maximizing the log-likelihood function. Indeed:

$$\begin{aligned}\frac{\partial \mathcal{L}}{\partial \hat{\rho}} &= \sum_j f_j \frac{\partial \ln(\mathrm{pr}_j)}{\partial \hat{\rho}} \\ &= \sum_j \frac{f_j}{\mathrm{pr}_j}\frac{\partial \mathrm{pr}_j}{\partial \hat{\rho}} = 0,\end{aligned} \tag{5.1.4}$$

where the equality to zero was set in order to find the stationary points. Finally:

$$\begin{aligned}\frac{\partial \mathcal{L}}{\partial \hat{\rho}} &= \sum_j \frac{f_j}{\mathrm{pr}_j}\frac{\partial \mathrm{pr}_j}{\partial \hat{\rho}} \\ &= \sum_j \frac{f_j}{\mathrm{pr}_j}\hat{\Pi}_j = \hat{R}(\hat{\rho}),\end{aligned} \tag{5.1.5}$$

where the relation $\mathrm{Tr}[AB] = \sum_{ij} A_{ij}B_{ji}$ was used in order to compute $\frac{\partial \mathrm{Tr}[AB]}{\partial B} = \sum_{ij} A_{ij}$. If now $\hat{\rho}^*$ is the density that is maximizing the log-likelihood ($\hat{\rho}^* = \arg\max(\mathcal{L}(\hat{\rho}))$), then the j^{th} result pr_j will appear with a frequency f_j.
In particular, these two values are linked by a constant:

$$f_j = c \times \mathrm{pr}_j(\hat{\rho}_0), \tag{5.1.6}$$

since the frequency of occurrences is given by the number of times each outcome is observed.

Namely, the density $\hat{\rho}^*$ is able to generate the exact data that were measured, and:

$$\begin{aligned}\hat{R}(\hat{\rho}^*) &= \sum_j \frac{f_j}{\mathrm{pr}_j(\hat{\rho}^*)}\hat{\Pi}_j \\ &= \sum_j \frac{c \times \mathrm{pr}_j(\hat{\rho}^*)}{\mathrm{pr}_j(\hat{\rho}^*)}\hat{\Pi}_j \\ &= c\sum_j \Pi_j.\end{aligned} \tag{5.1.7}$$

However, the operator $\hat{\Pi}_j$ is a set of projection operators (POVMs), thus the sum has to be the identity:

$$\sum_j \hat{\Pi}_j = \mathbb{I}, \tag{5.1.8}$$

then the operator $\hat{R}(\hat{\rho}^*)$ is a constant $\implies \hat{R}(\hat{\rho}^*) \propto \mathbb{I}$.
But since any operator commute with the Identity operator $\mathbb{I}$, then

$$\hat{R}(\hat{\rho}^*)\hat{\rho}^* = \hat{\rho}^*\hat{R}(\hat{\rho}^*) \propto \hat{\rho}^*, \tag{5.1.9}$$

and the density matrix $\hat{\rho}$ can be updated by the rule [41]:

$$\hat{\rho}^{k+1} = \mathcal{N}\left(\hat{R}(\hat{\rho}^k)\hat{\rho}^k\hat{R}(\hat{\rho}^k)\right) \tag{5.1.10}$$

where $\mathcal{N}$ is a normalization coefficient defined as:

$$\mathcal{N} = \frac{1}{\mathrm{Tr}\left[\left(\hat{R}(\hat{\rho}^k)\hat{\rho}^k\hat{R}(\hat{\rho}^k)\right)\right]} \tag{5.1.11}$$

Then by iterating multiple times one is able to obtain the final convergence density matrix $\hat{\rho}^*$.
Usually a small number of iterations is needed for convergence, as later shown. It is important to notice that the projection operator $\hat{\Pi}_j$ has to be written in the quadrature base.

As a remark from the theory, the quadrature operator can be equivalently defined as:

$$\hat{X}_\theta = \hat{X}\cos\theta + \hat{P}\sin\theta \tag{5.1.12}$$

$$\hat{X}_\theta = \frac{1}{\sqrt{2}}\left[\hat{a}e^{i\theta} + \hat{a}^\dagger e^{-i\theta}\right] \tag{5.1.13}$$

where the phase θ is the relative phase where the quadrature is measured. One can then define the θ-dependent quadrature eigenstate as:

$$|\theta, x\rangle = e^{i\hat{a}\hat{a}^\dagger\theta}|x\rangle \tag{5.1.14}$$

where the rotation operator $\hat{U}(\theta) = e^{i\hat{a}\hat{a}^\dagger\theta}$ was defined [3].

Moreover, since the light is composed of discrete particles (photons), the state must be described by a space that accounts for all those particles. This space, as previously described, is the Fock space.
Therefore the projection operator $\hat{\Pi}_\theta = |\theta, x\rangle\langle\theta, x|$, can be written as:

$$\langle m|\hat{\Pi}_\theta|n\rangle = \langle m|\left(|\theta, x\rangle\langle\theta, x|\right)|m\rangle, \qquad |m\rangle, |n\rangle \in \text{Fock vectors}, \tag{5.1.15}$$

where ach Fock state $|n\rangle$ is an eigenstate of the number operator $\hat{n} = \hat{a}^\dagger\hat{a}$. Moreover, it is well known that any operator $\hat{U}$ that can be expressed as a function f of an operator $\hat{n}$ ($\hat{U} = f(\hat{n})$) preserves the eigenvalues of such operator under the same transformation:

$$f(\hat{n})|n\rangle = f(n)|n\rangle. \tag{5.1.16}$$

Consequently, the rotation operator $\hat{U}(\theta) = e^{i\hat{n}\theta}$ acts on Fock states by applying a phase factor:

$$\langle n|\theta, x\rangle = \langle n|e^{i\hat{n}\theta}|x\rangle = e^{in\theta}\langle n|x\rangle, \tag{5.1.17}$$

hence, the scalar product $\langle n|\theta, x\rangle$ reads:

$$\langle n|\theta, x\rangle = e^{in\theta}\left(\frac{2}{\pi}\right)^{1/4}\frac{H_n(\sqrt{2}x)}{\sqrt{2^n n!}}e^{-x^2}, \tag{5.1.18}$$

where H_n are the Hermite polynomials and $\hbar, m\omega$ were set to one [41].

So the Maximum Likelihood implementation will follow the sequent organization:

- **Split the data per constant phase**; this will allow us to retrieve the statistic of points for every phase;
- **Update the density matrix for a certain number of iterations**; this can be implemented with the previously shown evolution formula 5.1.10;
- **Recover the Wigner function**: since the density has a one to one correspondence with the Wigner function.

However, the MLE estimation can be proven to converge strictly to a single value only under ideal conditions: when an infinite number of points (i.e., infinite information) and an infinite Fock space dimension are used. Since those two requirements can not be satisfied in experimental conditions, the next sections will analyse the limitations induced by such restrictions.

Moreover, for finite datasets, it is reasonable to expect an oscillatory behaviour at convergence [47], as shown in Figure 5.9 and formally derived in Appendix 6.12.
In particular, the amplitude of these oscillations depends on the number of points in the dataset, i.e., on the available amount of information. The larger the number of points, the better the statistics of the data, leading to a faster and more stable convergence of the MLE.

The rest of this section is organized as follows. First, we analyse ideal simulations, as previously done using the Inverse Radon Transform. Then, we discuss the limitations of the algorithm that justify the choice of the simulation parameters using a simulated coherent state with coherent parameter $\alpha = 5 + 0j$.

5.1.1 Numerical simulations

Since this work is focused on the recovery of squeezing (Figures 5.3 and 5.4), and on the calibration of coherent (Figure 5.2) and vacuum (Figure 5.1) states, only those Wigner functions will be exposed in this subsection. Moreover, since the expected distributions were already motivated 4.1, only the results simulated with the MLE algorithm are reported here.
However, similarly to the IRT approach, the MLE algorithm is able to recover any classical and quantum Wigner function [41]. To prove this well known assumption, simulation results for a single photon, as well as even and odd cat states, are presented in Figure 5.5.
The data generation made use of the `numpy` python library, whereas the MLE execution exploited the `scypi` and `QuTiP` packages.

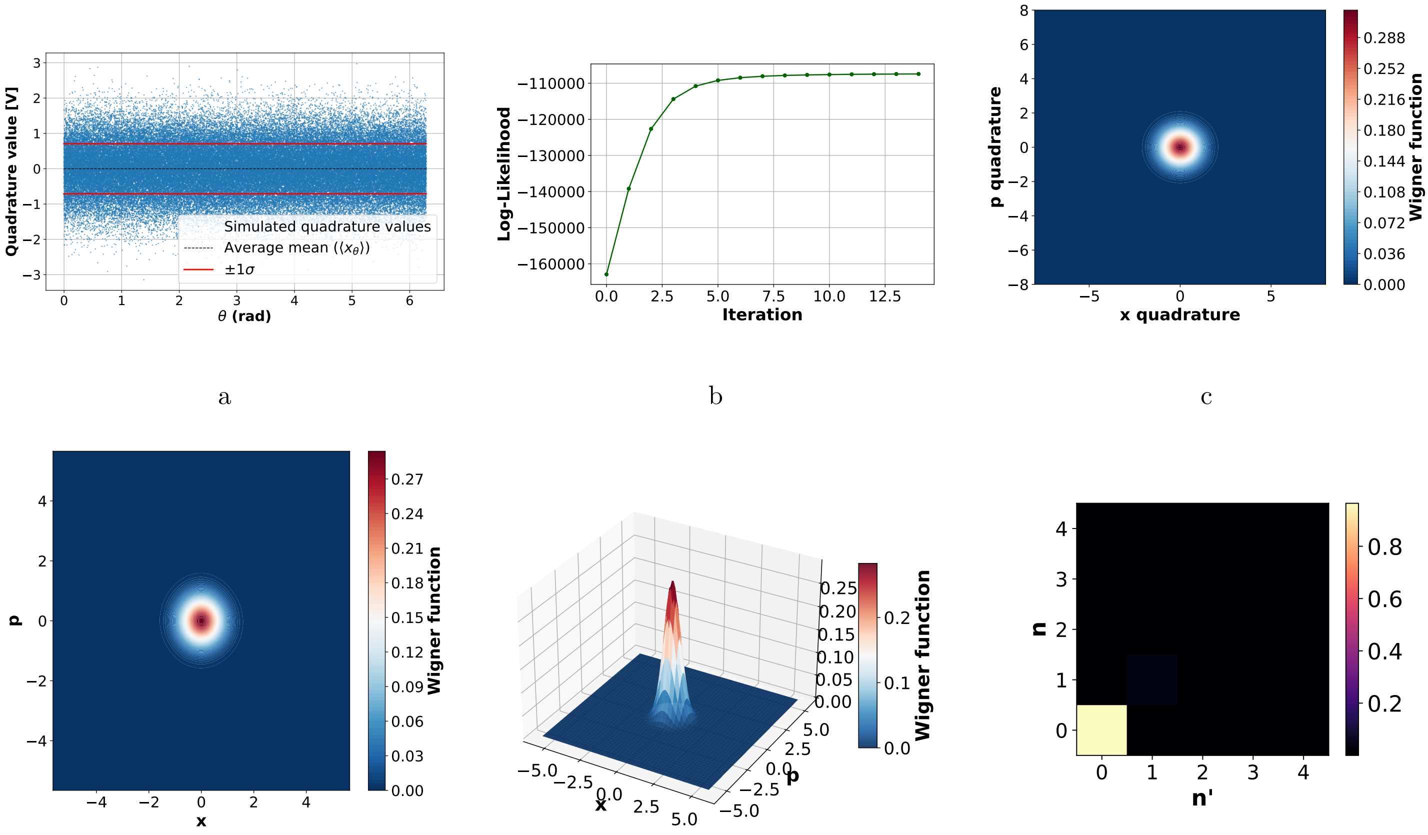

a

b

c

d

e

f

Figure 5.1: In the figure above, the vacuum state simulation is illustrated with a total of 10^5 points and 20 uniformly distributed phases. The simulated trace (a) has a fixed variance, and the expected Wigner function (c) resembles the theoretical expectation. The achieved two-dimensional (d) and three-dimensional (e) reconstructions exhibit the same behaviour, in agreement with Figure 4.5. The convergence of the log-likelihood function (b) is monotonically increasing, as stated previously, and the reconstructed density matrix (f) has only one non-zero element in the Fock basis, as expected.

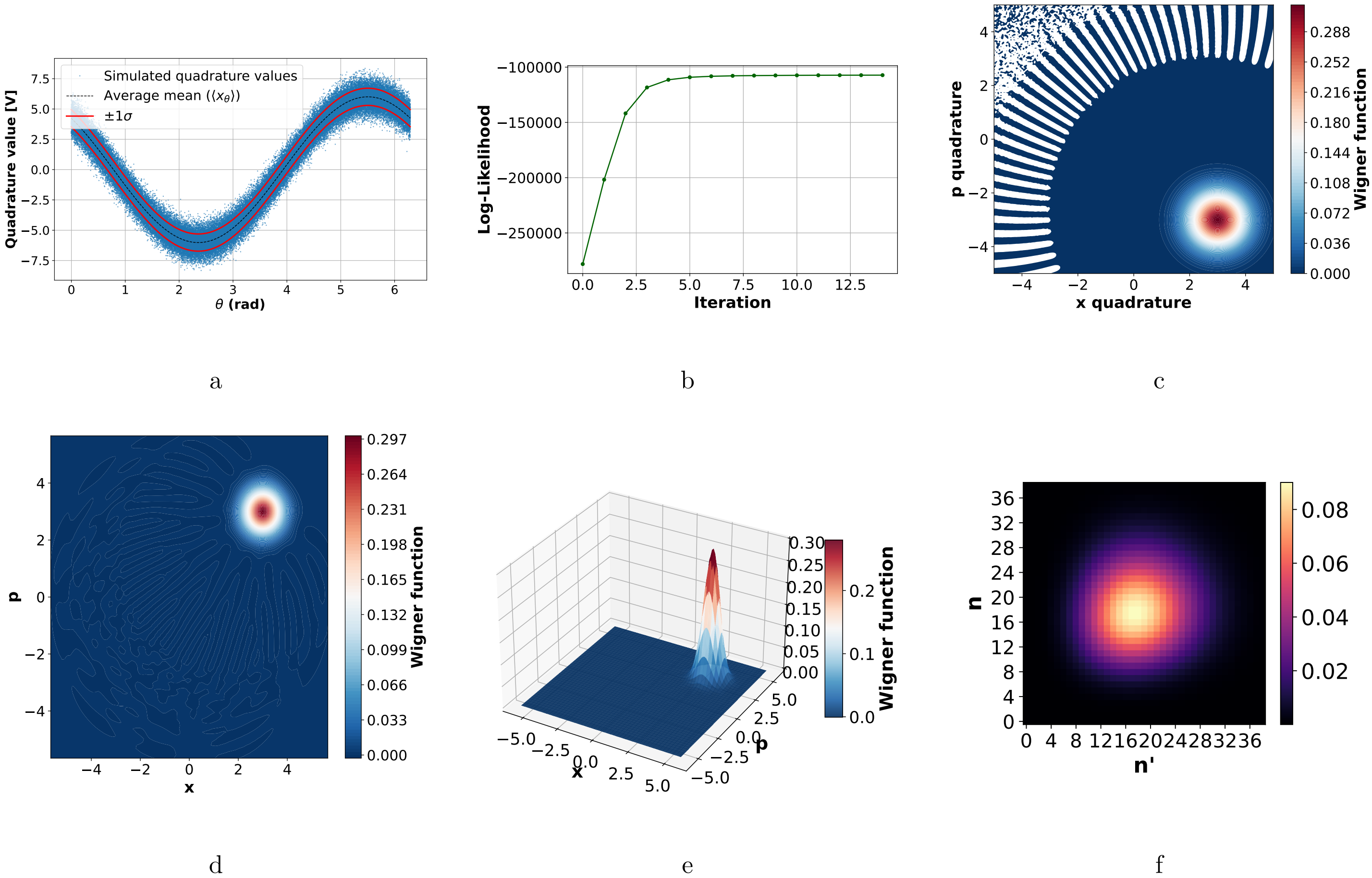

a

b

c

d

e

f

Figure 5.2: In the figure above, the coherent state simulation is shown for a total of 10^5 points with 20 uniformly distributed phases and coherent parameter $\alpha = 4.3 + 4.3j$. The simulated trace (a) has a fixed variance and a cosinusoidal phase dependence, while the expected Wigner function (c) matches the theoretical expectation. The achieved two-dimensional (d) and three-dimensional (e) reconstructions are in agreement with Figure 4.10. The Likelihood function convergence (b) shows a plateau and the reconstructed density matrix (f) exhibits a Gaussian distribution centred at the mean photon number $|\alpha|^2 = 18$, as expected.

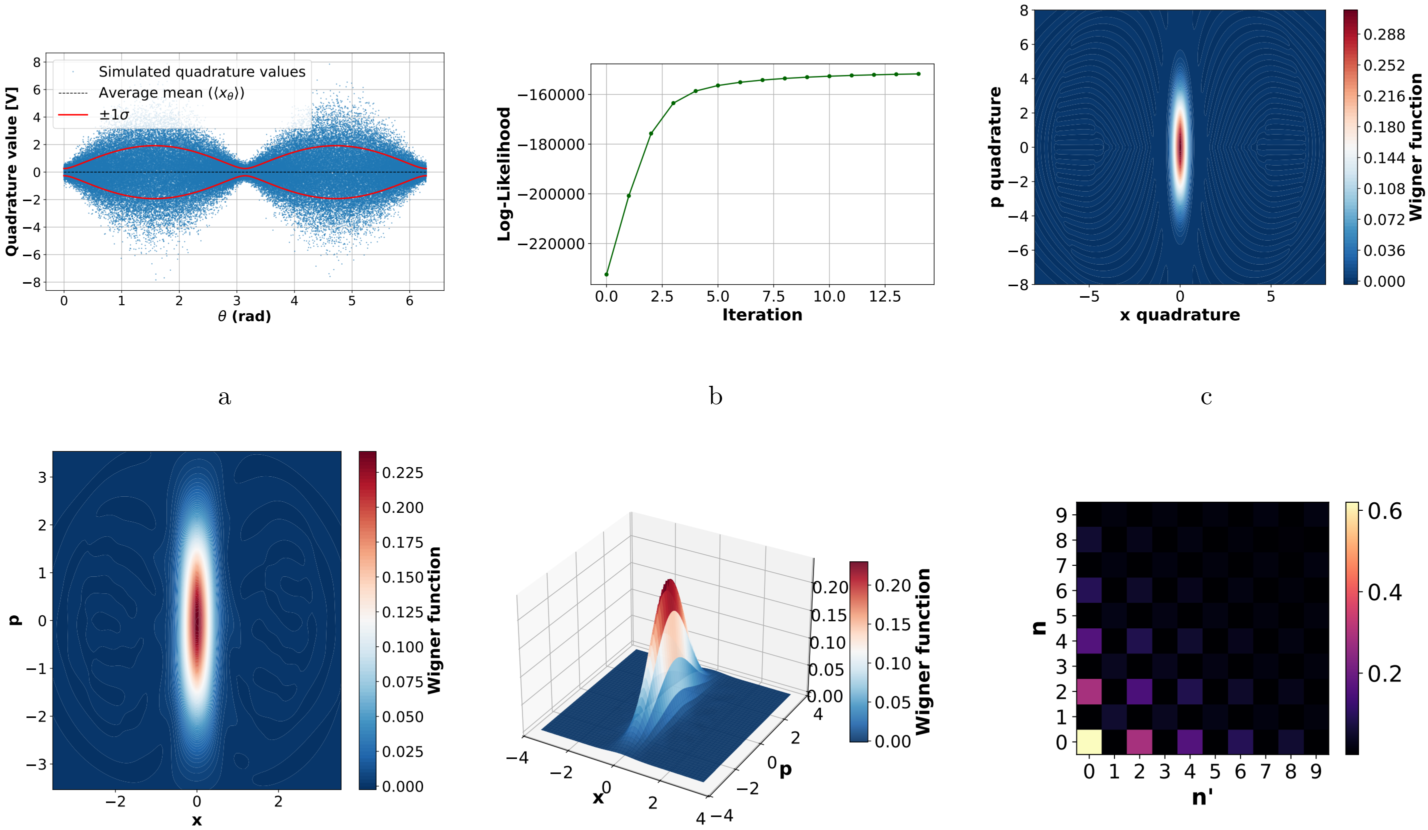

a b c

d e f

Figure 5.3: In the figure above, the squeezed vacuum state simulation is shown with a total of 10^5 points, 20 uniformly distributed phases, squeezing parameter $r = 1$, and Fock dimension $N_{fock} = 20$. The simulated trace (a) has a variable variance and a cosinusoidal phase dependence, while the expected Wigner function (c) is in line with the theoretical expectation, showing a high squeezing on the $\hat{X}$ quadrature. The achieved two-dimensional (d) and three-dimensional (e) reconstructions again follow the same behaviour as the IRT analysis, as shown in Figure 4.13, and the convergence of the log-Likelihood function (b) is monotonically increasing. The reconstructed density matrix (f) has non-zero values only in the even components, which decrease in magnitude as they move further from zero, as expected.

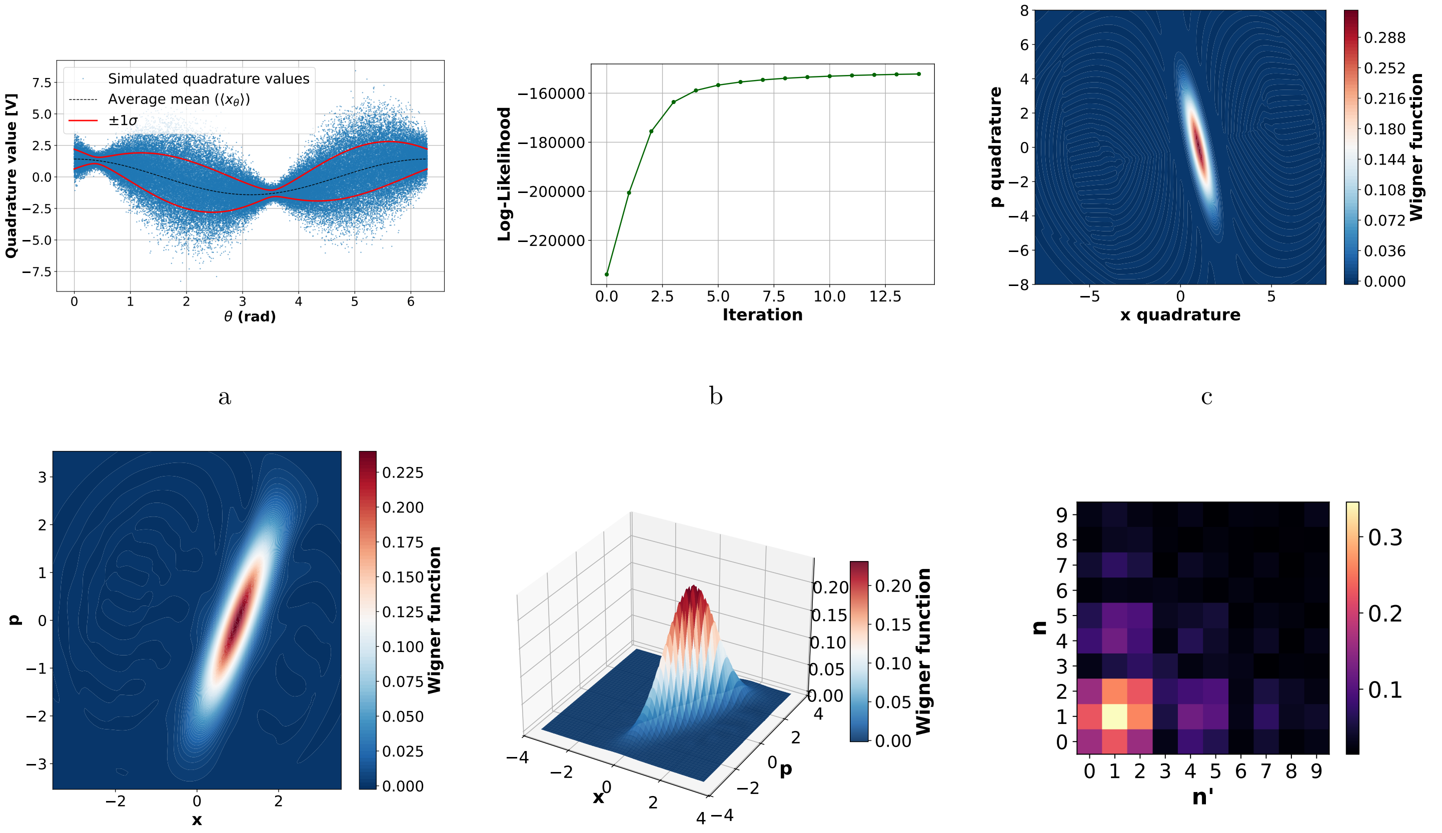

a b c

d e f

Figure 5.4: The figure above shows the simulation of a displaced squeezed state with coherent parameter $\alpha = 1 + 0j$, displacement parameter $r = 1$, rotation angle $\theta = 0.4$ rad, 20 phases, and a total of 10^5 points, simulated with Fock dimension $N_{fock} = 20$. The achieved results in both the two-dimensional (d) and three-dimensional (e) reconstructions are in line with the theoretical ones (c), as in the simulated trace (a). The log-Likelihood function convergence (b) shows a monotonically increasing behaviour, and the density matrix (f) behaves as a mixture of a coherent and a squeezed state, as expected from theory.

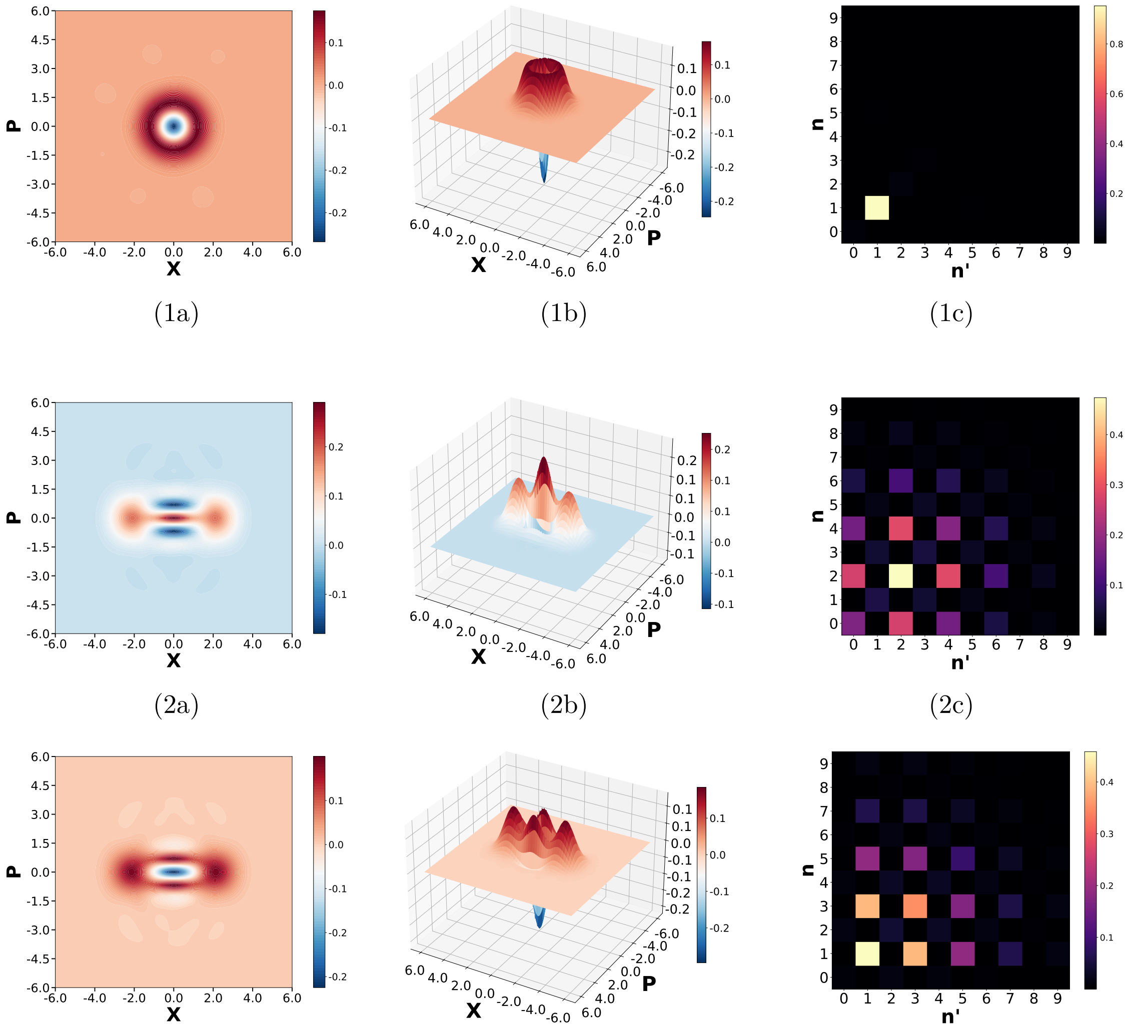

(1a) (1b) (1c)

(2a) (2b) (2c)

(3a) (3b) (3c)

Figure 5.5: The figure above presents the Wigner function reconstructions for a single-photon (1), even-cat (2), and odd-cat (3) states using 20 phases and 10^5 points, with 15 iterations of the MLE algorithm. In the left (a) and central (b) panels the two-dimensional and three-dimensional Wigner functions are shown, while the reconstructed density matrices are present in the right (c) panel. All the images follow the expected behaviour shown in Figure 2.9, proving that the here implemented MLE reconstruction can reconstruct also highly non classical states.

5.1.2 Number of required iterations

As illustrated in Section 2.3, the convergence of a tomographic algorithm strongly depends on the dataset. In the previous Chapter it was shown how the number of points can affect a particular tomographic algorithm: the Inverse Radon Transform; here the same analysis is reported for the MLE.

The MLE implemented in this code is designed in such a way it is able to reconstruct the density matrix of the state $\hat{\rho}$. The evolution between successive density matrices is governed by the operator defined in Eq. 5.1.10, and reads:

$$\rho^{k+1} = \frac{R(\hat{\rho}^k)\hat{\rho}^k R(\hat{\rho}^k)}{\mathrm{Tr}[R(\hat{\rho}^k)\hat{\rho}^k R(\hat{\rho}^k)]} = F(\hat{\rho}^k), \tag{5.1.19}$$

where $F(\hat{\rho}^k)$ is a map able to generate the next iteration: $F(\hat{\rho}^k) = \hat{\rho}^{k+1}$. If $\hat{\rho}^k$ indicates the density matrix at iteration k. As before anticipated, only few iterations are needed to achieve the convergence, as shown in Figure 5.6.

It is common practice to distinguish between the ideal density matrix maximizing the Likelihood function $\hat{\rho}^*$ in the ideal framework with respect to the real one, estimated by the data: $\hat{\rho}$.
In this work this division is not stressed; however, as previously mentioned, the Likelihood function is able to estimate the ideal density only in ideal conditions.
Supposing now this density exists (and it does since the MLE is a converging algorithm [41]), then it is possible to define an error δ_k at the k^{th} iteration defined as the change between the two iterations:

$$\delta_k = \hat{\rho}^k - \hat{\rho}^*. \tag{5.1.20}$$

Using the Taylor expansion truncated at the first order:

$$\begin{aligned} \hat{\rho}^{k+1} = F(\hat{\rho}_k) &= F(\hat{\rho}^* + \delta_k) \\ &= F(\hat{\rho}^*) + J\delta_k + \mathcal{O}(||\delta_k||^2) \\ &= \hat{\rho}^* + J\delta_k + \mathcal{O}(||\delta_k||^2) \sim \hat{\rho}^* + J\delta_k, \end{aligned} \tag{5.1.21}$$

where the identity $F(\hat{\rho}^*) = \hat{\rho}^*$ was used (with $\hat{\rho}^*$ as the target density), and J is the Jacobian matrix defined as $J = \frac{\partial F}{\partial \rho}\Big|_{\rho^*}$.
It follows that:

$$\hat{\rho}^{k+1} = \hat{\rho}^* + \delta_{k+1} \sim \hat{\rho}^* + J\delta_k \implies \delta_{k+1} \sim J\delta_k, \tag{5.1.22}$$

and, iterating k times:

$$\delta_k \sim J^k \delta_0, \tag{5.1.23}$$

if δ_0 is the initial error (starting *distance* with respect to the target density $\hat{\rho}^*$).
Using the Frobenius Norm ($||\delta_k|| \leq ||J^k||||\delta_0||$), and applying the Gel'Fand formula ($r_\lambda = \lim_{k\to\infty} ||A^k||^{\frac{1}{k}}$), one can achieve:

$$||\delta_k|| \leq \left[\left(||J^k||\right)^{\frac{1}{k}}\right]^k ||\delta_0|| = r_\lambda^k ||\delta_0||, \tag{5.1.24}$$

where r_λ is the spectral radius: the maximum modulus of the spectra of J [48].
Defined now an error $\varepsilon \geq 0$, one can search for the minimum number of iterations that allows for:

$$||\delta_k|| \leq \varepsilon. \tag{5.1.25}$$

Then:

$$\begin{aligned} ||\delta_k|| \leq ||\delta_0|| r_\lambda^k &\implies \frac{\varepsilon}{||\delta_0||} \leq r_\lambda^k \\ &\implies k \geq \frac{\ln\left(\frac{\varepsilon}{||\delta_0||}\right)}{\ln\left(r_\lambda\right)}. \end{aligned} \tag{5.1.26}$$

One can notice that r_λ is a way to characterize *how much* an error is shrunken (or enlarged) at every iteration; the fact that $r_\lambda < 1$ for each iteration (in ideal conditions) is another way to prove that the error is always minimized by the MLE convergence algorithm [49], consistently with what was stated before.
In particular, one expects that if the initial density is very far from the target one, $r_\lambda \to 1$, a high number of iterations is required.
On the contrary, if the density is very close to the target one, therefore $r_\lambda \to 0$, a very small number of iterations is required.

Supposing now to have n different (i.i.d.) measurements for a given phase, then the average value between them is defined as:

$$\bar{X}_n = \frac{X_1 + \cdots X_n}{n} \to \mathbb{E}[X_1] \tag{5.1.27}$$

where $\mathbb{E}[\cdot]$ defines the expected value.
Therefore, it is always possible to define an error ε such that, in the sense of probabilities:

$$\mathbb{P}[|\bar{X}_n - \mathbb{E}[X_1]| > \varepsilon] \to 0 \qquad\qquad n \to \infty, \tag{5.1.28}$$

and usually $\varepsilon \to 0$ in order to maximize the convergence.
Namely, the sample mean converges to the expected value X_1 as the number of measurements increases. In such condition, the Central Limit Theorem (CLT) can be applied:

$$\sqrt{n}\left(\bar{X}_n - \mathbb{E}[X_1]\right) \to \mathcal{N}(0, \sigma^2), \tag{5.1.29}$$

for some variance σ^2. So, as long as the number of measurements is high enough, their distribution will resemble a normal distribution with mean 0 and a small standard deviation. This standard deviation in inversely proportional to the Fisher information of the dataset [43], as before anticipated, thus reciprocal to the number of data [47].

Therefore it is logical to expect that, depending on the number of points, the convergence of the MLE will determine the quality of the convergence.

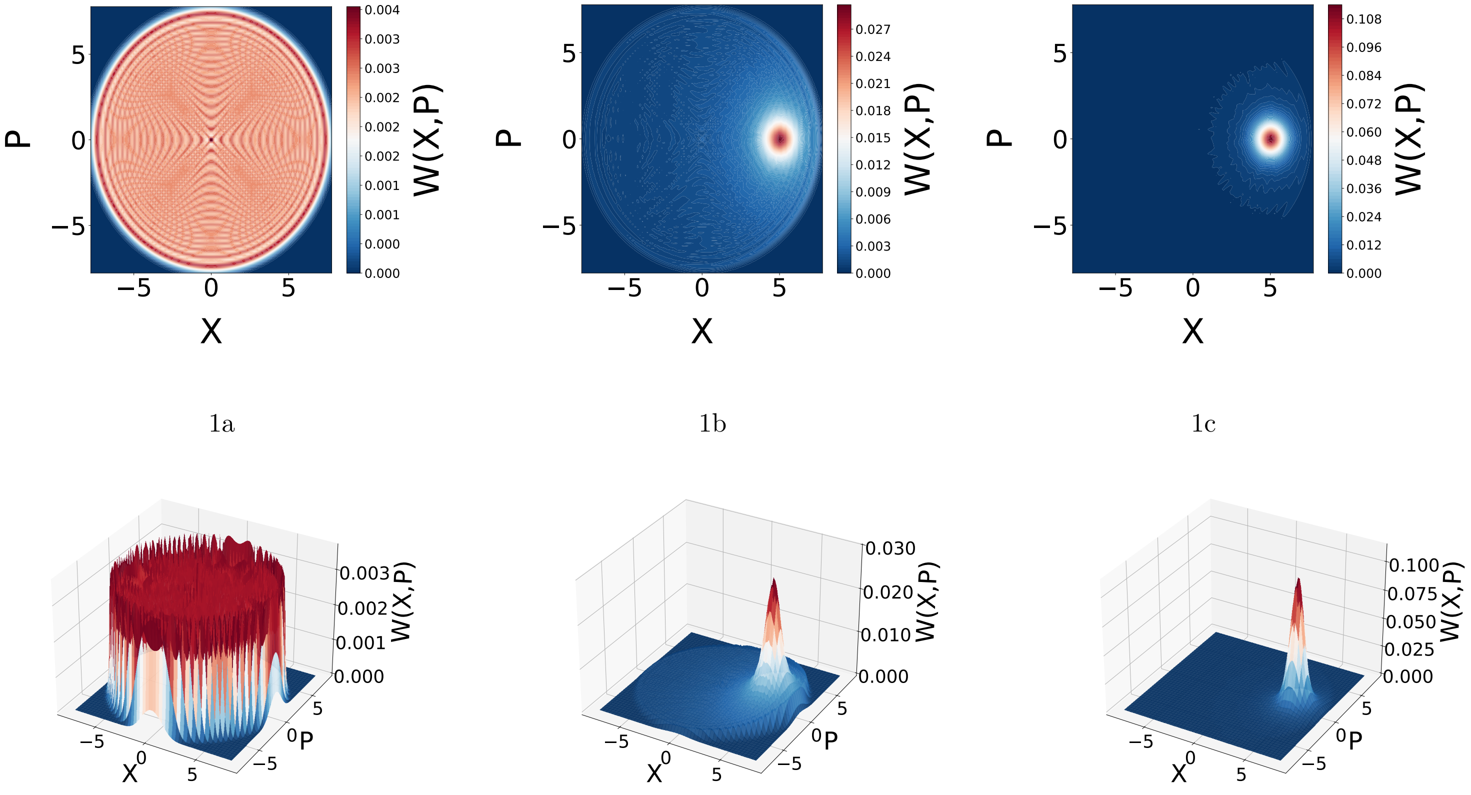

1a 1b 1c

2a 2b 2c

Figure 5.6: In the image above, the Wigner function of a simulated coherent state with coherent parameter $\alpha = 5 + 0j$ is shown, both from a two-dimensional (1) and from a three-dimensional (2) perspective, for the initial density (a), the first (b), and the second (c) iteration. The code assumes a completely mixed state as the initial density matrix ($\hat{\rho}_0 = \frac{\mathbb{I}}{N}$), whose corresponding Wigner function is shown in a. The algorithm then iteratively updates the density matrix using the simulated data as a probability distribution, implementing the update formula in Equation 5.1.3. As can be seen, the convergence is monotonic, and the state becomes already well-defined after only a few iterations. This behaviour holds for simulated data; however, convergence can take require a higher number of iterations for a real experiment due to noise and limited data availability.

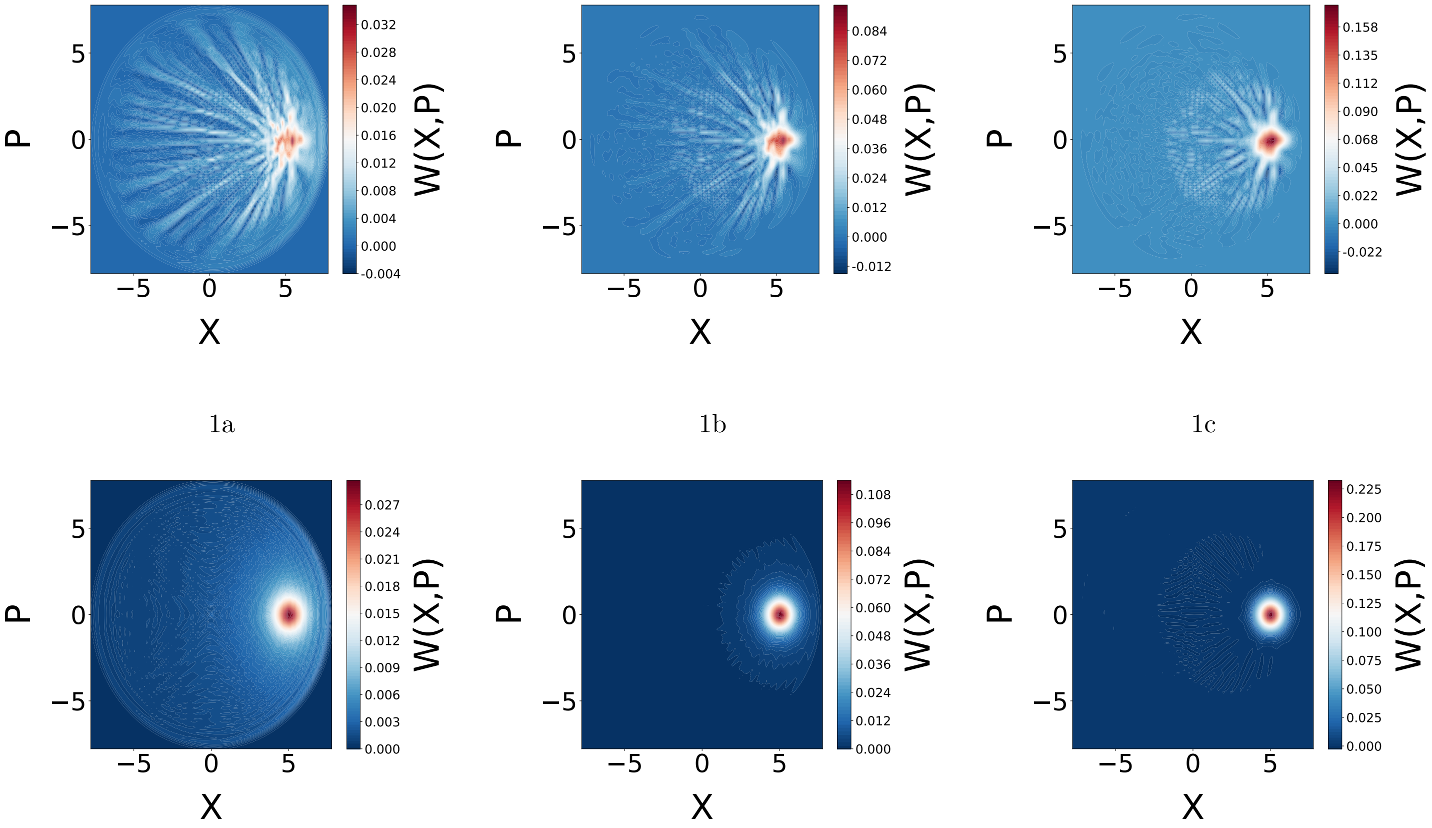

1a 1b 1c

2a 2b 2c

Figure 5.7: In the above, the Wigner reconstructions obtained using the MLE algorithm are shown for a total of 100 (1) and 10^5 (2) points, with 20 different phase values. Panels (a), (b), and (c) respectively show the reconstructed Wigner functions at the first, second, and fifth iteration of a coherent state with coherent parameter $\alpha = 5 + 0i$, starting from a completely mixed density matrix. At first glance, it is evident that the Wigner functions reconstructed with 10^5 points are much clearer than those obtained with only 500 points at each iteration. Moreover, simulations using a larger number of data points the converge significantly faster. The slower convergence observed for smaller datasets is due to the limited amount of information available.

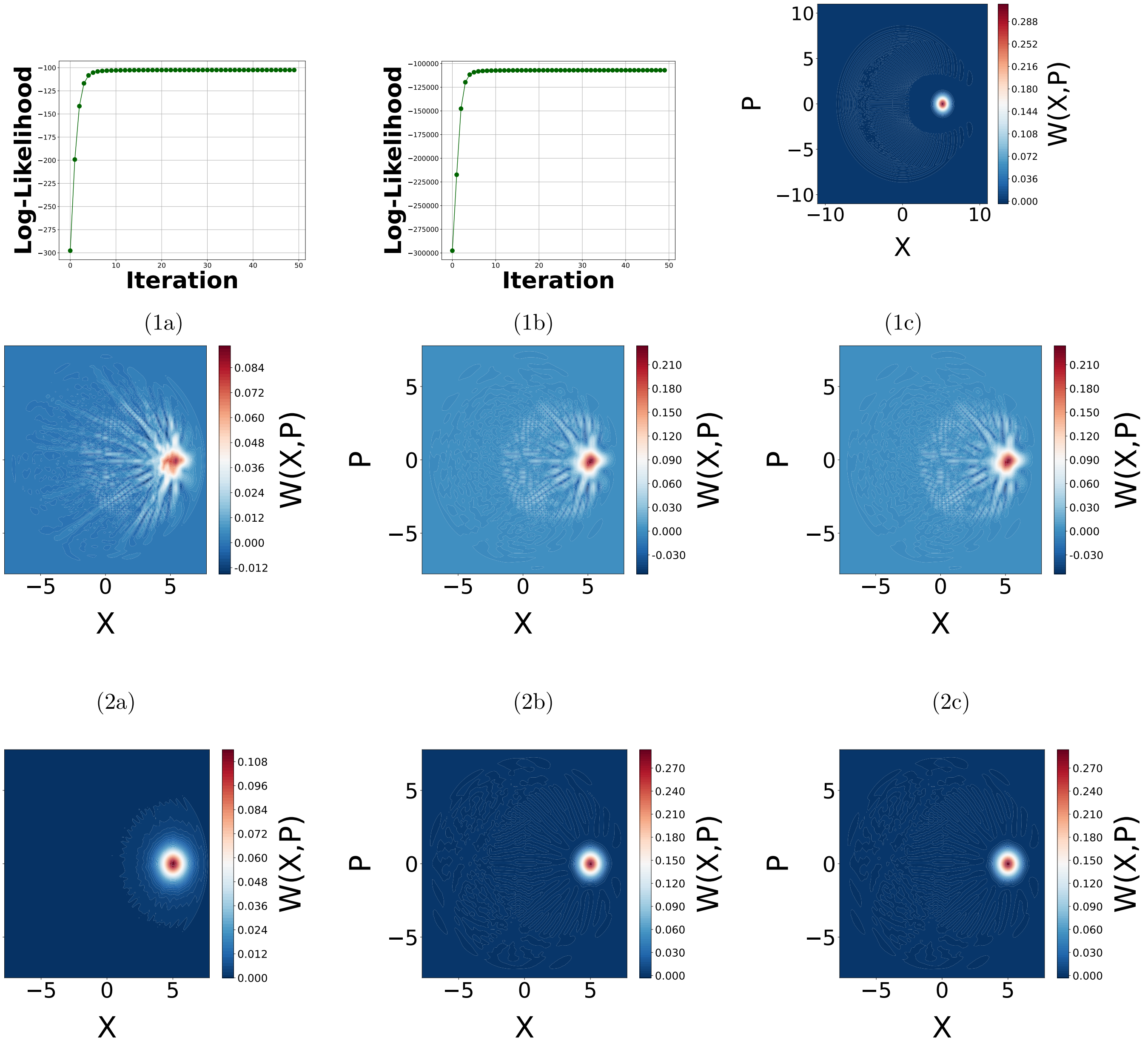

(1a) (1b) (1c)

(2a) (2b) (2c)

(3a) (3b) (3c)

Figure 5.8: In the figure above, the Log-Likelihood evolution is shown for 100 (1a) and 10^5 (1b) points, together with the expected Wigner function in Figure (1c). Panels 2 and 3 display the Wigner reconstructions using 100 and 10^5 points and 20 phase values at iteration 3, 40, and 41, respectively. It is evident that the algorithm exhibits *saturation* in both cases after a number of iterations, as most of the information has already been extracted. Moreover, one can observe that using 100 points at iteration 42 still produces a Wigner function that is worse than the one obtained after only 15 iterations with 10^5 points.

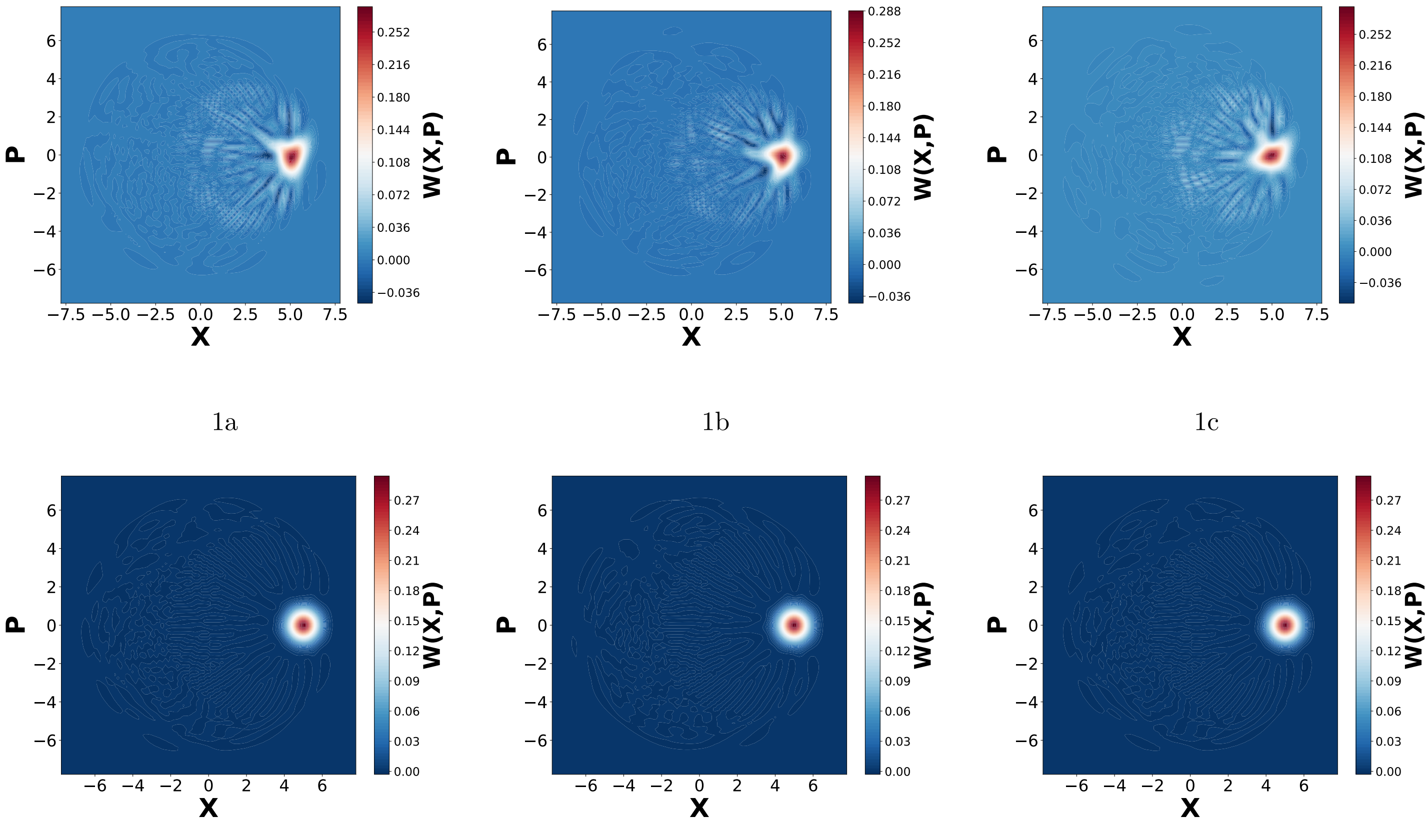

1a 1b 1c

2a 2b 2c

Figure 5.9: In the figure above are shown different Wigner reconstruction achieved by using a total of 100 (1) and 10^5 (2) simulated points, a total of 20 phases and 15 iterations for three different simulations (a,b,c). As can be seen, using 10^5 points the achieved Wigner function is correct and well-behaved; moreover the convergence Wigner (thus the achieved density matrix), is almost the same independently on the simulation. On the contrary, by using 100 points, the achieved Wigner shows a high baseline level and lower maxima, and it is changing dependently on the simulation. This behaviour is expected since higher oscillations are achieved once the convergence Wigner is achieved by using a lower amount of points, as derived in Appendix 6.12.

5.1.3 The Fock dimension

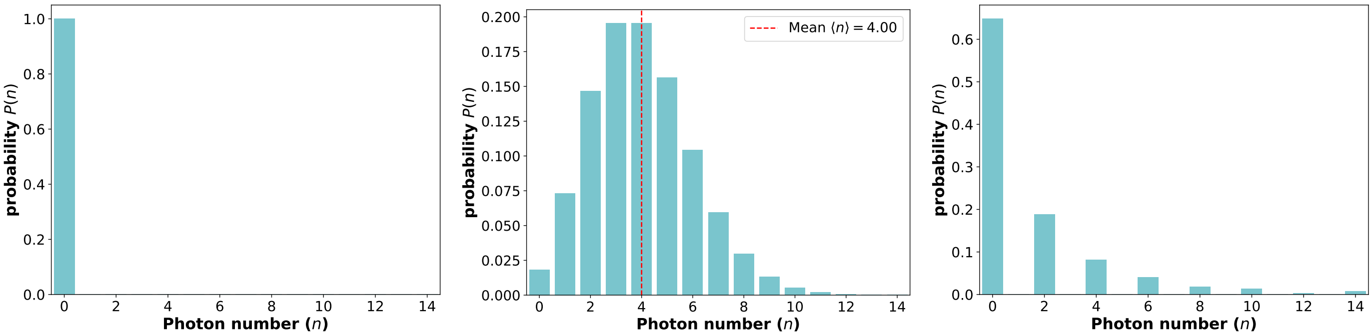

(a) (b) (c)

Figure 5.10: In the figure above the simulated Photon statistics for the vacuum (a), coherent (b) and squeezed vacuum states (c) are shown. As expected the vacuum state is centred at zero (since no photons are present), while the coherent state has a Poissonian distribution around the mean $|\alpha|^2$ and the squeezed state is described only by even pairs, since the generation started with $|0\rangle$.

As a last limitation in the used model, there is the Fock dimension.
Following what shown in Section 2.2, the states of light have to be defined in the Fock space. Consequently, the Fock dimension is the maximum size one wants to consider of this space.
For instance, as shown in Figure 5.10, the vacuum state has components only at zero (since zero photons are present), while the coherent state has a Poissonian distribution, since it is a perfectly random state.
The Fock dimension, as before anticipated, is crucial in the MLE algorithm because of the evolution equation 5.1.3; indeed the operator $\hat{\Pi}$ inside $\hat{R}$ has to be defined in the Fock basis through equation 5.1.10.
If the Fock space is not sufficiently high, one risks to cut some meaningful information, thus resulting in a bad convergence of the algorithm.

Suppose $|n\rangle_{n=0}^{\infty}$ is the complete Fock basis, then by setting a Fock space lower than infinity, one is effectively projecting the state through a projector:

$$\hat{P}_N = \sum_{n=0}^{N-1} |n\rangle \langle n| \,, \tag{5.1.30}$$

thus reducing the space.
Therefore, the infinite-dimensional (in the Fock basis) density operator $\hat{\rho}_{true}$ is reduced into:

$$\hat{\rho} = \frac{\hat{P}_N \hat{\rho}_{true} \hat{P}_N}{\mathrm{Tr}[\hat{P}_N \hat{\rho}_{true}]}, \tag{5.1.31}$$

where $\left[\hat{P}_N \hat{\rho}_{true}\right]$ is a normalization factor.

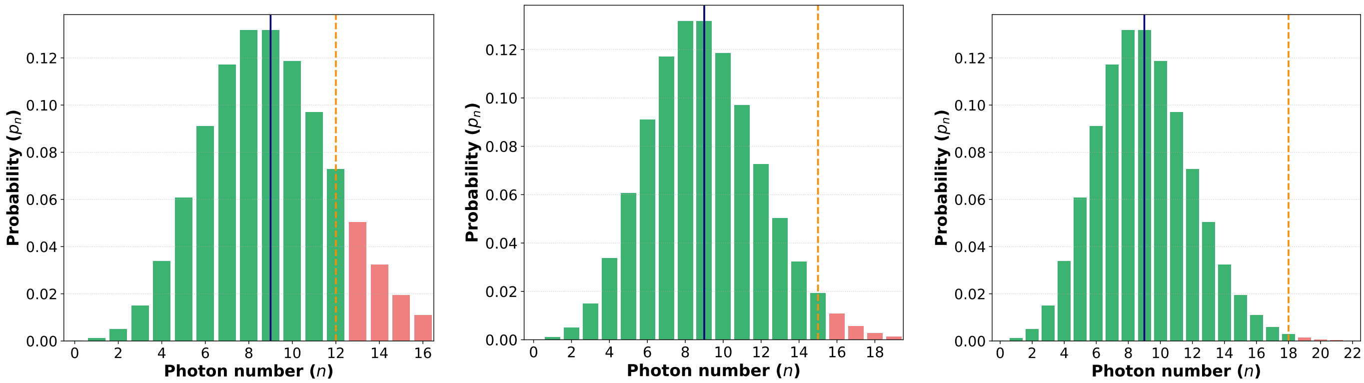

(a) (b) (c)

Figure 5.11: In the figure above, the photon number distribution of a coherent state (Poissonian in the Fock space) with mean photon number $|\alpha|^2 = 9$ is shown. The state is represented with a truncated Fock space of dimension $|\alpha|^2 + k|\alpha|$, for $k = 1$ (a), 2 (b), and 3 (c). The covered probability region is highlighted in green, while the missing tail probability p_{tail} is shown in red. The corresponding numerical results are summarized in Table 5.1.

Hence, the probability to have components outside the truncated Fock space is:

$$p_{tail} = 1 - \mathrm{Tr}[\hat{P}_N \hat{\rho}_{true}] = \mathrm{Tr}[(\mathbb{I} - \hat{P}_N)\hat{\rho}_{true}], \tag{5.1.32}$$

and, if one is measuring a generic operator $\hat{O}$ (for example the number operator $\hat{n}$ or the quadrature operator $\hat{X}_\theta$), the truncation could be modelled as:

$$\Delta_{\hat{O}} = \left|\mathrm{Tr}\left[\hat{O}\hat{\rho}_{true}\right] - \mathrm{Tr}\left[\hat{O}\hat{\rho}\right]\right| = \left|\mathrm{Tr}\left[\hat{O}\left(\mathbb{I} - \hat{P}_N\right)\hat{\rho}_{true}\right]\right| \leq ||\hat{O}||\hat{\rho}_{true}. \tag{5.1.33}$$

Being $|f_m\rangle$ the Fock vector, if the Fock dimension is not high enough some information is lost.
As a rule of thumb, the Fock space has to be estimated at least as the mean photon number present in the state (this gives the displacement of the distribution), plus a certain amount k of variances (usually $k \geq 3$) able to catch the spread of the distribution:

$$N_{fock} = \langle n \rangle + k\langle n \rangle. \tag{5.1.34}$$

For instance, if one is looking at a coherent state, then $\langle n \rangle = |\alpha|^2$ and $\mathrm{Var}[\langle n \rangle] = \sqrt{\langle n \rangle} = |\alpha|$, so, by changing between $k = 1, 2, 3$ the results in table 5.1 can be achieved. Where p_{tail} is the non-covered probability, p_{cov} is the covered probability and Fock dim is the dimension of the Fock space.

The distributions for a coherent state by varying the Fock space are shown in Figure 5.11, while the rebuilt Wigner functions are shown in Figure 5.12.

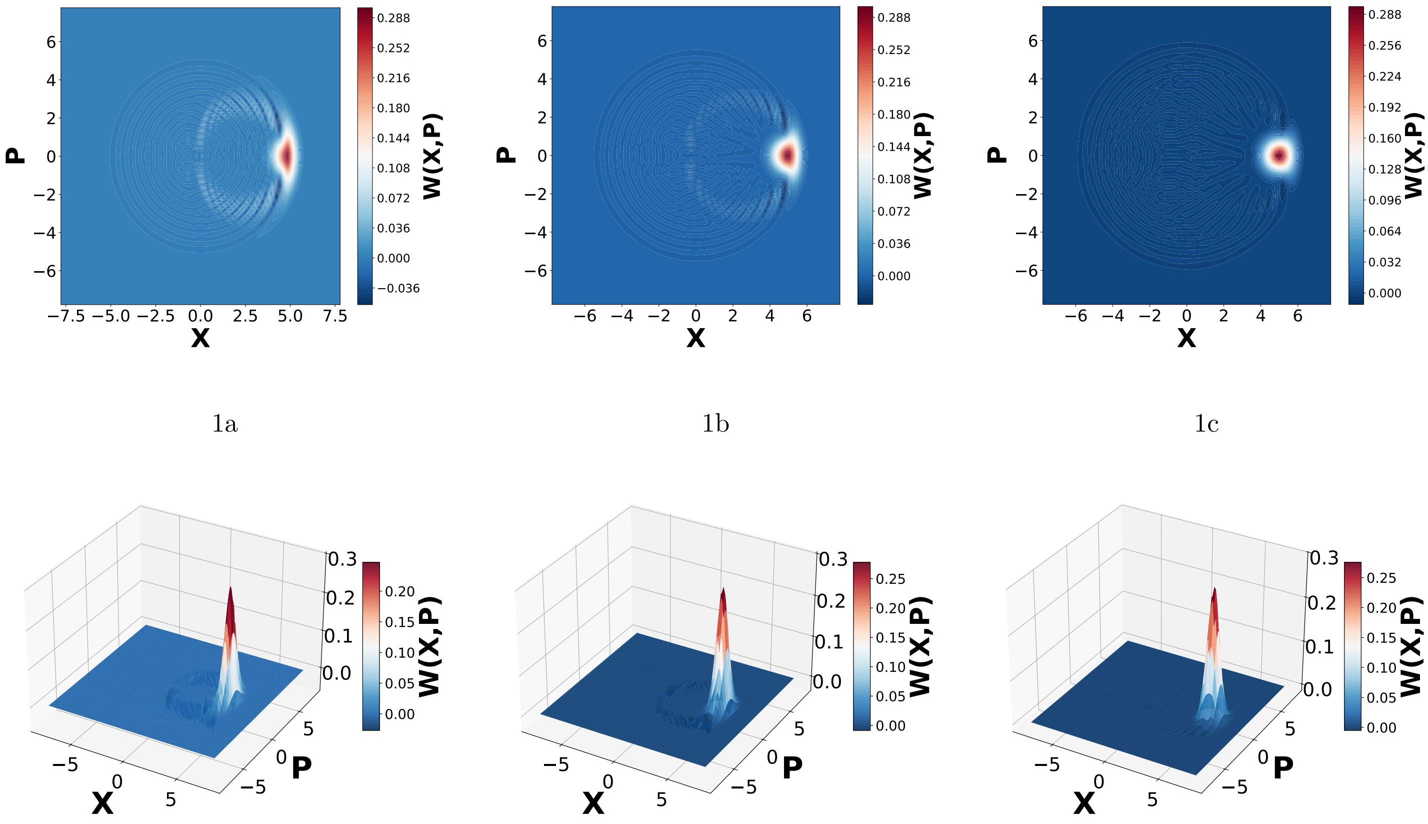

1a

1b

1c

2a

2b

2c

Figure 5.12: In the figure above are shown the Wigner reconstruction by simulated data for a coherent state with coherent parameter $\alpha = 5+0j$, a total of 10^5 points divided in 20 uniformly distributed phases. The Fock dimension was chosen to be $N_{fock} = |\alpha|^2 + k|\alpha|$, accordingly to formula 5.1.34 for k = 1 (a), 2 (b) and 3 (c); both the two-dimensional (1) and three-dimensional (2) Wigner functions are plotted. As expected, the higher is the used k parameter and the higher is the Fock dimension, allowing for a better convergence. However, in simulations and data analysis, k = 5 was used since better results were achieved as shown in Figure 5.13.

k	**Fock dim**	p_{cov}	p_{tail}
1	12	87.58%	12.42%
2	15	97.80%	2.2%
3	18	99.76%	0.24%

Table 5.1

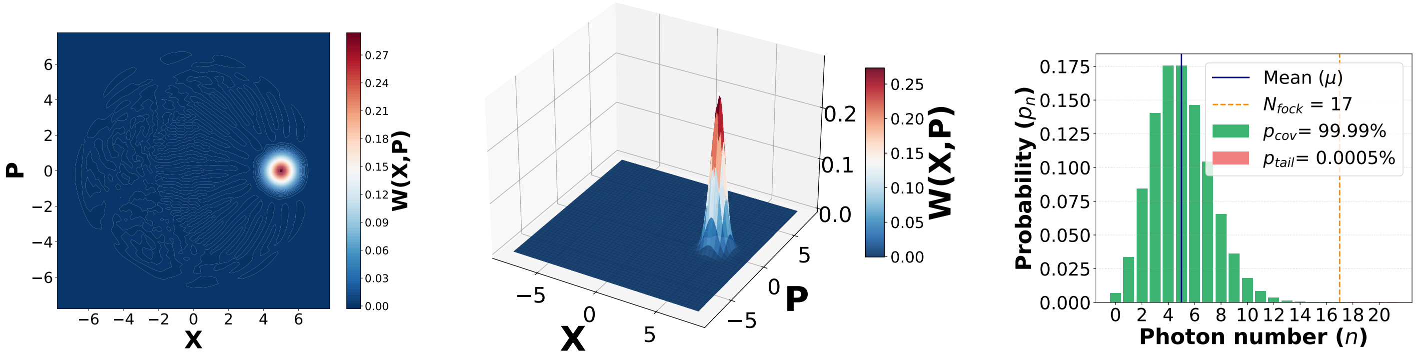

(a) (b) (c)

Figure 5.13: In the image above, the Wigner function reconstruction from simulated data of the coherent state shown in Figure 5.7 with $k = 5$ is presented. As can be seen in both the two-dimensional (a) and three-dimensional (b) Wigner representations, the state closely resembles a coherent state with coherent parameter $|\alpha| = 5 + 0j$. This is further confirmed by the photon-number histogram in the Fock space (c), where the uncovered probability p_{tail} is approximately zero.

As can be seen, with $k \gtrsim 3$ the statistic is well covered by the model, even if k = 5 was required for a better reconstruction.
Then one may wonder why not set a very high Fock dimension while retrieving the data in order to not lose probability. This *brute-force* solution however requires high memory computers in order to compensate for overflow and limited storage capabilities.
Indeed, the Fock wavefunctions are defined as:

$$\psi_n(x) = \mathcal{N}_n \cdot H_n(\xi) \cdot e^{-\xi^2/2} \tag{5.1.35}$$

with $\mathcal{N}_n$ normalization and $\psi_n = \langle n, \psi \rangle$.
The Hermite polynomials however go as:

$$H_n(x) = (-1)^n e^{x^2} \frac{d^n}{dx^n} e^{-x^2} \tag{5.1.36}$$

highly diverging on n. Using the notation `complex 128` in python, the maximum representable number should be close to, $\sim 10^{308}$ that corresponds to a truncated Fock dimension around $N_{max} \sim 170$.
Exceeding this limitation, overflow errors occur, effectively limiting the type of states one can measure/simulate.

It has to be noted that, since the Hermite polynomials are then multiplied by other quantities, and that the Fock wavefunction ψ_n also depends on the data, the maximum Fock dimension has to be lower than this value. Experimentally, a limitation was found around $N_{fock} \sim 150$.

5.1.4 From density matrix to the Wigner function

The log-likelihood function, as previously implemented, can reconstruct the density matrix of a state of light.

However, the goal of this work is to reconstruct the Wigner function of the state, that is the common way to characterize a state in quantum optics. As before stated, there is a one to one correspondence between the Wigner function and the density matrix, through the formula [7]:

$$W(X,P) = \frac{1}{2\pi}\int_{-\infty}^{+\infty} \langle X - \tfrac{v}{2}|\, \hat{\rho}\, |X + \tfrac{v}{2}\rangle\, e^{iPv}\, dv. \tag{5.1.37}$$

This formula belongs to the class of inverse Weyl transforms, where a quantum mechanical operator ($\hat{\rho}$) is connected to a phase function ($W(X,P)$).

The passage between the conversion to the achieved density matrix was then done by using the already implemented python function `Wigner`, present in the `QuTiP` package. The evolution of the density matrix in the Fock basis is shown in Figure 5.14.

As previously anticipated, a dependency between the number of used phases and the dimension of the reconstructed density operator is theoretically expected. However, this behaviour was not observed in our ideal simulations, when all other parameters were kept fixed, as shown in Figure 5.15.

This lack of visible dependence is probably due to the simplicity of the considered states, which are Gaussians.

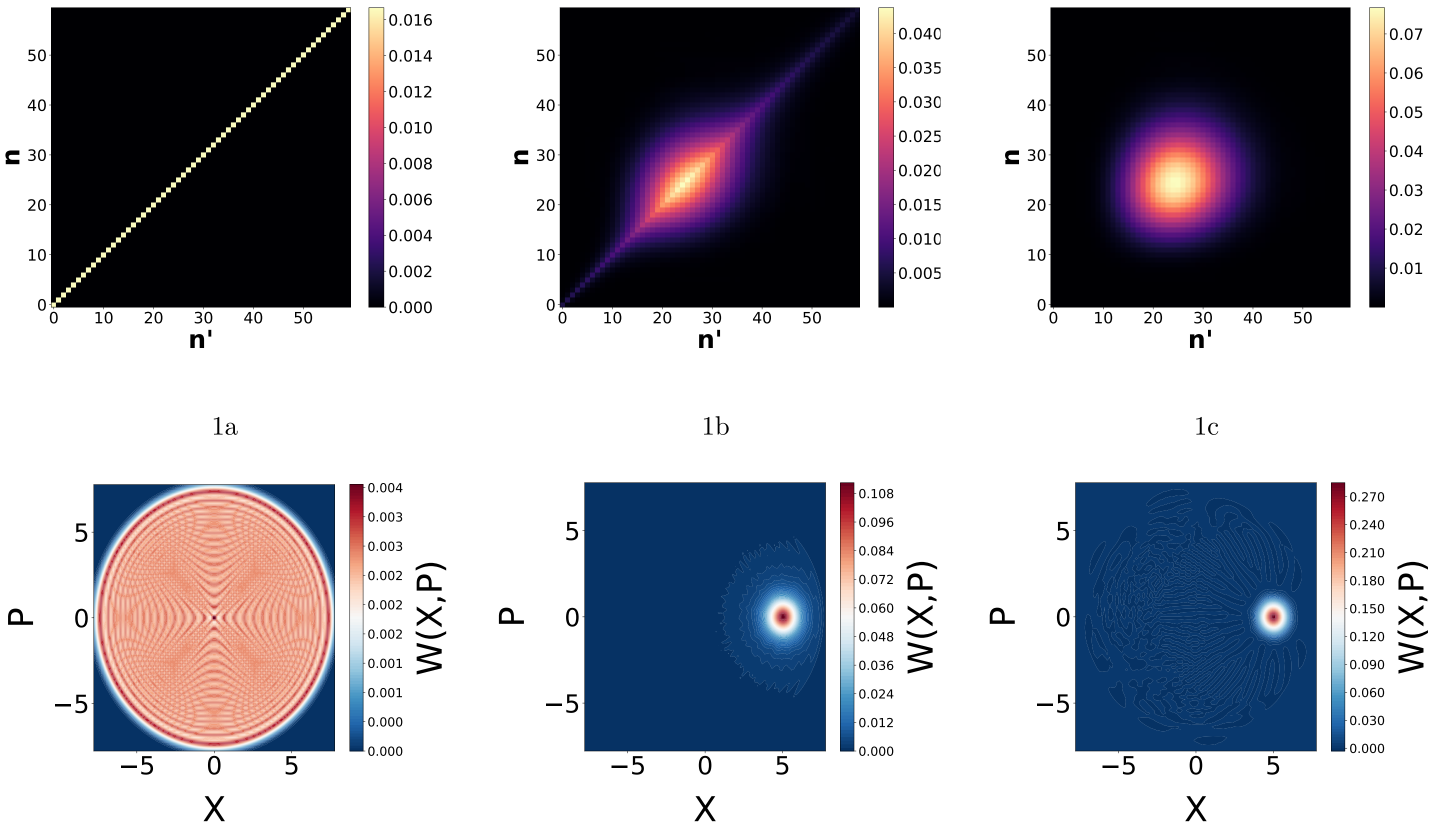

1a 1b 1c

2a 2b 2c

Figure 5.14: In the figure above, the evolution of the density matrix (1) and the corresponding two-dimensional Wigner function (2) is shown for the first (a), second (b), and eleventh (c) iterations of the MLE algorithm applied to a simulated coherent state with coherent parameter $\alpha = 5 + 0j$. A total of 10^5 points with 20 uniformly distributed phases were used. Consistent with Figure 5.7, after a few iterations the density matrix already exhibits suppression of all components far from the mean photon number $|\alpha|^2$, and its values begin to peak around that value with a Gaussian distribution, as expected.

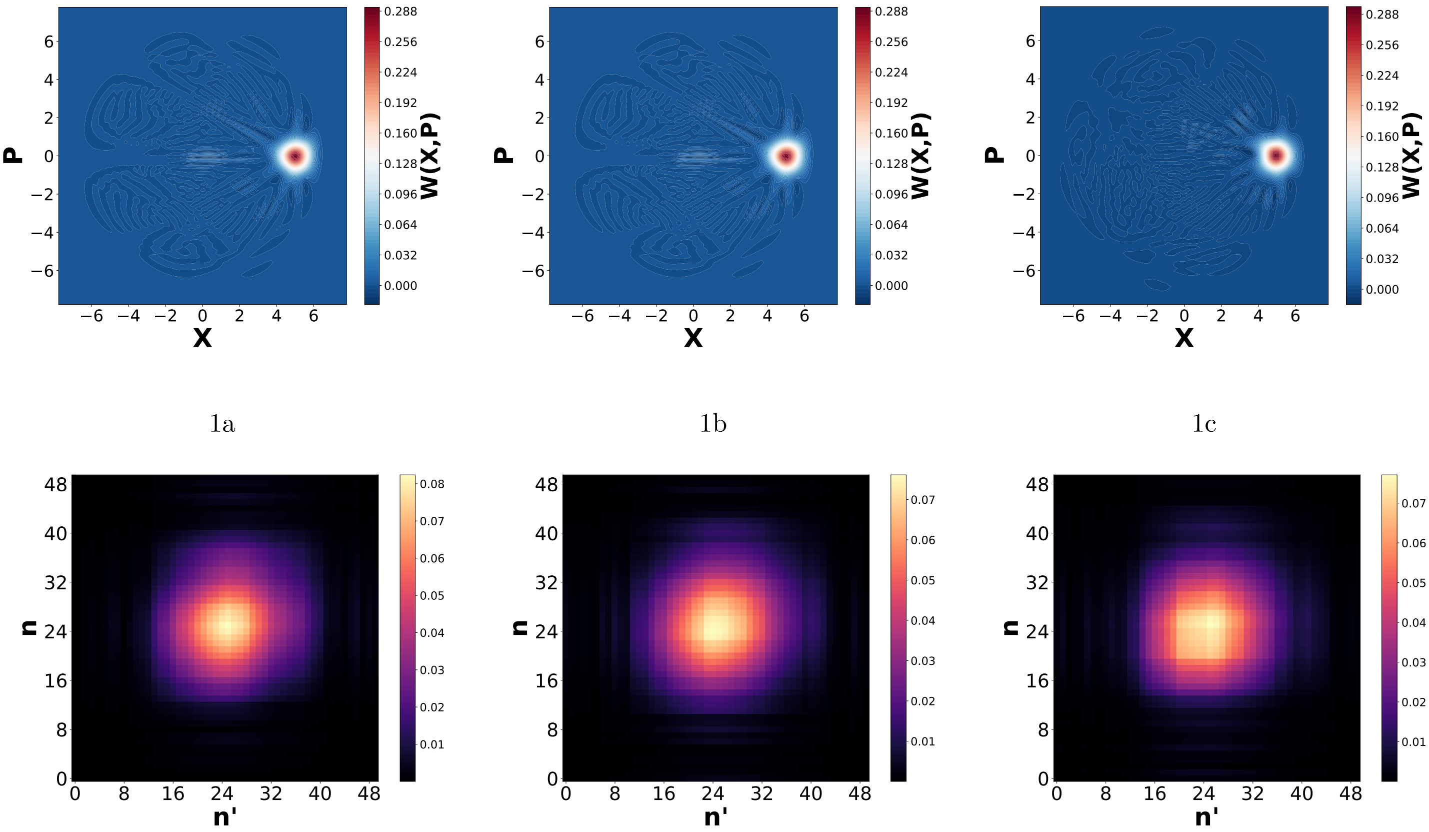

1a 1b 1c

2a 2b 2c

Figure 5.15: In the figure above, a coherent state with coherent parameter $\alpha \approx 5+0j$ was simulated using 10^3 sampled points and a Fock-space cutoff of $N_{\text{Fock}} = 50$. The number of phase angles was varied among 3 (a), 6 (b), and 15 (c). As can be seen, no significant phase dependence appears in either the Wigner reconstructions or the density-matrix reconstructions. This behaviour is likely due to the relatively large amount of data used ($\sim 10^3$ points). Since MLE is a redundant reconstruction algorithm, some information is still encoded even with a small number of phase samples. However, drastically reducing the number of sampled points is not a suitable approach, as it may introduce additional errors due to insufficient statistics, making it difficult to determine which factor is limiting the reconstruction.

5.2 Experiment results

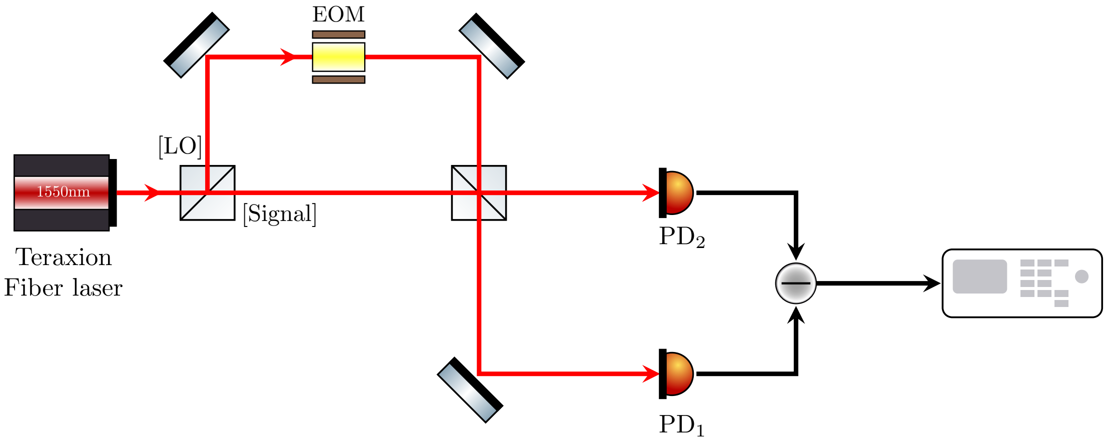

Figure 5.16: In the Figure the setup used for the MLE experiment (the same as the IRT one) is shown above. An ultra-stable laser (Teraxion TNL162630) operating around 1550 nm was used as the Local Oscillator. Due to phase instabilities, only calibration states (vacuum and coherent) were studied. The signal was therefore simply an attenuated beam coming from the Local Oscillator. A phase EOM (Electro-Optic Modulator) was used to achieve a controlled phase difference between the Local Oscillator and the signal, while interference was obtained through a Beam Splitter. The signal was then detected using the previously described Exalos EBR differential detector.

Now that the behaviour of the code is well understood and has been proven to work properly, the analysis of real data can proceed.

The setup used for the second experiment is essentially the same as the one described in Section 4, reported in Figure 5.16 for convenience. The same ultra-stable laser (Teraxion TNL162630) with a previously measured linewidth of 300 Hz was used as the Local Oscillator (LO) with a fixed output power of 10 dBm. The phase difference between the signal and the Local Oscillator was introduced using an MPZ-N10 electro-optic modulator (EOM). The signal and Local Oscillator were then combined at a beam splitter, and the output was measured using a differential Exalos EBR370005-02 photodiode, as in the Inverse Radon Transform experiment; the losses were again estimated to be ($\sim 8.7 \pm 0.02$) dB.

Also in this experiment, due to phase instabilities, the light state emitted by the quantum well laser driven with quiet pump was not measured. Therefore, only calibration states were characterized.

In order to feed the modulating signal to the EOM, the Agilent 33522A Arbitrary Waveform Generator has been used.
The modulating signal was spanning between $V_0 = 0$ and $V_\pi = 4$ in order to cover the $[0, \pi]$ phase range, as in the IRT experiment.
The modulation was generated in order to have jumps between the different voltage signals (then converted into phase values) in order to well define the various intervals, as

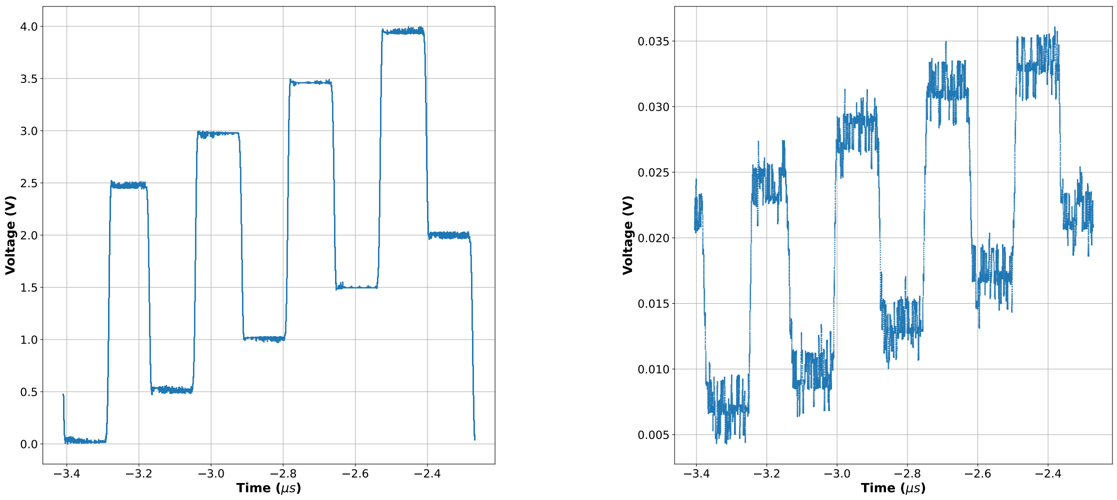

(a) (b)

Figure 5.17: In the figure above are shown the generated voltage signal (a) and the achieved interference pattern (b). As can be seen the stability of the Teraxion allowed us to achieve a very clean trace; the shifting between the signal and the voltage is due to an intrinsic delay between the generated modulating signal and the trace, then fixed during the post processing.

shown in Figure 5.17.

The signal had a frequency of approximately 1 MHz, corresponding to a period of $T \sim 1\ \mu$s. However, the Arbitrary Waveform Generator introduces transients between the different phase jumps. This induces some non-idealities, as different voltages (and thus different phases) are explored in an unwanted way. To overcome this issue, some points were removed from each segment where the phase was constant, slightly reducing the precision of the algorithm.

Each acquisition was again composed of three parts: an *off_acquisition*, where both the signal and the Local Oscillator (LO) were off; a *lo_acquisition*, where only the LO was on; and an *on_acquisition*, where both the signal and LO were on, as in the IRT analysis. Using the off and LO acquisitions, the shot noise was estimated for each measurement, allowing proper normalization of the acquired trace in shot noise Units (SNU).

The results for both vacuum and coherent traces are shown in Figure 5.19.
As can be seen, the vacuum reconstruction clearly exhibits a Gaussian function centred in the phase space, as expected. Since the vacuum trace is phase-independent, the modulator jumps did not introduce any non-idealities in the data, allowing no points to be removed. This results in better convergence (Figure 5.20) and analysis.

The achieved density matrix only has the $|0\rangle$ state in the Fock basis: $\hat{\rho} = |0\rangle\langle 0|$, as expected, since no photons are present in the vacuum state. Approximately 2000–2500 points per phase were measured for a total of 9 phases, yielding about 2.5×10^4 points

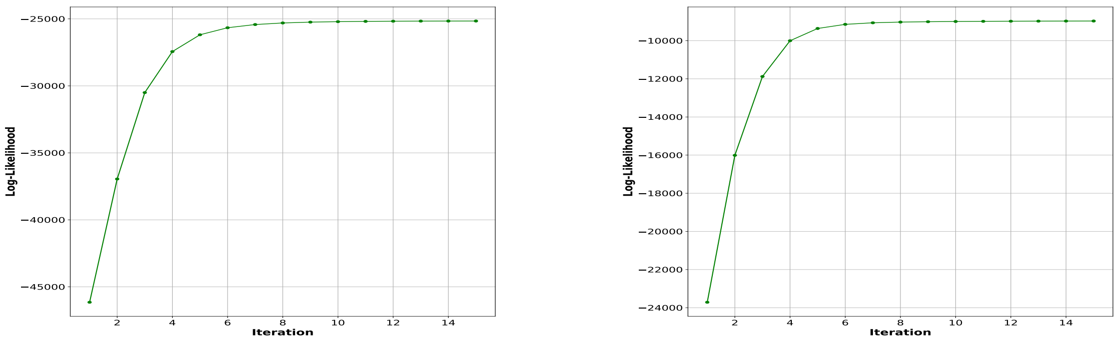

(a) (b)

Figure 5.18: In the figure above, the Log-Likelihood evolution for the vacuum state (a) and the coherent state (b) are shown. As can be seen, the convergence in both cases is achieved in a low amount of iterations (~ 5). In particular, the vacuum trace has a more abrupt and direct raise, mostly due to the higher number of points for phase, and achieve a more stable convergence. On the other hand, the coherent state has a softer raise and still some small improvements are present after the initial iterations. Nevertheless, improving the number of iterations is not leading to an appreciable better Wigner function, symbol that most of the information was already gained by the algorithm.

overall. This was possible thanks to the high speed oscilloscope used, with a sampling frequency of ~ 25 GSa/s.

The convergence was achieved in a quite direct way after almost 15 iterations of the algorithm, starting with a completely mixed density matrix ($\hat{\rho} = \frac{1}{N}\sum_i |\psi_i\rangle\langle\psi_i|$) with a Fock dimension $N_{fock} = 5$.

For what concerns the coherent state reconstruction, a high attenuation was used in the signal branch; necessary in order to allow for reconstructions with a lower Fock dimension, as discussed in section 5.1.3. The signal fiber was slightly disconnected in order to achieve a higher attenuation. This allowed us to achieve an estimated coherent parameter $\alpha \sim 3$.
The density matrix reconstruction shows an almost Poissonian distribution correctly centred at $|\alpha|^2 \sim 16$ consistent with the shift of the Wigner function in $|\alpha| \sim -3-4$.
The reconstructed Wigner function exhibits some ripples and some small negativities, moreover the shape is not a clear Gaussian distribution. These unexpected errors are likely due to numerical artefacts and residual noise in the measured data and are coming from the fact that in the density matrix some elements are non-zero, also far from the Poissonian distribution in $|\alpha|^2$.
Nevertheless, the Wigner reconstruction shows a clearly displaced coherent state, proof that the reconstruction went well.
Since the coherent trace is phase dependent (as expected and shown in Figure 5.17), some points had to be discarded in order to compensate for the transients while modulating

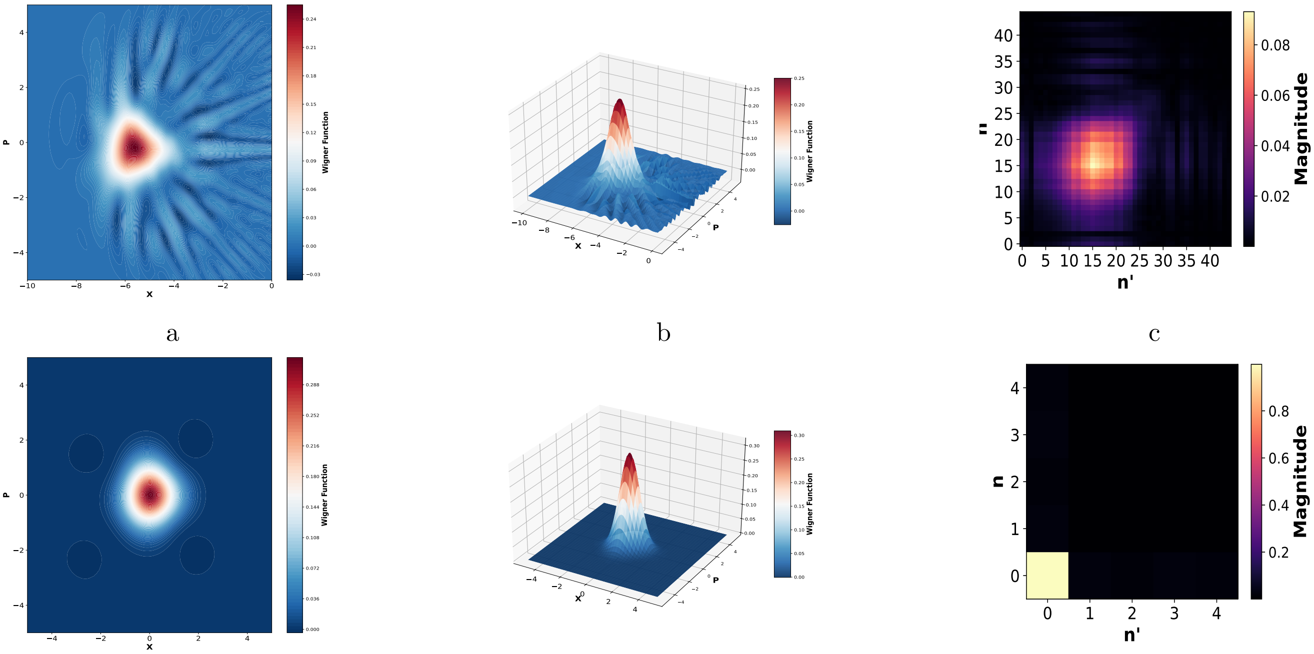

a b c

d e f

Figure 5.19: In the figure above, the measured data for vacuum (above) and coherent (below) states are reported. The coherent Wigner function, both from a three-dimensional (b) and two-dimensional (a) perspective shows non-idealities such as negativities, ripples, and spreading in probability, likely due to residual noise and insufficient points. However, in the rebuilt density matrix (c), the state resembles a coherent state with an associated coherent parameter $\alpha \sim 4-5$, consistent (in this reconstruction the quadrature operators were defined with the $\sqrt{2}$ normalization factor) with the plotted Wigner functions. On the other hand, the Wigner functions for the vacuum state, both in the two-dimensional (d) and three-dimensional (e) perspectives, show a Gaussian function centred at zero. The plane baseline shows zero probability as expected, except where the Gaussian distribution is present. Also, the achieved density matrix (f) shows a non-zero value only in $|0\rangle\langle 0|$, as expected.

between two far voltages. A total of 1000 points were removed from each segment, effectively lowering its number to ~ 1000 per each phase.
This lack of points likely affected the Wigner reconstructions, introducing errors; nevertheless, different simulations of the same dataset let to almost the same Wigner distribution (and density matrix), as shown in Figure 5.21. This proves both that with this number of points the algorithm is stable and that the non idealities present in the density matrix are not due to an error in the computation but are intrinsic to the dataset.

[p]

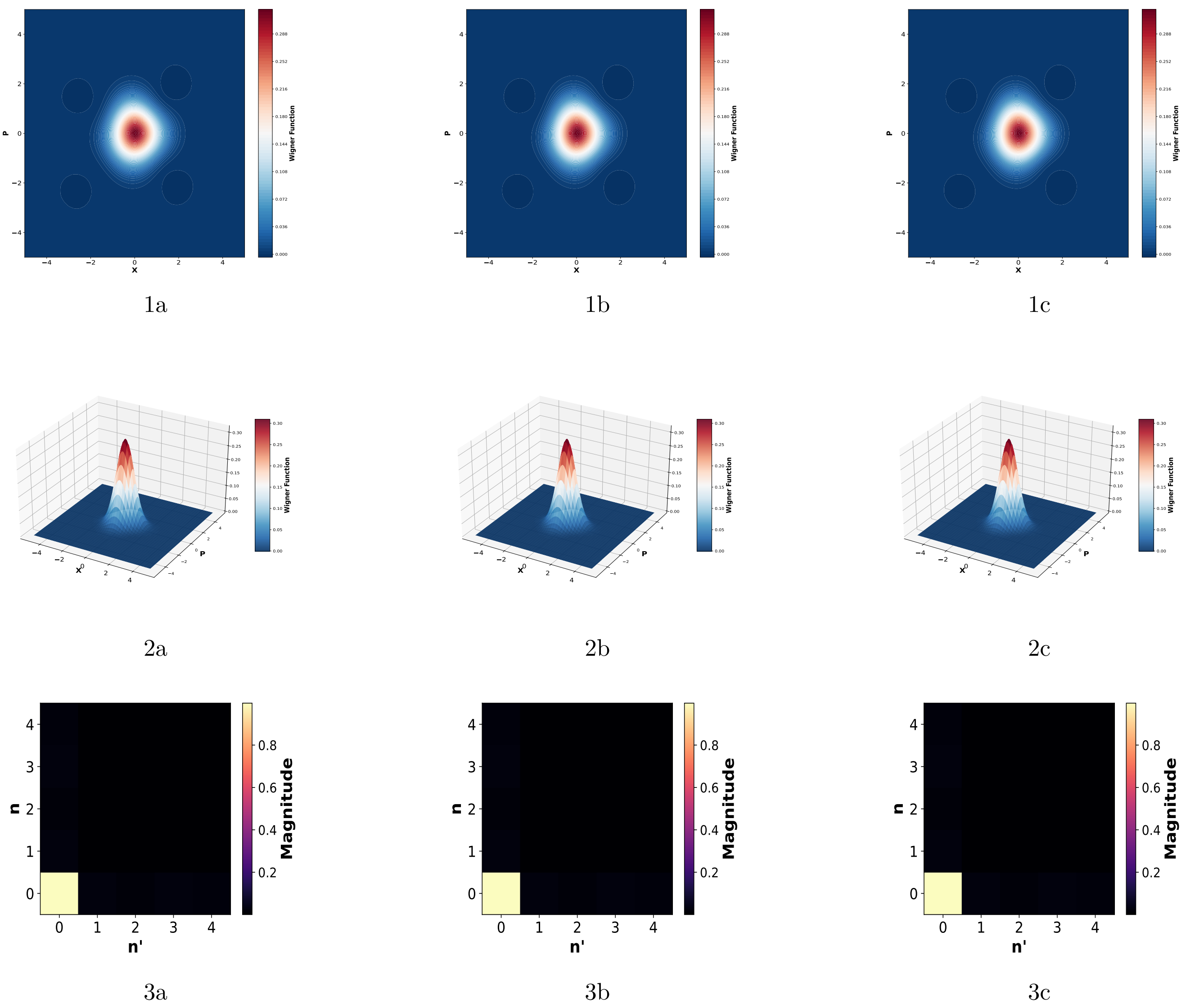
1a 1b 1c

2a 2b 2c

3a 3b 3c

Figure 5.20: In the image above, three different Wigner reconstructions of the same dataset for the vacuum state are shown. As can be seen, both in the two-dimensional (1) and three-dimensional (2) Wigner functions and in the density matrices (3) after 15 iterations, good convergence is observed. Since the trace was phase-independent, no effects from the phase jumps were observed in the trace, thus allowing a high number of points per phase segment (~ 3000). This allows us to discard fewer points, thus enabling better convergence.

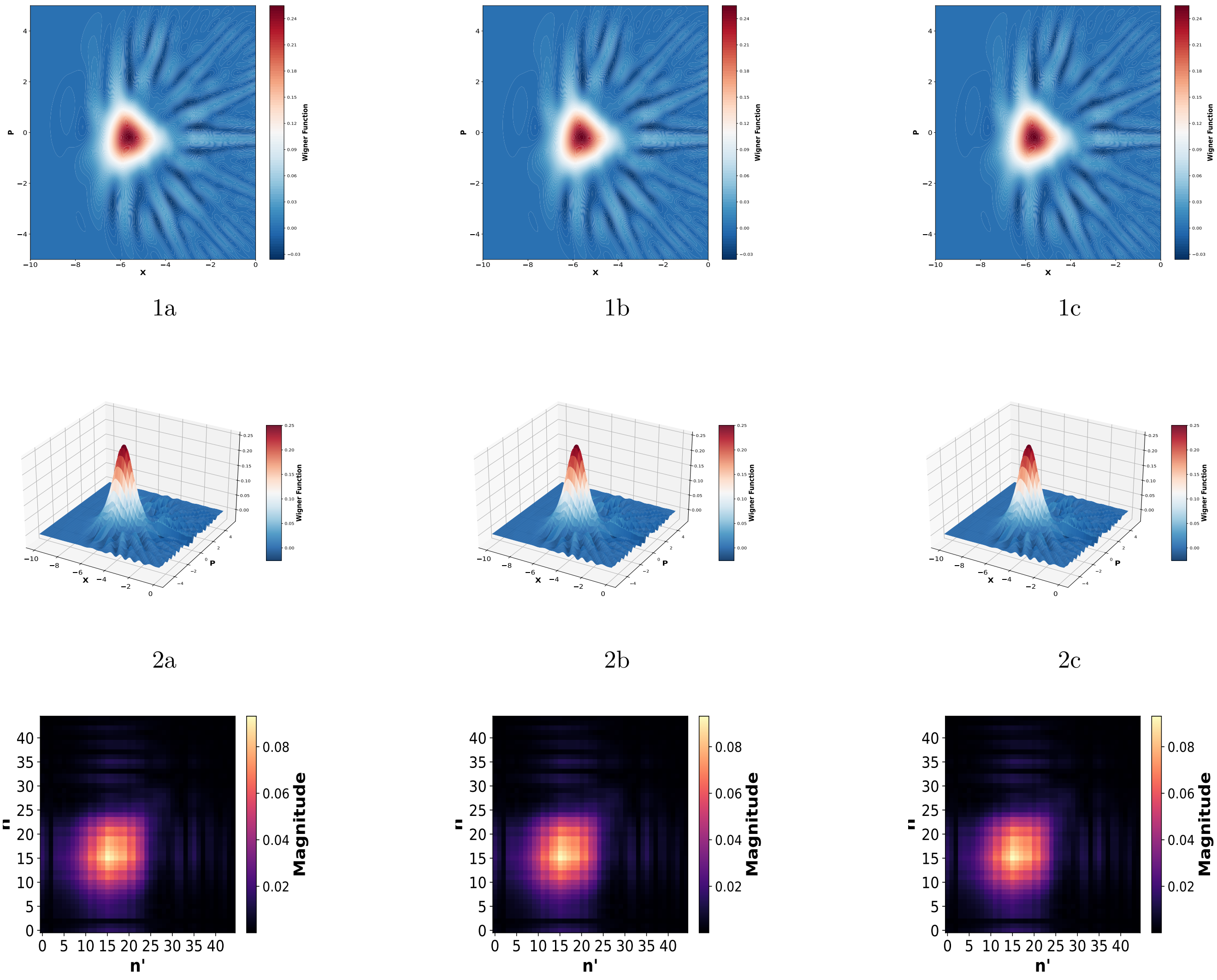

1a 1b 1c

2a 2b 2c

3a 3b 3c

Figure 5.21: In the image, the experimental Wigner function reconstructions are shown both from two-dimensional (1) and three-dimensional (2) perspectives, together with the corresponding density matrices (3) of three independents runs of the algorithm. The same dataset was used with 15 iterations. As can be seen, good convergence is observed, although some oscillations are present in the final representations, probably due to the limited number of points per phase (~ 1000).

Chapter 6

Conclusions and future works

In this work, the Wigner functions of a coherent and the vacuum state were reconstructed using two alternative methods: the Maximum Likelihood Estimation (MLE) technique [11] and the Inverse Radon Transform (IRT) approach [41], both from experimental and simulated data. While squeezed states and other non classical states were only achieved through ideal simulations. These results were obtained through a Balanced Homodyne Detection partially implemented in Polarization Maintaining fibres. In particular, the high stability of the used Local Oscillator (Teraxion TNL162630), which has a linewidth of 300 Hz, helped us during the experimental reconstructions.
Moreover, the same set-up has been used to retrieve the Wigner function of the state emitted by another source: a quantum well laser driven by a quiet pump current supply, that has shown sub-shot noise emission [15]. In this case, the reconstruction of the Wigner function was prevented by phase instabilities.
Indeed, this work shows that the phase diffusion is one of the main limiting factor for Wigner function reconstruction in phase space, requiring phase stability [7, 11]. Furthermore, by analysing realistic numerical simulations, the thesis provides both a quantitative and conceptual understanding of the experimental limitations that can corrupt the measurements in the IRT and MLE methods, only valid in specific circumstances [50]. This analysis is a necessary preliminary step toward the implementation of robust quantum tomography algorithms in future experiments and in CV-QKD protocols.

The phase drifting comes from the fact that in a real laser, spontaneous emissions occur alongside with stimulated ones, even if it remains the dominant mechanism. In particular, when a spontaneous emission occurs, the phase is not forced to be the same, therefore a small phase drifting is possible.
The new generated photon, with its drifted phase, can trigger further stimulated emissions, causing the overall phase of the laser output to diverge. Therefore, the first solution one can think is to lock the phase; this strategy is known as a Phase-Locked Loop (PLL) [51], and it is usually implemented by modulating the input current of the laser. However, changing the current statistics from which the laser is fed, prevents us to investigate whether the sub-shot noise statistic is related to squeezing. For not incur on this problem a Mach Zehnder Interferometer (MZI), able to record the instantaneous phase,

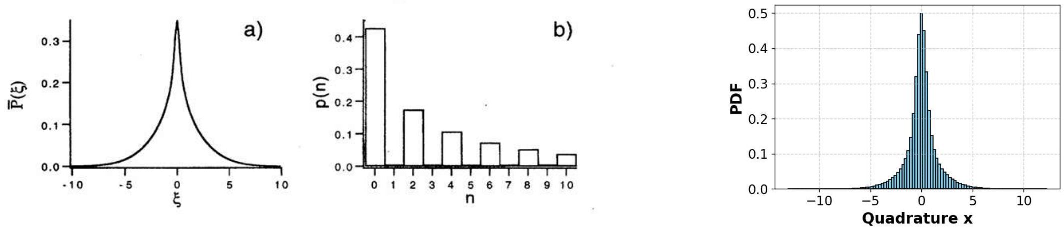

Figure 6.1: In the image above the achieved graphs from [55], both for the Photon statistic (a) and for the Photon distribution (b) are shown. As can be seen in that paper, the state of light was retrieved by simply looking at the photon distribution with a random phase. The simulated results are shown in the right figure, following a similar behaviour.

can be built. Then, the phase drifting, can be compensated by the usage of an EOM (Electro-Optic Modulator) or a fibre stretcher [52]. However, it has to be noted, that implementing a PLL is resource-demanding and challenging.
For such reason, alternative reconstruction strategies, that are not directly reconstructing the Wigner function, and do not rely on the phase stability, will be explored in the future.

These strategies were not implemented, mainly due to time constraints and the lack of specific equipment in the laboratory. However, they are well established techniques, already proven from experimental data.
One of those approaches rely on the photon number statistic [53, 54] that, as shown in Figure 5.10 depends on the measured quantum state. Similarly, the presence of squeezing can be proven looking at the quadrature measurement distribution when the phase is randomized [55]. Such reconstruction was performed in Figure 6.1, working with simulated data.

It is important to notice that, for the correct implementation of those techniques, a suitable detection bandwidth is necessary. Relying on this assumption, an additional procedure that could be explored is phase reorganization through the In-phase and in-Quadrature components. Indeed, in phase space, each slice corresponds to a specific

phase, allowing one to identify whether squeezing is present. In this case, the Husimi Q-function can be reconstructed; In particular, this function can be obtained by convolving the Wigner function with a Gaussian distribution [7].
As a result, negativities (quantum features) are lost, and fine details of the state, such as the amount of squeezing, are attenuated.

If, in addition, also a faster electronic is available, faster modulation schemes can represent a promising direction toward overcoming phase diffusion and enabling dynamic control of the quantum state. Indeed, one can beat the phase noise by repeating the experiment faster than the phase drifting. However, fast electronic, as faster FPGAs ($\sim$ 4GHz), are costly, difficult to be used and to be built.

Furthermore, they have limitations in the output voltage and in the rising time.

In conclusion, while the present work focuses on the reconstruction of coherent and vacuum states, it establishes the methodological and experimental foundations required for future measurements of non-classical states of light. Moreover, the presented analysis of phase diffusion and the limitations of the various tomographic algorithms constitute an important step toward the realization of advanced continuous-variable quantum optics experiments achieved using standard telecom equipment in our laboratory, useful for future applications.

Acknowledgement

I would like to express my deepest gratitude to my main supervisor in Telecom Paris, Prof. Frederic Grillot for his availability, guidance and continuous support, as well as his patience throughout this work.

I am also very grateful to my supervisor from Polytechnic of Turin Prof. Lorenzo Columbo for being always available and present even over the distance whenever necessary.

I am moreover very thankful to Prof. Juan Rafael Alvarez Velasquez, who constantly supported me during this work, providing the right motivation and invaluable advice with great willingness, and Prof. Huang Heming for his help in the laboratory whenever needed. Providing exhaustive information about all the devices.

Furthermore,I want to thank all the team in Telecom, especially Profs. Nicolas Fabre, Matteo Schiavon, Elie Awwad for providing new references and perspectives during this work. I am also grateful to Dr. Daniele Nello for achieving remarkable results with his simulations at the Polytechnic of Turin, and Dr. Guillame Richard and Dr. Shivang Srivastava for their help.

I would also like to thank my parents, my brother Manuel Battiston, and my grandma for their unconditional love and encouragement throughout my studies, and my partner Elias for his support, patience, and understanding during the long months of this work. My sincere thanks also go to all my colleagues and friends in the lab for creating a stimulating environment, for their collaboration, and for the many moments we shared, both scientific and personal, especially Thomas, Sergio, Sara, and Ornella. Finally, I truly appreciate the support of my italian friends, especially Roberto, Paolo, Noemi, Andrea and Coralie; I hope this bond will continue.

Lastly, I thank all those who, in various ways, have contributed to this journey.

Federico Battiston

Appendices

6.1

The Maxwell equations in vacuum (without any charge or current) can be written as follows:

$$\nabla \cdot \mathbf{E} = 0, \tag{6.1.1}$$

$$\nabla \cdot \mathbf{B} = 0, \tag{6.1.2}$$

$$\nabla \times \mathbf{E} = -\frac{\partial \mathbf{B}}{\partial t}, \tag{6.1.3}$$

$$\nabla \times \mathbf{B} = \mu_0 \varepsilon_0 \frac{\partial \mathbf{E}}{\partial t}. \tag{6.1.4}$$

Using those equations one can easily retrieve the wave equation [56]:

$$\nabla^2 \mathbf{E} - \frac{1}{c^2}\frac{\partial^2 \mathbf{E}}{\partial t^2} = 0 \tag{6.1.5}$$

where $c = 1/\sqrt{\mu_0 \varepsilon_0}$ is the speed of light in vacuum.
It is known that the vector potential is defined up to the gradient of a scalar function χ, so the choice of a gauge is required. The most commonly used gauge is the Coulomb one, where $(\nabla \cdot \mathbf{A} = 0)$, so:

$$\mathbf{E} = -\frac{\partial \mathbf{A}}{\partial t}, \qquad \mathbf{B} = \nabla \times \mathbf{A}. \tag{6.1.6}$$

Therefore the wave equation for $\mathbf{A}$ reads:

$$\nabla^2 \mathbf{A} - \frac{1}{c^2}\frac{\partial^2 \mathbf{A}}{\partial t^2} = 0. \tag{6.1.7}$$

Expanding $\mathbf{A}(\mathbf{r}, t)$ with the Fourier expansion one has:

$$\mathbf{A}(\mathbf{r}, t) = \sum_{\mathbf{k},\lambda} \left[a_{\mathbf{k},\lambda}(t)\, \boldsymbol{\epsilon}_{\mathbf{k},\lambda} e^{i\mathbf{k}\cdot\mathbf{r}} + \text{c.c.} \right], \tag{6.1.8}$$

where $\boldsymbol{\epsilon}_{\mathbf{k},\lambda}$ are the transverse polarization vectors.
Substituting this into the wave equation leads to:

$$\ddot{a}_{\mathbf{k},\lambda}(t) + \omega_k^2 a_{\mathbf{k},\lambda}(t) = 0, \tag{6.1.9}$$

which is the classical equation of motion of a harmonic oscillator of frequency $\omega_k = c|\mathbf{k}|$. Therefore, each mode of the field behaves like a classical harmonic oscillator.
After the second quantization, the value $a_{\mathbf{k},\lambda}(t)$ becomes operators satisfying canonical commutation relations:

$$\left[\hat{a}_{\mathbf{k},\lambda}, \hat{a}^{\dagger}_{\mathbf{k}',\lambda'}\right] = \delta_{\mathbf{k},\mathbf{k}'}\delta_{\lambda,\lambda'}, \tag{6.1.10}$$

and the Hamiltonian of the electromagnetic field becomes:

$$\hat{H} = \sum_{\mathbf{k},\lambda} \hbar\omega_k \left(\hat{a}^{\dagger}_{\mathbf{k},\lambda}\hat{a}_{\mathbf{k},\lambda} + \frac{1}{2}\right). \tag{6.1.11}$$

6.2

In this Appendix the general equation that describes a wavefunction in the Fock space is derived.
By solving the eigenvalue equation:

$$\hat{H}\left|\psi_n\right\rangle = E_n\left|\psi_n\right\rangle \tag{6.2.1}$$

where $\hat{H}$ is the Hamiltonian operator one can obtain the following differential equation [7]:

$$\frac{1}{2}(-\frac{\partial^2}{\partial X^2} + X^2)\left|\psi_n\right\rangle = E_n\left|\psi_n\right\rangle \tag{6.2.2}$$

Moreover, from the results of the harmonic oscillator it is well established that the energies have to be quantized (discrete values instead of a continuum as in the classical formalism) and that the wavefunction are vanishing for large value of X. Thus the wavefunction $\left|\psi_n\right\rangle$ reads:

$$\left|\psi_n\right\rangle = N_n P_n e^{-x^2/2} \tag{6.2.3}$$

where N_n is a normalization constant.
The P_n are polynomials, coming from the requisite to ensure that the Sturm Liouville principle is valid, needed for the discreteness of the E_n eigenvalues [57,58].
By taking the second derivative of the previously defined wavefunction one can achieve:

$$\ddot{\psi}_n = [\ddot{P}_n(x) - 2xP_n + (x^2-1)P_n]e^{-\frac{x^2}{2}}, \tag{6.2.4}$$

$$-\frac{1}{2}[\ddot{P}_n(x) - 2xP_n + (x^2-1)P_n]e^{-\frac{x^2}{2}}, = E_n e^{-\frac{x^2}{2}}. \tag{6.2.5}$$

By simplifying the exponential one can finally achieve the final equation

$$\ddot{P}_n - 2X P_n + 2(E_n - \frac{1}{2})P_n = 0, \tag{6.2.6}$$

with

$$H_n(X) = (-1)^n e^{X^2} \frac{d^n}{dx^n}\left(e^{-X^2}\right). \tag{6.2.7}$$

being the Hermite polynomials.
Following the Born principle the wavefunction has to be normalized to one, since it is related to the probability to find the particle in the space ($\int_{\mathbb{R}} |\psi|^2 = 1$).
Finally one has to identify the normalizing constant N_n ensuring:

$$\int_R \psi_n \psi_n^* = \int_R |\psi|^2 = 1 \tag{6.2.8}$$

Since the Hermite polynomials are guaranteed orthonormal [59], this normalization constant is evaluated as:

$$N_n = \frac{1}{\sqrt[4]{\pi}\sqrt{2^n n!}} \tag{6.2.9}$$

One can see that for $n = 0$ this wavefunction exactly converges to the vacuum one, derived in Appendix 6.3, proving the effectiveness of the obtained formula.

6.3

In this Appendix, the vacuum state wavefunction is derived. This result is a particular case of the more general outcome presented in Appendix 6.2.
However, it is instructive, as it allows us to obtain a specific result by starting from the physical properties of the state.
One equation underlining the properties of vacuum is the annihilation boundary condition presented in 2.1.22. Indeed:

$$\hat{a}\psi_0 = \frac{1}{\sqrt{2}}(\hat{X} + i\hat{P})\psi_0 = \frac{1}{\sqrt{2}}(\hat{X} + \frac{\partial}{\partial X})\psi_0 = 0 \tag{6.3.1}$$

where ψ_0 is the vacuum wavefunction and the mathematical definition of $\hat{P} = -i\frac{\partial}{\partial X}$ was used.

This is a separable differential equation solved by:

$$\ln(\psi_0) = \frac{-X^2}{2} + C \implies \psi_0 = Ae^{-\frac{X^2}{2}} \tag{6.3.2}$$

being C and $A = e^C$ constants. Again, the canonical procedure in order to evaluate the normalization constant A is to use the Born rule. Thus to impose that the probability has to converge to 1 in the whole space:

$$\int_{-\infty}^{+\infty} \psi\psi^* = \int_{-\infty}^{+\infty} |A|^2 e^{-q^2} = |A|^2\sqrt{\pi} = 1 \tag{6.3.3}$$

where the calculation was done in one dimension for simplicity (but could be expanded in the three-dimensional one by considering π^3 instead of π).
Then

$$|A| = \frac{1}{\sqrt[4]{\pi}}, \tag{6.3.4}$$

thus

$$|0\rangle = \frac{1}{\sqrt[4]{\pi}} e^{-\frac{X^2}{2}}, \tag{6.3.5}$$

as shown in 2.2.6. In particular one can now estimate the variance and the mean value of the vacuum state as:

$$Var(\psi_0) = \langle X^2 \rangle - \langle X \rangle^2 = \langle 0| \hat{X}^2 |0\rangle - \langle 0| \hat{X} |0\rangle, \tag{6.3.6}$$

$$E(\psi_0) = \langle X \rangle = \langle 0| \hat{X} |0\rangle. \tag{6.3.7}$$

By Recalling that $\langle X \rangle = \int_{\mathbb{R}} X|\psi_0|^2 dX = 0$ (since X it is an odd function) when integrated in the whole space, and that $< X^2 >= \int_{\mathbb{R}} X^2|\psi_0|^2 dX = \frac{1}{2}$, one is able to achieve that:

$$Var(\psi_0) = \frac{1}{2} \tag{6.3.8}$$

$$E(\psi_0) = 0 \tag{6.3.9}$$

While the quadrature formalism can feel somewhat abstract, the vacuum wavefunction gains a more *intuitive meaning* when expressed in terms of the canonical position $\hat{x}$ and momentum $\hat{p}$ operators. In this representation, the vacuum state is simply the *ground state of the quantum harmonic oscillator.* Its Gaussian form reflects minimal uncertainty: the state has the lowest possible energy and saturates the Heisenberg uncertainty relation, just like the first quantized energy level of a one-dimensional harmonic oscillator.

6.4

In this Appendix the coherent state wavefunction is derived. The coherent state is defined as the eigenvalue of the annihilation operator, therefore:

$$
\begin{aligned}
|\alpha\rangle &= \hat{D}(\alpha)\,|0\rangle & (6.4.1)\\
&= e^{\alpha\hat{a}^\dagger - \alpha^*\hat{a}}\,|0\rangle\,, & (6.4.2)
\end{aligned}
$$

where the definition of the Displacement operator $\hat{D}(\alpha)$ was used.
Since $\hat{a}$ and $\hat{a}^\dagger$ do not commute, the Baker-Campbell-Hausdorff formula must be applied. Namely let $\mathcal{A}$ and $\mathcal{B}$ two operators, then:

$$
e^{\mathcal{A}+\mathcal{B}} = e^{-\frac{1}{2}[\mathcal{A},\mathcal{B}]}e^{\mathcal{A}}e^{\mathcal{B}}, \tag{6.4.3}
$$

where $[\cdots]$ identifies the commutator.
Moreover, since:

$$
[\alpha\hat{a}^\dagger, -\alpha^*\hat{a}] = -|\alpha|^2[\hat{a},\hat{a}^\dagger] = |\alpha|^2, \tag{6.4.4}
$$

using the Taylor expanction:

$$
e^{-\alpha a}\,|0\rangle = \sum_{n=-\infty}^{\infty}\frac{(-\alpha)^n}{n!}\hat{a}^n\,|0\rangle = 0. \tag{6.4.5}
$$

Therefore the wavefunction reads:

$$
\begin{aligned}
|\alpha\rangle &= e^{-\frac{|\alpha|^2}{2}}e^{\alpha\hat{a}^\dagger}\,|0\rangle & (6.4.6)\\
&= e^{-\frac{|\alpha|^2}{2}}\sum_{n=0}^{\infty}\frac{\alpha^n}{n!}\hat{a}^{\dagger n}\,|0\rangle & (6.4.7)\\
&= e^{-\frac{|\alpha|^2}{2}}\sum_{n=0}^{\infty}\frac{\alpha^n}{n!}\sqrt{n!}\,|n\rangle & (6.4.8)\\
&= \sum_{n=0}^{\infty}e^{-\frac{|\alpha|^2}{2}}\frac{\alpha^n}{\sqrt{n!}}\,|n\rangle\,. & (6.4.9)
\end{aligned}
$$

This is indeed the coherent state representation in the Fock basis. It is clear that this state is expressed as an infinite superposition of Fock states $|n\rangle$. This implies that a truncation (thus an approximation) is needed while observing those states.

6.5

In this Appendix the noise properties (standard deviations) of the squeezed states are derived. This information will be crucial for the correct understanding of these states. Recalling that the quadrature operators are defined as:

$$\hat{X} = \frac{\hat{a} + \hat{a}^\dagger}{\sqrt{2}} \tag{6.5.1}$$

$$\hat{P} = \frac{\hat{a} - \hat{a}^\dagger}{\sqrt{2}i} \tag{6.5.2}$$

where $\hbar$ was set to one, and by using the vacuum wavefunction derived in Appendix 6.3, it is possible to define the squeezed wavefunction as [7]:

$$|\psi_r(x)\rangle = \langle x|\psi_r\rangle = e^{\frac{r}{2}}\psi_0(e^r x), \tag{6.5.3}$$

where r is a real coefficient, known as squeezing parameter.
The variance of the state is then defined as:

$$\langle \Delta X\rangle = \langle X^2\rangle - \langle X\rangle^2. \tag{6.5.4}$$

Considering the previous defined ψ_r, one can define the mean value of the quadrature $\hat{X}$ as:

$$\langle X\rangle_r = \int_{\mathbb{R}} x|\psi_r(x)|^2 dx = e^{-r}\int_{\mathbb{R}} u|\psi_0(u)|^2 du = e^{-r}\langle X\rangle_0 = 0, \tag{6.5.5}$$

where x was substituted to X inside the integration and the change of variable $xe^r = u$ was used.
Since the squeezing was associated to the vacuum state in the previous reasoning, one expects a vanishing mean value of the squeezed state is 0: in agreement with what obtained.
On the other hand:

$$\langle X^2\rangle_r = \int_{\mathbb{R}} x^2|\psi_r(x)|^2 dx = e^{-2r}\int_{\mathbb{R}} u^2|\psi_0(u)|^2 du = e^{-2r}\langle X^2\rangle_0 = \frac{e^{-2r}}{2} \tag{6.5.6}$$

This leads to the well established results:

$$\langle \Delta X^2\rangle = \frac{e^{2r}}{2} \tag{6.5.7}$$

$$\langle \Delta P^2\rangle = \frac{e^{-2r}}{2}, \tag{6.5.8}$$

where the result for the $\hat{P}$ quadrature could be obtained by following the same reasoning with this operator. It is clear in the previous equations that the variance properties are *anti*-correlated: if one quadrature assumes an higher than vacuum variance, then the variance on the other must diminish. This property, typical of squeezed states, can be summarized by noticing that squeezed states are minimum uncertainty states, as proven in Appendix 6.6.

6.6

In this Appendix, it is formally derived the condition for a minimum uncertainty state; i.e. a state that *saturate* the Heisenberg uncertainty relation:

$$\Delta X\,\Delta P = \frac{1}{4}. \tag{6.6.1}$$

Such states are particularly important because they allow one to minimize noise in one quadrature while controlling the other. Examples include the vacuum and coherent. Let us introduce the operator

$$\hat{A} = \Delta\hat{X} + i\lambda\,\Delta\hat{P}, \qquad \lambda \in \mathbb{R}, \tag{6.6.2}$$

where

$$\Delta\hat{X} = \hat{X} - \langle\hat{X}\rangle, \qquad \Delta\hat{P} = \hat{P} - \langle\hat{P}\rangle. \tag{6.6.3}$$

By construction, for any quantum state $|\psi\rangle$:

$$\langle\hat{A}^\dagger\hat{A}\rangle \geq 0. \tag{6.6.4}$$

Indeed:

$$\begin{aligned}
\hat{A}^\dagger\hat{A} &= (\Delta\hat{X} - i\lambda\Delta\hat{P})(\Delta\hat{X} + i\lambda\Delta\hat{P}) && (6.6.5)\\
&= (\Delta\hat{X})^2 + \lambda^2(\Delta\hat{P})^2 + i\lambda[\Delta\hat{X},\Delta\hat{P}] && (6.6.6)\\
&= (\Delta\hat{X})^2 + \lambda^2(\Delta\hat{P})^2 - \lambda, && (6.6.7)
\end{aligned}$$

where we used $[\hat{X},\hat{P}] = i$.

It can be proven that a state $|\psi\rangle$ minimizes the uncertainty if [58]:

$$\langle\hat{A}^\dagger\hat{A}\rangle = 0. \tag{6.6.8}$$

This implies

$$(\Delta X)^2 + \lambda^2(\Delta P)^2 - \lambda = 0. \tag{6.6.9}$$

Therefore:

$$\lambda = \frac{1}{2(\Delta P)^2}. \tag{6.6.10}$$

Substituting back, one finds the Heisenberg equality:

$$\Delta X \, \Delta P = \frac{1}{4}. \tag{6.6.11}$$

In the X-representation ($\hat{P} = -i\frac{\partial}{\partial X}$), the condition

$$\hat{A}\psi(X) = (\Delta X + i\lambda\Delta P)\psi(X) = 0 \tag{6.6.12}$$

becomes the differential equation:

$$(X - X_0 + \lambda\frac{\partial}{\partial X})\psi(X) = 0, \tag{6.6.13}$$

where $X_0 = \langle \hat{X} \rangle$ and $\hbar = 1$.
Solving this first-order differential equation gives a Gaussian wavefunction:

$$\psi(X) = A \exp\left[-\frac{(X - X_0)^2}{2\lambda} + iP_0(X - X_0) \right], \tag{6.6.14}$$

where $P_0 = \langle \hat{P} \rangle$ and A is the normalization constant.
For instance the vacuum state: $X_0 = P_0 = 0$, $\lambda = 1$ ($\hbar = 1$), we recover

$$\psi_0(X) = Ae^{-X^2/2}, \tag{6.6.15}$$

in agreement with Appendix 6.3.
Thus the states that minimize the Heisenberg uncertainty principle has to be Gaussian states, hence vacuum, coherent and squeezed states.
In particular for a coherent state, X_0 and P_0 shift the Gaussian centre while for a squeezed state, $\lambda \neq 1$ compresses one quadrature and stretches the other, maintaining $\Delta X \, \Delta P = 1/2$.
Hence, all these states are minimum uncertainty states, with Gaussian wavefunctions determined by λ and the expectation values (X_0, P_0).

6.7

In this Appendix it is proven that the conjugate quadratures $\hat{X}$ and $\hat{P}$ are linked by a Fourier transform.
Let us start by identifying their eigenvalue equations:

$$\hat{X} \left| X \right\rangle = x \left| X \right\rangle \tag{6.7.1}$$

$$\hat{P} \left| P \right\rangle = p \left| P \right\rangle, \tag{6.7.2}$$

where here x and p identifies the associated eigenvalues.
Therefore the product $\langle X| \hat{P} |P\rangle$ can be written as:

$$\langle X| \hat{P} |P\rangle = p \langle X|P\rangle = p f_P(X) \tag{6.7.3}$$

where the quantity $f_P(q) = \langle X|P\rangle$ was defined.
However $\hat{P}$ is $\hat{P} = -i\frac{\partial}{\partial X}$ if $\hbar = 1$ that, for consistency, has to be the previously defined value p.
By solving the differential equation one finds:

$$-i\frac{\partial}{\partial X} f_P(X) = p f_P(X) \implies \tag{6.7.4}$$

$$f_P(X) = A e^{iPX}. \tag{6.7.5}$$

However $\hat{P}$ and $\hat{X}$ have to be orthonormal and, since the two operators live in the infinite dimension space, the common practice is to impose:

$$\langle P|P'\rangle = \delta(P - P') \tag{6.7.6}$$

On the other hand:

$$\langle P|P'\rangle = \int_{\mathbb{R}} \langle X|P\rangle \langle X|P'\rangle \, dX \tag{6.7.7}$$

$$= \int_{\mathbb{R}} f_P(X) f^*_{P'}(X) \, dX \tag{6.7.8}$$

$$= AA^* \int_{\mathbb{R}} e^{iX(P-P')} \, dX \tag{6.7.9}$$

$$= |A|^2 2\pi \, \delta(P - P'), \tag{6.7.10}$$

where the identity was written as $\mathbb{I} = \int_{\mathbb{R}} |X\rangle \langle X|$ and the definition with the properties of the delta and its Fourier transform was used [60]. By then using both eq 6.7.10 and eq 6.7.6, the final form of $f_P(X)$ can be achieved:

$$f_P(X) = \langle X|P\rangle = \frac{1}{\sqrt{2\pi}} e^{iXP} \tag{6.7.11}$$

that is indeed the change of basis due to the Fourier transform, proving that the $\hat{P}$ operator is indeed the Fourier transform of the $\hat{Q}$ momenta. This result can also be understood intuitively by noting that $|X\rangle$ and $|P\rangle$ form a pair of dual bases, with $|P\rangle$ representing plane-wave states in the $\hat{X}$ representation [7].

6.8

This Appendix is divided into two parts: first, the minimum number of iterations required for a tomographic algorithm is derived; second, a suitable set of projectors for tomographic measurements is introduced.

Minimum number of iterations : First of all, a generic density matrix $\hat{\rho} \in \mathbb{C}^{d \otimes d}$ must satisfy the following conditions:

i **Hermiticity:** $\hat{\rho} = \hat{\rho}^\dagger$;

ii **Semi-positive definite:** $\langle \psi | \hat{\rho} | \psi \rangle \geq 0$;

iii **Trace unitarity:** $\sum_i \rho_{ii} = 1$.

The total number of parameters of such density matrix is $d \otimes d = d^2$, and only d of them correspond to the diagonal elements.
Hence, the number of off-diagonal elements is

$$d^2 - d = d(d-1), \tag{6.8.1}$$

and these must be independent.
According to property iii, once all the diagonal elements are known, the remaining one is determined.
Thus, the total number of free parameters in a d-dimensional density matrix is

$$d(d-1) + (d-1) \sim d^2 \tag{6.8.2}$$

for large d.
Using the Frobenius norm [61],

$$\|\rho\|_F = \sqrt{\sum_{i=1}^{m} \sum_{j=1}^{n} |\rho_{ij}|^2} = \sqrt{\mathrm{Tr}(\rho\rho^\dagger)}, \tag{6.8.3}$$

the corresponding error norm is

$$||\Delta\rho||_F = \sqrt{\mathrm{Tr}(\Delta\rho\Delta\rho^\dagger)}. \tag{6.8.4}$$

If p is the total number of free parameters and ϵ the acceptable error per parameter, then

$$||\Delta\rho||_F = \delta = \epsilon\sqrt{p} \implies \epsilon = \frac{\delta}{\sqrt{p}}, \tag{6.8.5}$$

where δ represents the total matrix error.
According to the law of large numbers, given n measurements, the statistical error decreases as $\sim 1/\sqrt{n}$.

In a generic density matrix, there are $\sim d^2$ free elements. If an error ϵ is acceptable for each element (assuming all errors are equal), the total number of measurements required scales as

$$n \sim \frac{d^2}{\epsilon^2}. \tag{6.8.6}$$

On the other hand, if $\hat{\rho}$ represents a pure state ($\hat{\rho} = |\psi\rangle \langle\psi|$), or if only the diagonal elements are relevant, it can be shown that the number of independent parameters reduces to $\sim d$. In this particular case, the required number of measurements decreases quadratically:

$$n \sim \frac{d}{\epsilon^2}, \tag{6.8.7}$$

and the setup can be simplified to a single basis measurement, since all cross-diagonal elements vanish.
Moreover, as the number of measurements increases, the total error distribution approaches a Gaussian shape, in accordance with the Central Limit Theorem. The standard deviation scales as $\sigma \propto 1/\sqrt{N}$, where N is the number of measurements. Thus, the higher the number of measurements, the smaller the total reconstruction error.

Choice of the projectors : A suitable set of projectors must be defined in order to span the entire Hilbert space. For simplicity, consider the case of a qubit, whose state is completely determined by the Pauli operators $\hat{X}, \hat{Y}, \hat{Z}$. A generic qubit state can be expressed as [62]:

$$\rho = \frac{1}{2}\Big(\operatorname{tr}(\rho)I + \operatorname{tr}(X\rho)X + \operatorname{tr}(Y\rho)Y + \operatorname{tr}(Z\rho)Z\Big), \tag{6.8.8}$$

where $\operatorname{Tr}(A\rho) = \operatorname{Tr}(\rho A)$ represents the expectation value of the observable A in the state ρ. By repeating each measurement a sufficiently large number of times, one obtains a set of experimental values $p_{A,i}(\rho)$ defining a probability distribution.
As the number of repetitions increases, these values converge to the true probability $p_A(\rho)$, allowing the estimation of expectation values by averaging the measurement outcomes.
The qubit case can be generalized beyond the concept of a finite-dimensional Hamel basis. In continuous-variable quantum systems, the relevant observable is the quadrature operator $\hat{X}_\theta$, belonging to an infinite-dimensional Hilbert space. In this case, one must define an appropriate set of POVMs (Positive Operator-Valued Measures) corresponding to projections along different quadratures. These POVMs allow measurement of the quantity

$$\mathcal{E}(\rho) = \sum_{nm} E_n \rho E_m^\dagger, \tag{6.8.9}$$

where $\mathcal{E}$ denotes the quantum channel probing the state ρ, and $\{E_n\}$ are the POVM elements, which can be expressed as [3]

$$E_n = \sum_i h_{in} \tilde{E}_i, \tag{6.8.10}$$

with $\{\tilde{E}_i\}$ forming a suitable set of projection operators. Thus, the overall transformation can be rewritten as:

$$\mathcal{E}(\rho) = \sum_{nm} \tilde{E}_n \rho \tilde{E_m} \chi_{nm}, \tag{6.8.11}$$

where χ_{nm} is a Hermitian matrix defined as $\chi_{nm} = h_{in} h^*_{im}$. The coefficients of χ can be numerically reconstructed since $\mathcal{E}(\rho)$ is experimentally accessible [3].
In general, the POVM elements $\{\tilde{E}_i\}$ are not individual vectors, but rather rank-one projectors onto pure states.
The goal is to identify a basis in which the state can be expressed as a linear combination of these projectors, thereby enabling the reconstruction of the density matrix ρ. This reconstruction process is closely related to the Choi–Jamiołkowski isomorphism [63].
Consider a generic pure state $|v\rangle$ in the Hilbert space $\mathbb{C}^d$. Each complex vector has $2d$ real parameters, and the normalization condition $\langle v|v\rangle = 1$ removes one degree of freedom. Hence, $|v\rangle$ corresponds to a point on the hypersphere $S^{2d-1} = \{v \in \mathbb{C}^d : \|v\| = 1\}$. We can express $|v\rangle$ as a column of a unitary matrix U, for instance $|v\rangle = Ue_1$, where $e_1 = [1,0,0,\ldots,0]^T$ is the first basis vector of the identity matrix. Within the unitary group $U(d)$, there exists a unique invariant measure μ, known as the Haar measure, which assigns a uniform volume to the group [64].
Hence, every pure state $|v\rangle \in \mathbb{C}^d$ (representing a quadrature projector) can be viewed as a point on the hypersphere S^{2d-1}. Physically, this means that every possible pure quantum state corresponds to a unique point on this high-dimensional sphere, and the Haar measure formalizes uniform sampling over all such states. In practice, this corresponds to performing quadrature measurements $\hat{X}_\theta$ for many different phases θ, uniformly sampled over $\theta \in [0, \pi]$. This is the continuous-variable analogue of sampling uniformly over the unitary group $U(d)$.

6.9

In this Appendix the connection between the Wigner function W and the density operator is shown.
The Inverse Radon Transform $\mathcal{R}^{-1}$ allows us to reconstruct the Wigner function from the measured quadrature distributions, which are the experimentally accessible quantities. To see this explicitly, we start with the definition of the Fourier transform of the Wigner function.
In this Appendix, the quadratures $\hat{X}$ and $\hat{P}$ will be denoted as $\hat{q}$ and $\hat{p}$, following the standard convention in quantum mechanics. This change of notation ensures

consistency with the literature and references, without altering the physical meaning of the discussion.

$$\mathcal{F}(W) = \chi(u,v) = \int W(q,p)e^{-i(uq+vp)}dqdp. \tag{6.9.1}$$

That is a known function called characteristic function.
Going back to the probabilities that one observes in the experiment, one has that their Fourier transform is

$$\tilde{P}_\theta(k) = \int P_\theta(q)e^{-ikq}dq \tag{6.9.2}$$

However, by definition, since the P_θ are the probabilities and W the Wigner function:

$$\tilde{P}_\theta(k) = \int_{\mathbb{R}} P_\theta(q)e^{-ikq}dq = \int_{\mathbb{R}}\int_{\mathbb{R}} W(q',p')e^{-ikq}dqdp, \tag{6.9.3}$$

where, following the previous definition of the Wigner function depending on θ given in equation 2.3.7, the quantities q' and p' are defined as

$$\begin{aligned} q' &= q_\theta = q\cos(\theta) + p\sin(\theta) \\ p' &= p_\theta = q\sin(\theta) + p\cos(\theta). \end{aligned}$$

Then by calling

$$u = k\cos(\theta) \qquad\qquad v = k\sin(\theta).$$

The quantity kq_θ becomes

$$kq_\theta = uq + vp \tag{6.9.4}$$

So

$$\begin{aligned} \tilde{P}_\theta(k) &= \int\int W(q,p)e^{-i(uq+vp)}dpdq \\ &= \chi(u,v) = \chi(k\cos(\theta), k\sin(\theta)). \end{aligned} \tag{6.9.5}$$

However, since the goal is to find out the Inverse Radon Transform $\mathcal{R}^{-1}$, then the Inverse Fourier transform has to be applied, so:

$$W(q,p) = \frac{1}{2\pi}\int\int \chi(u,v)e^{-i(uq+vp)}dudv, \tag{6.9.6}$$

However the characteristic function can always be seen as the expected value of the complex exponential of the random variable that, in our case, is the operator:

$$\chi_X(t) = \mathbb{E}(e^{itX}) \qquad X \quad \text{r.v.} \quad ,t \in \mathbb{R} \tag{6.9.7}$$

since in quantum mechanics the expected value is replaced by the trace one has that

$$\chi(u,v) = Tr[\hat{\rho}e^{-i(uq+vp)}] = \int_{\mathbb{R}} dx \quad \langle x|\,\hat{\rho}e^{-i(uq+vp)}\,|x\rangle\,, \tag{6.9.8}$$

where the identity relation $\int_{\mathbb{R}} |x\rangle\langle x| = \mathbb{I}$ was used. The exponential can be further simplified using the Baker–Campbell–Hausdorff formula (BCH) [65]. And in the particular case of Glauber the formula simplifies to:

$$e^{X+Y} = e^X e^Y e^{-\frac{1}{2}[X,Y]}, \tag{6.9.9}$$

if $[X,[X,Y]] = [Y,[Y,X]] = 0$ that is our case since $[X,Y] = const$.
So the action of the complete exponential operator can be proven be simply a shifting in $|x\rangle$ and a phase shifting; To see this one can use the Baker's formula that states that

$$e^A B e^{-A} = B + [A,B] + \frac{1}{2!}[A,[A,B]] + \cdots \tag{6.9.10}$$

since the commutator between $\hat{q}$ and $\hat{p}$ is constant, one can write that:

$$\langle x| e^{-iv\hat{p}} |x\rangle = \langle x|x+v\rangle = \delta(v) \tag{6.9.11}$$

For the $\hat{q}$ exponential the same reasoning can be done resulting in a simple phase shift; then

$$\begin{aligned} W(q,p) &= \frac{1}{2\pi}\int\int \chi(u,v) e^{-i(uq+vp)}\, du\, dv \\ &= \frac{1}{2\pi}\int\int \mathrm{Tr}[\hat{\rho}\, e^{-i(u\hat{q}+v\hat{p})}]\, du\, dv \\ &= \frac{1}{2\pi}\int\int \langle x|\,\hat{\rho}\, e^{-i(u\hat{q}+v\hat{p})}\,|x\rangle\; du\, dv \\ &= \frac{1}{2\pi}\int\int e^{-iux}\,\langle x|\,\hat{\rho}\, e^{-iv\hat{p}}\,|x\rangle\; du\, dv \\ &= \frac{1}{2\pi}\int\int e^{-iux}\,\langle x|\,\hat{\rho}\,|x+v\rangle\; du\, dv \\ &= \frac{1}{2\pi}\int dv\, e^{ivp}\,\langle q-\frac{v}{2}|\,\hat{\rho}\,|q+\frac{v}{2}\rangle\,. \end{aligned} \tag{6.9.12}$$

that is the celebrated Wigner formula found in [7,66].

6.10

In this Appendix, we illustrate the mathematical working principle of the Inverse Radon Transform.
Let us start with the probability distribution $p_\theta(s)$ that is defined as the *probability distribution of the field for a given angle* θ.

Define then the two-dimensional Fourier transform (2D-FFT) and its inverse as the generalized two-variable version of the one dimensional one ($\mathcal{F}_{1D}$):

$$\mathcal{F}(k_x, k_y) = \mathcal{F}_{2D}\{f(x,y)\} = \int\int f(x,y)e^{-i(k_x x + k_y y)}dxdy \tag{6.10.1}$$

$$f(x,y) = \mathcal{F}_{2D}^{-1}\{\mathcal{F}(x,y)\} = \int\int \mathcal{F}(k_x, k_y)e^{i(k_x x + k_y y)}dk_x dk_y \tag{6.10.2}$$

The projection for a given angle θ is then given by:

$$p_\theta(s) = \int_{\mathbb{R}^2} f(x,y)\delta(s - x\cos(\theta) - y\sin(\theta))dxdy \tag{6.10.3}$$

where $f(x,y)$ is simply the image function that one wants to represent.
Whereas δ is simply accounting for the radial *slices* of this function for a given θ.
Taking the Fourier transform of this function one has that:

$$\begin{aligned} \tilde{p}_\theta(\omega) &= \int_{\mathbb{R}} p_\theta(s)e^{-i\omega s}ds \\ &= \int_{\mathbb{R}} f(x,y)\left[\int_{\mathbb{R}} e^{-i\omega s}\delta(s - x\cos\theta - y\sin\theta)\right]dxdy \\ &= \int_{\mathbb{R}}\int_{\mathbb{R}} f(x,y)e^{-i\omega(x\cos\theta + y\sin\theta)}dxdy, \end{aligned} \tag{6.10.4}$$

where the basic property

$$\int_{\mathbb{R}} \delta(x-a)f(x)dx = f(a) \tag{6.10.5}$$

was used, setting $f(x) = e^{-i\omega s}$.
However formula 6.10.4 is the definition of the two dimensional Fourier transform given in 6.10.1.
So:

$$\tilde{p}_\theta(\omega) = \mathcal{F}_{2D}\{p\}(\omega\cos\theta, \omega\sin\theta). \tag{6.10.6}$$

Then:

$$f(x,y) = \frac{1}{(2\pi)^2}\int_{\mathbb{R}^2} \mathcal{F}(k_x, k_y)e^{i(k_x x + k_y y)}dk_x dk_y \tag{6.10.7}$$

and by using $\rho = \omega$ one can write the above integral in polar coordinates, by imposing:

$$\begin{cases} k_x = \rho\cos\theta \\ k_y = \rho\sin\theta, \end{cases} = \begin{cases} k_x = \omega\cos\theta \\ k_y = \omega\sin\theta, \end{cases} \tag{6.10.8}$$

with $\rho \geq 0$ and $\theta \in [0, 2\pi)$.
Thus:

$$f(x,y) = \frac{1}{(2\pi)^2}\int_0^\pi \int_{-\infty}^{\infty} F(\omega\cos\theta, \omega\sin\theta)e^{i\omega(x\cos\theta + y\sin\theta)}|\omega|d\omega d\theta, \tag{6.10.9}$$

where the celebrated two dimensional polar Jacobian

$$J = \det\begin{bmatrix} \partial_\rho x & \partial_\theta x \\ \partial_\rho y & \partial_\theta y \end{bmatrix} = \rho(\cos^2\theta + \sin^2\theta) = \rho \tag{6.10.10}$$

was used.
Here the Fourier Slicing Theorem [67] was used, with P_1 projection operator identified with $p_\theta(s)$ and S_1 slicing operator identified by the F function.
Finally the celebrated formula will be [11]:

$$\begin{aligned} f(x,y) &= \frac{1}{(2\pi)^2}\int_0^\pi \int_{\mathbb{R}} \tilde{p}_\theta(s)|\omega|e^{i\omega s}d\omega ds \\ &= \frac{1}{(2\pi)^2}\int_0^\pi q_\theta(x\cos\theta, y\sin\theta)d\theta, \end{aligned} \tag{6.10.11}$$

with $s = x\cos\theta + y\sin\theta$ and $q_\theta(x\cos\theta, y\sin\theta) = \int_{\mathbb{R}} \tilde{p}_\theta(s)|\omega|e^{i\omega s}d\omega$, coherently with the theory.
This is exactly the mathematical definition of the filtered backprojection since the inverse Fourier transform is applied to the projection p_θ that is filtered by $|\omega|$.

6.11

It was shown in Appendix 6.10 that the IRT has to be understood with the concept of *filtered* backprojection. One might then wonder whether other filters are present and what their effect is.
In this Appendix the action of the filter inside the IRT is explored with its non idealities. The application of a filter with transfer function $H(\omega)$ is particularly easy in the frequency domain where the final transformation $\tilde{q}_\theta(\omega)$ is simply given by:

$$\tilde{q}_\theta(\omega) = H(\omega)\tilde{p}_\theta(\omega) \tag{6.11.1}$$

where the p_θ function is the one used in Appendix 6.10; thus

$$q_\theta(s) = \frac{1}{2\pi}\int_{-\infty}^{\infty} H(\omega)\tilde{p}_\theta(\omega)e^{i\omega s}d\omega \tag{6.11.2}$$

The final transformed function will then be defined by:

$$\begin{aligned} f_H(x,y) &= \frac{1}{2\pi}\int_0^\pi q_\theta(x\cos\theta + y\sin\theta)d\theta \\ &= \frac{1}{2\pi}\int_0^\pi \left[\frac{1}{2\pi}\int_{-\infty}^{\infty} H(\omega)\tilde{p}_\theta(\omega)e^{i\omega s}d\omega\right]d\theta \end{aligned} \tag{6.11.3}$$

So the filtered function will be

$$f_H(x,y) = \frac{1}{(2\pi)^2}\int_0^\pi \int_{\mathbb{R}} H(\omega)\tilde{p}_\theta(\omega)e^{i\omega(x\cos\theta + y\sin\theta)}d\omega d\theta \tag{6.11.4}$$

$$= \frac{1}{(2\pi)^2}\int_0^\pi \int_{\mathbb{R}} H(\omega)F(\omega\cos\theta, \omega\sin\theta)e^{i\omega s}d\omega d\theta \tag{6.11.5}$$

By moving to polar coordinates with variables:

$$\begin{cases} k_x = \omega\cos\theta \\ k_y = \omega\sin\theta \end{cases} \tag{6.11.6}$$

and using the fact that the modulus of the Jacobian $|J| = |\omega|$, one has:

$$dk_x dk_y = |\omega| d\omega d\theta \implies d\omega d\theta = \frac{dk_x dk_y}{|\omega|} \tag{6.11.7}$$

with $|\omega| = \sqrt{\omega^2} = \sqrt{\omega^2(\cos^2\theta + \sin^2\theta)} = \sqrt{k_x^2 + k_y^2}$. So

$$\begin{aligned} f_H(x,y) &= \frac{1}{(2\pi)^2}\int_{\mathbb{R}^2} H(\omega(k_x,k_y))F(k_x,k_y)e^{i(k_x x + k_y y)}\frac{1}{|\omega(k_x x, k_y y)}dk_x dk_y \\ &= \frac{1}{(2\pi)^2}\int_{\mathbb{R}^2} \frac{H(\sqrt{k_x^2+k_y^2})}{\sqrt{k_x^2+k_y^2}}F(k_x,k_y)e^{i\mathbf{k}\cdot x}d\mathbf{k} \\ &= \frac{1}{(2\pi)^2}\int_{\mathbb{R}^2} G(k_x,k_y)F(k_x,k_y)e^{i\mathbf{k}x}d\mathbf{k} \end{aligned} \tag{6.11.8}$$

where the quantity $G(k_x,k_y) = \frac{H(\sqrt{k_x^2+k_y^2})}{\sqrt{k_x^2+k_y^2}}$ was defined. So without normalizations

$$F^{rec}(k) = G(k)F(k) \qquad\qquad G(k) = \frac{H(|k|)}{|k|} \tag{6.11.9}$$

Following this reasoning the back-projection (BP) process can be viewed as a convolution between a filter and a radial kernel $g(r)$:

$$\begin{aligned} BP &= \frac{1}{(2\pi)^2}\int_0^\pi \int_{\mathbb{R}} \tilde{p}_\theta(\omega)G(\omega)e^{i\omega(x\cos\theta + y\sin\theta)}\,d\omega\,d\theta \\ &\implies BP(x,y) = (f * g)(x,y). \end{aligned} \tag{6.11.10}$$

Here $G(k_x,k_y)$ denotes the frequency-domain representation of the filter, which depends radially as $G(k_x,k_y) = G(k)$ with $k = \sqrt{k_x^2+k_y^2}$.
Introducing polar coordinates:

$$\begin{cases} k_x = k\cos\theta, \\ k_y = k\sin\theta, \\ r = \sqrt{x^2+y^2}, \end{cases}$$

the radial component of the kernel is obtained as the Hankel transform of order zero:

$$g(r) = \frac{1}{2\pi}\int_0^\infty G(k)J_0(kr)\,k\,dk, \tag{6.11.11}$$

where J_0 is the zeroth-order Bessel function of the first kind [68].

For large r, using the asymptotic expansion

$$J_0(kr) \sim \sqrt{\frac{2}{\pi kr}} \cos(kr - \pi/4),$$

one finds that

$$g(r) \propto \frac{1}{r},$$

showing that the spatial kernel decays inversely with distance.
Since the noise spectrum is defined as $S(\omega) = \langle nn^* \rangle$, and the filter modifies the frequency response by a factor $G(\omega)$, the resulting noise spectrum becomes

$$S_{\text{final}}(\omega) \propto |G(\omega)|^2.$$

Thus, the filter not only affects the reconstructed image but also shapes the spectral characteristics of the noise.

6.12

In this Appendix, we illustrate the convergence behaviour of the Maximum Likelihood Estimation (MLE) algorithm. When the number of data points is finite, multiple density matrices may indeed maximize the Likelihood, resulting in a possible *convergence drifting*.
The log-likelihood function is defined as:

$$\mathcal{L}(\hat{\rho}) = \sum_{m=1}^{M} \ln p_m(\hat{\rho}), \tag{6.12.1}$$

where $p_m(\hat{\rho}) = \langle f_m | \, \hat{\rho} \, | f_m \rangle$ is the probability associated with the Fock state $|f_m\rangle$.
In the MLE framework, the Likelihood function $\mathcal{L}(\hat{\rho})$ is maximized by a density matrix $\hat{\rho}^*$. In the asymptotic limit of infinite data and Fock dimension, the *ideal* (theoretical) log-likelihood coincides with its expectation value over the true distribution able to generate $\hat{\rho}^*$. Hence, in theory, no iterations would be necessary: the maximum could be found in a single calculation.
However, the ideal conditions hold only if the number of points and the Fock space dimension are infinite. For finite datasets and practical Fock dimension, the *numerical Likelihood* converges to the ideal Likelihood through the Law of Large Numbers [47]:

$$\mathcal{L}_n(\hat{\rho}^*) \xrightarrow{p} \mathcal{L}(\hat{\rho}^*), \quad n \to \infty. \tag{6.12.2}$$

We can therefore distinguish between the *ideal Likelihood* and the *real Likelihood*. The real Likelihood is treated as an optimization problem, with the density matrix $\hat{\rho}$ as the optimization parameter. It satisfies

$$\mathcal{L}_n(\rho) \leq \mathcal{L}(\rho^*), \tag{6.12.3}$$

where equality holds only at $\rho = \rho^*$ in the limit of infinite iterations. The iterative procedure of MLE is monotonic: the log-Likelihood increases at each step. Hence, the algorithm is reliable when a sufficiently large dataset is available (see Figure 5.7).
Since $\hat{\rho}^*$ maximizes the Likelihood, it follows that

$$\mathbb{P}_{\rho^*}\left[\mathcal{L}(X|\rho) = \mathcal{L}(X|\rho^*)\right] = 1. \tag{6.12.4}$$

Then the convergence of the MLE can be analysed using the derivatives of the Likelihood. Defining:

$$\mathcal{L}'(X|\rho) = \frac{\partial}{\partial \rho}\mathcal{L}(X|\rho), \tag{6.12.5}$$

we expect

$$\mathbb{E}_{\rho^*}[\mathcal{L}'(X|\rho^*)] = 0, \tag{6.12.6}$$

since ρ^* is the target density. The Fisher information is then:

$$I(\rho^*) = \mathbb{E}_{\rho^*}\left[\left(\mathcal{L}'(X|\rho^*)\right)^2\right] = \mathrm{Var}[\mathcal{L}'(X|\rho^*)]. \tag{6.12.7}$$

Using the Mean Value Theorem for some $\rho_1 \in [\rho, \rho^*]$:

$$0 = \mathcal{L}'_n(\rho) = \mathcal{L}'_n(\rho^*) + \mathcal{L}''_n(\rho_1)(\rho - \rho^*), \tag{6.12.8}$$

so that

$$\rho - \rho^* = -\frac{\mathcal{L}'_n(\rho^*)}{\mathcal{L}''_n(\rho_1)}, \quad \sqrt{n}(\rho - \rho^*) = -\sqrt{n}\frac{\mathcal{L}'_n(\rho^*)}{\mathcal{L}''_n(\rho_1)}. \tag{6.12.9}$$

Since $\rho_1 \in [\rho, \rho^*]$, one can show $\mathcal{L}''_n(\rho_1) \to -I(\rho^*)$, leading to the asymptotic distribution [47]:

$$-\frac{\sqrt{n}\mathcal{L}'_n(\rho^*)}{\mathcal{L}''_n(\rho_1)} \xrightarrow{d} \mathcal{N}\left(0, \frac{1}{I(\rho^*)}\right). \tag{6.12.10}$$

Physically, this means that the MLE estimate $\hat{\rho}$ is centred around the true state ρ^*, and its statistical fluctuations due to finite data are normally distributed. The numerator measures residual deviations of the observed log-likelihood from its expected value, while the denominator quantifies the sensitivity of the estimate to these fluctuations. The variance of $\hat{\rho}$ is inversely proportional to the Fisher information:

$$\mathrm{Var}(\hat{\rho}) \sim \frac{1}{I(\rho^*)}.$$

Then:

- More informative data (higher Fisher information) lead to more precise estimates.

- Less informative data (lower Fisher information) lead to larger statistical fluctuations.

The variance here arises from the finite estimation of the probability distribution. In the limit of noiseless, infinite data, the MLE converges directly to the true state. In practical experiments, noise and finite sampling slow convergence (see Figure 5.9). This can be mitigated by increasing the number of samples in simulations, but in real experiments hardware limitations may prevent arbitrarily fast acquisition.

Bibliography

[1] Sujaykumar Reddy M and Chandra Mohan B. Comprehensive analysis of BB84, a quantum key distribution protocol. December 2023.

[2] Frédéric Grosshans and Philippe Grangier. Continuous variable quantum cryptography using coherent states. *Phys. Rev. Lett.*, 88:057902, Jan 2002.

[3] Michael A. Nielsen and Isaac L. Chuang. *Quantum Computation and Quantum Information: 10th Anniversary Edition*. Cambridge University Press, Cambridge, 2010. `https://www.cambridge.org/highereducation/books/quantum-computation-and-quantum-information/01E10196D0A682A6AEFFEA52D53BE9AE`.

[4] Samuel L. Braunstein and Peter van Loock. Quantum information with continuous variables. *Rev. Mod. Phys.*, 77:513–577, Jun 2005.

[5] Vladyslav C. Usenko, Antonio Acín, Romain Alléaume, Ulrik L. Andersen, Eleni Diamanti, Tobias Gehring, Adnan A. E. Hajomer, Florian Kanitschar, Christoph Pacher, Stefano Pirandola, and Valerio Pruneri. Continuous-variable quantum communication, 2025.

[6] Joseph M. Lukens, Nicholas A. Peters, and Bing Qi. Hybrid classical-quantum communication networks. *Progress in Quantum Electronics*, 103:100586, September 2025.

[7] Ulf Leonhardt. Measuring the quantum state of light. *Physics Reports*, 338(2):77–139, 1997.

[8] J Aasi and et. a.l Abadie. Gravitational waves from known pulsars: Results from the initial detector era. *Astrophys. J.*, 785(2):119, April 2014.

[9] Han-Sen Zhong, Hui Wang, Yu-Hao Deng, Ming-Cheng Chen, Li-Chao Peng, Yi-Han Luo, Jian Qin, Dian Wu, Xing Ding, Yi Hu, Peng Hu, Xiao-Yan Yang, Wei-Jun Zhang, Hao Li, Yuxuan Li, Xiao Jiang, Lin Gan, Guangwen Yang, Lixing You, Zhen Wang, Li Li, Nai-Le Liu, Chao-Yang Lu, and Jian-Wei Pan. Quantum computational advantage using photons. *Science*, 370(6523):1460–1463, December 2020.

[10] M V Larsen, J E Bourassa, S Kocsis, J F Tasker, R S Chadwick, C González-Arciniegas, J Hastrup, C E Lopetegui-González, F M Miatto, A Motamedi, R Noro, G Roeland, R Baby, H Chen, P Contu, I Di Luch, C Drago, M Giesbrecht, T Grainge, I Krasnokutska, M Menotti, B Morrison, C Puviraj, K Rezaei Shad, B Hussain, J McMahon, J E Ortmann, M J Collins, C Ma, D S Phillips, M Seymour, Q Y Tang, B Yang, Z Vernon, R N Alexander, and D H Mahler. Integrated photonic source of Gottesman-Kitaev-Preskill qubits. *Nature*,

642(8068):587–591, June 2025.

[11] Gerd Breitenbach. *Quantum State Reconstruction of Classical and Nonclassical Light and Related Topics*. PhD thesis, University of Konstanz, 1999. PhD thesis on quantum state reconstruction of light.

[12] R. M. Shelby, M. D. Levenson, S. H. Perlmutter, R. G. DeVoe, and D. F. Walls. Broad-band parametric deamplification of quantum noise in an optical fiber. *Phys. Rev. Lett.*, 57:691–694, Aug 1986.

[13] C F McCormick, V Boyer, E Arimondo, and P D Lett. Strong relative intensity squeezing by four-wave mixing in rubidium vapor. *Opt. Lett.*, 32(2):178–180, January 2007.

[14] S. Machida, Y. Yamamoto, and Y. Itaya. Observation of amplitude squeezing in a constant-current–driven semiconductor laser. *Phys. Rev. Lett.*, 58:1000–1003, Mar 1987.

[15] Shiyuan Zhao, Shihao Ding, Heming Huang, Isabelle Zaquine, Nicolas Fabre, Nadia Belabas, and Frédéric Grillot. Broadband amplitude squeezing in electrically driven quantum dot lasers, 2023.

[16] Shihao Ding, Shiyuan Zhao, Heming Huang, and Frédéric Grillot. Observation of amplitude squeezing in a constant-current-driven distributed feedback quantum dot laser with optical feedback. *APL Quantum*, 1(2), June 2024.

[17] Laurie M. Brown. `https://faculty.washington.edu/seattle/physics441/online/about`. Accessed: 2025-10-27.

[18] Paul A. M. Dirac. *The Principles of Quantum Mechanics*. Oxford University Press, Oxford, 4th edition, 1958. Classic textbook introducing the bra-ket notation and the abstract formalism of quantum mechanics.

[19] Albert Einstein. Über einen die erzeugung und verwandlung des lichtes betreffenden heuristischen gesichtspunkt. *Annalen der Physik*, 17(6):132–148, 1905. Translated version available in Einstein Papers Project, Princeton University.

[20] Martin Bauer. The stern-gerlach experiment, translation of: "der experimentelle nachweis der richtungsquantelung im magnetfeld", 2023.

[21] Kai Wang, Daniel R. Terno, Časlav Brukner, Shining Zhu, and Xiao-Song Ma. Controlling wave-particle duality with entanglement between single-photon and bell states. *Physical Review A*, 106(5), November 2022.

[22] Max Born. Zur quantenmechanik der stoßvorgänge. *Zeitschrift für Physik*, 37(12):863–867, 1926.

[23] Benedikt Philipp. *Methodological Treatment of Non-linear Structural Behavior in the Design, Analysis and Verification of Lightweight Structures*. PhD thesis, 06 2017.

[24] Werner Heisenberg. Über den anschaulichen inhalt der quantentheoretischen kinematik und mechanik. *Zeitschrift für Physik*, 43(3-4):172–198, 1927. In this paper Heisenberg introduced the matrix formulation of quantum mechanics, showing that some operators do not commute.

[25] Werner Heisenberg. Über den anschaulichen inhalt der quantentheoretischen kinematik und mechanik. *Zeitschrift für Physik*, 43(3-4):172–198, 1927.

Heisenberg's uncertainty principle paper, introducing the fundamental disturbance caused by measurement.

[26] P A M Dirac. The quantum theory of the emission and absorption of radiation. *Proc. R. Soc. Lond. A Math. Phys. Sci.*, 114(767):243–265, March 1927.

[27] H. M. Wiseman and G. J. Milburn. Quantum theory of field-quadrature measurements. *Phys. Rev. A*, 47:642–662, Jan 1993.

[28] J D Franson. Third quantization of the electromagnetic field. February 2021.

[29] Rodney Loudon. *The Quantum Theory of Light*. Oxford University Press, 3rd edition, 2000.

[30] Andrey Pereverzev and Eric R. Bittner. On the derivation of exact eigenstates of the generalized squeezing operator. *arXiv preprint arXiv:0805.3666*, 2008.

[31] Michael Reed and Barry Simon. *Methods of Modern Mathematical Physics I: Functional Analysis*. Academic Press, 1980.

[32] E. Brian Davies. *Linear Operators and Their Spectra*. Cambridge University Press, 2007.

[33] Muhammad AbuGhanem. Full quantum process tomography of a universal entangling gate on an ibm's quantum computer, 2024.

[34] M. AbuGhanem and Hichem Eleuch. Quantum tomography study of db gate on an ibm's quantum computer, 2023. Accessed: 2025-08-28.

[35] John Wright. Lecture 22: Introduction to quantum tomography. url = https://www.cs.cmu.edu/ odonnell/quantum15/lecture22.pdf, November 2015. Accessed: 2025-08-28.

[36] W. K. Wootters and W. H. Zurek. A single quantum cannot be cloned. *Nature*, 299(5886):802–803, October 1982.

[37] E E Perepelkin, B I Sadovnikov, N G Inozemtseva, and P V Afonin. Wigner function properties for electromagnetic systems. August 2023.

[38] D. Gross. Hudson's theorem for finite-dimensional quantum systems. *Journal of Mathematical Physics*, 47(12), December 2006.

[39] N. Lütkenhaus and Stephen M. Barnett. Nonclassical effects in phase space. *Phys. Rev. A*, 51:3340–3342, Apr 1995.

[40] R. T. Thew, K. Nemoto, A. G. White, and W. J. Munro. Qudit quantum-state tomography. *Physical Review A*, 66(1), July 2002.

[41] A I Lvovsky. Iterative maximum-likelihood reconstruction in quantum homodyne tomography. *Journal of Optics B: Quantum and Semiclassical Optics*, 6(6):S556–S559, May 2004.

[42] D. Sych, J. Řeháček, Z. Hradil, G. Leuchs, and L. L. Sánchez-Soto. Informational completeness of continuous-variable measurements. *Phys. Rev. A*, 86:052123, Nov 2012.

[43] R. A. Fisher. Theory of statistical estimation. *Mathematical Proceedings of the Cambridge Philosophical Society*, 22(5):700–725, 1925.

[44] R. D. H. Heijmans and J. R. Magnus. Consistency of maximum likelihood estimators when observations are dependent. Working Paper Amsterdam 042, University of Amsterdam, Department of Econometrics, 1983. Working Paper – Amsterdam School of Economics.

[45] Abraham Wald. Note on the consistency of the maximum likelihood estimate. *Ann. Math. Stat.*, 20(4):595–601, December 1949.

[46] Andreas Anastasiou. Bounds for the normal approximation of the maximum likelihood estimator from m-dependent random variables, 2016.

[47] MIT. `https://ocw.mit.edu/courses/18-443-statistics-for-applications-fall-2006/03b407da8a94b3fe22d987453807ca46_lecture3.pdf?` Accessed: 2025-10-8.

[48] Peter J Olver. Numerical analysis lecture notes. `https://www-users.cse.umn.edu/~olver/num_/lns.pdf?` Accessed: 2025-10-8.

[49] Stephen J. Wright Jorge Nocedal. `https://www.math.uci.edu/~qnie/Publications/NumericalOptimization.pdf`. Accessed: 2025-10-8.

[50] Christopher Ferrie and Robin Blume-Kohout. Maximum likelihood quantum state tomography is inadmissible, 2018.

[51] Error - Cookies Turned Off — onlinelibrary.wiley.com. `https://onlinelibrary.wiley.com/doi/book/10.1002/9780470178737`. [Accessed 15-10-2025].

[52] Ruiyang Chen, Yi-Han Luo, Jinbao Long, and Junqiu Liu. Arbitrary-phase locking of fiber unbalanced mach-zehnder interferometers. *Physical Review Applied*, 22(5), November 2024.

[53] Konrad Banaszek. Reconstruction of photon distribution with positivity constraints, 1998.

[54] Konrad Banaszek. Maximum-likelihood estimation of photon-number distribution from homodyne statistics. *Phys. Rev. A*, 57:5013–5015, Jun 1998.

[55] M. Munroe, D. Boggavarapu, M. E. Anderson, and M. G. Raymer. Photon-number statistics from the phase-averaged quadrature-field distribution: Theory and ultrafast measurement. *Phys. Rev. A*, 52:R924–R927, Aug 1995.

[56] Paolo Mazzoldi, Massimo Nigro, and Cesare Voci. *Fisica 2*. Zanichelli, 7 edition, 2021.

[57] K. O. Friedrichs. *Mathematical Aspects of the Quantum Theory of Fields*. Interscience Publishers, 1st edition, 1953. ASIN: B0006ATGK4.

[58] David J. Griffiths. *Introduction to Quantum Mechanics*. Pearson Prentice Hall, Upper Saddle River, NJ, 2nd edition, 2005.

[59] Académie des Sciences (France). Comptes rendus hebdomadaires des séances de l'académie des sciences. *Comptes Rendus Hebdomadaires*, 1864. Accessible via Biodiversity Heritage Library, item 23663, page ?

[60] Kurt Glasner. Fourier transform techniques, 2019. Accessed: 2025-08-27.

[61] Anirban Gupta, Robert Kosut, and Berthold Englert. Statistical analysis of low rank tomography with compressive random measurements. *arXiv preprint arXiv:1609.03758*, 2016.

[62] Donghong Han, Chu Guo, and Xiaoting Wang. Density matrix reconstruction using non-negative matrix product states. *Phys. Rev. A*, 106:042435, Oct 2022.

[63] Markus Frembs and Eric G Cavalcanti. Variations on the choi–jamiołkowski isomorphism. *Journal of Physics A: Mathematical and Theoretical*, 57(26):265301,

June 2024.

[64] Wolfram Research. Haar measure — from MathWorld, 2025. Accessed: 2025-08-29.

[65] Claude Cohen-Tannoudji, Bernard Diu, and Franck Laloë. *Mécanique quantique*. Hermann, Paris, 1 edition, 1977. Vol. I e II. Contiene trattazioni di Baker-Campbell-Hausdorff e della formula di Glauber.

[66] Eugene P. Wigner. On the quantum correction for thermodynamic equilibrium. *Physical Review*, 40:749–759, 1932.

[67] R N Bracewell. Numerical transforms. *Science*, 248(4956):697–704, May 1990.

[68] Le funzioni di bessel. https://dipmat.univpm.it/~calamai/METODI_1011/F_Bessel.pdf. Accessed: 2025-9-19.